Bosons in Rotating Optical Lattices

by

Rajiv Bhat

M. Sc. (Integrated), Indian Institute of Technology Kanpur

2001

A thesis submitted to the

Faculty of the Graduate School of the

University of Colorado in partial fulfillment

of the requirements for the degree of

Doctor of Philosophy

Department of Physics

2008

This thesis entitled:
Bosons in Rotating Optical Lattices
written by Rajiv Bhat
has been approved for the Department of Physics

Prof. Murray J. Holland

Prof. John L. Bohn

Date

The final copy of this thesis has been examined by the signatories, and we find that both the content and the form meet acceptable presentation standards of scholarly work in the above mentioned discipline.

Bhat, Rajiv (Ph. D., Physics)

Bosons in Rotating Optical Lattices

Thesis directed by Prof. Murray J. Holland

The fractional Quantum Hall effect (FQHE) has been predicted in a cloud of bosons rotating at a frequency equal to that of the confining harmonic potential. Achieving this regime experimentally, by directly spinning the cloud, is a challenge. In this thesis, we probe an alternate approach to realizing the FQHE physics in cold gases by examining cold bosons confined to a rotating optical lattice.

We derive modified Bose-Hubbard Hamiltonians to study the system in the tight-binding limit and develop analogies to Bloch electrons in the presence of a magnetic field. The primary effect of rotation is to introduce non-abelian character in the problem. This is because the system picks up a phase not always equal to a multiple of 2π when a particle goes around a plaquette.

We numerically study hardcore bosons in the tight-binding limit by diagonalizing a Hamiltonian constructed using a truncated Fock basis. We show that vorticity can exist in the tight-binding limit though angular momentum is no longer quantized. Using the discrete rotational symmetry of the system, we identify quasi-angular momentum as a good quantum number. Quantum phase transitions are expected when the discrete rotational symmetry of the ground state changes. Using a perturbative analysis, we show that the effect of a weak lattice is to spatially modulate the Hall resistance. A linear-response analysis of the system's response to an AC perturbation shows that the system does indeed display FQHE characteristics. We attempt to extend the analysis to larger systems using Monte Carlo methods. We show that the sign problem is inherent in the World Line Monte Carlo method as applied to non-abelian systems.

Dedication

To my parents.

Acknowledgements

I would like to thank my advisor Prof. Murray Holland for giving me this wonderful opportunity to do much beautiful physics under his guidance. His passion for the subject and broad-minded approach to independent research shaped my experience in a sublime way. I would also like to thank Prof. John (Jinks) Cooper for his invaluable guidance at every stage of my research. Getting to observe his tenacity for resolving even the smallest inconsistencies was simultaneously both humbling and inspiring. I am lucky to have gotten them — both as mentors and as friends.

Much of this thesis was shaped by the countless interactions with the other members of the Holland group: Stefano Giorgini, Simon Gardiner, Servaas Kokkelmans, Meret Krämer, Lincoln Carr, Jami Kinnunen, Dominic Meiser, Satyan Bhongale, Rob Chiaramonte, Jochen Wachter, Brian Seaman, Brandon Peden, Sarah McGee, Ronald Pepino, Dave Tieri and Boris Nowak. I would like to acknowledge their warm support and enthusiasm. There is much more to say and there are many more, in Boulder and elsewhere, to thank for helping me through the course of my research. In particular, I would like to thank Dominic, Jochen, Brian and Kartic for editing this manuscript. Any remaining errors are purely mine.

My siblings — Giri and Jyothi — cannot be thanked enough for all the strength they have given me. Finally, this thesis would not have been possible without the infinite encouragement, patience and support of my wife and best friend, Ramya.

Contents

Chapter

Figures

Figure

Chapter 1

Introduction

1.1 Background

In an attempt to formally derive Planck's radiation law in the early 1920s, Satyendra Nath Bose proposed a formalism for describing photon statistics where photons were considered indistinguishable. His efforts to get the results published met with initial resistance and he sent the manuscript directly to Albert Einstein to get his help. Einstein not only agreed with Bose but also showed that the formalism could be extended to all bosons [15, 23]. This formalism for indistinguishable bosons is now known as Bose-Einstein statistics. Einstein also showed that if bosons were cooled to very low temperatures, they would simultaneously occupy the lowest available quantum state forming a Bose-Einstein condensate (BEC).

The first experimental instance of a BEC was obtained in 1938 when Kaptitza, Allen and Misener discovered superfluidity in Helium-4 [40, 3]. However, the strong interactions between particles made the phenomena of superfluidity in Helium difficult to explain. Much of the subsequent theory was phenomenological because the experimental parameters needed to test the theories were not tunable. This changed when BECs were realized in weakly-interacting cold alkali gases in 1995 [5, 20, 16]. Since then, theoretical and experimental research in cold alkali atoms has exploded due to at least three main factors.

Firstly, interactions between the particles in a cold atom BEC can be tuned easily.

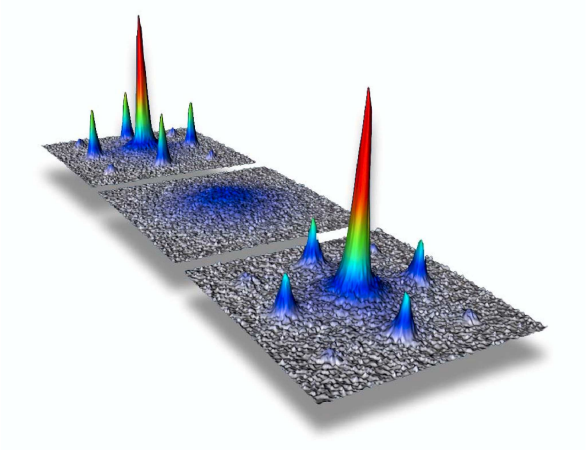

Figure 1.1: (Back to front) Superfluid, Mott insulator and superfluid signatures obtained by Greiner *et al.* [29] for a Bose-Einstein condensate in an optical lattice. These signatures correspond to momentum-space distributions obtained by taking time of flight images. In the superfluid state (shallow lattice), there is a coherent phase description across sites leading to an interference pattern while there is no such interference for the Mott insulator state (deep lattice).

The two-body scattering length can be varied via a Feshbach resonance by changing the magnetic field and interactions can be made repulsive or attractive to the extent required [37]. In 2003, this technique was used to coerce fermions into forming bosonic molecules which were then condensed into a BEC [30]. Secondly, BECs can be loaded into optical lattices. An optical lattice is formed from an off-resonant light-intensity pattern created by the interference of several laser beams. The atoms feel a potential proportional to the intensity of the light field. The height of the lattice potential can be tuned by changing the laser intensity. In a fine instance of how this could be used, Greiner *et al.* [29] experimentally demonstrated quantum phase transitions by showing that a condensate loaded in a lattice could be made to go from a superfluid phase (shallow lattice) to a Mott insulator phase (deep lattice) by simply changing the lattice depth (Fig. 1.1). Efforts are underway to use BECs in lattices to understand the role of periodic potentials in phenomena such as high-temperature superconductivity and creation of exotic anyonic states [22]. Lastly, rotation can be introduced in BECs. This

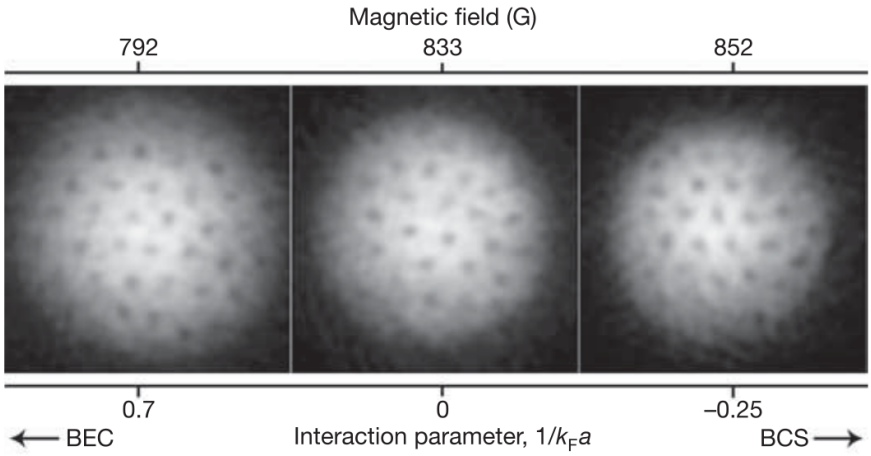

Figure 1.2: Vortex lattices as seen by Zwierlein *et al.* [89] on both sides of the BEC-BCS crossover. The vortex lattice on the right indicates superfluidity in a condensate of bosonic Li^6 molecules. The vortex lattice is on the left is due to a condensate of Cooper pairs (pairs in momentum space) and is a signature of superfluidity in strongly interacting Fermi gases.

rotation manifests itself in the form of quantized vortices that can be easily imaged. Starting from the quantum engineering of a single vortex [85], rotating condensates have been used to understand exotic phenomena such as the formation of Abrikosov vortex lattices [47, 32] and Tkachenko modes [72]. The presence of a vortex core is a signature of superfluidity. Recently, vortex lattices were imaged across the Feshbach resonance in the BEC-BCS crossover regime [89] hence demonstrating superfluidity in strongly interacting Fermi gases (Fig. 1.2).

1.2 Motivation

Rotating BECs are also expected to lead to the fractional quantum Hall effect (FQHE) in cold gases. Consider the Hamiltonian for a single particle in the presence of a symmetric 2D harmonic trap with oscillation frequencies ω. A coordinate transformation to a frame rotating with frequency Ω is accomplished by using the transformation $\mathcal{H} = \mathcal{H}_0 - \Omega L_z$ [45], where L_z is the angular-momentum operator around the axis of

rotation. The single-particle Hamiltonian in rotating frame coordinates is,

$$\begin{aligned}\mathcal{H} &= -\frac{\hbar^2}{2m}\nabla^2 + \frac{1}{2}m\omega^2\left(x^2+y^2\right) - \frac{\hbar\Omega}{i}\left(x\partial_y - y\partial_x\right) \\ &= \frac{1}{2m}\left(\frac{\hbar}{i}\nabla - m\left(\mathbf{\Omega}\times\mathbf{r}\right)\right)^2 + \frac{1}{2}m\left(\omega^2-\Omega^2\right)r^2 = \frac{1}{2m}\Pi^2 + \frac{1}{2}m\left(\omega^2-\Omega^2\right)r^2 . \quad (1.1)\end{aligned}$$

Here, $\mathbf{r}$ is the distance from the axis of rotation and m is the mass of the particle. In the last step, the covariant momentum $\mathbf{\Pi} \equiv \mathbf{p} - m\mathbf{A}$ and the vector potential $\mathbf{A} \equiv \mathbf{\Omega}\times\mathbf{r}$ have been introduced. The similarities to the Hamiltonian for a single particle in the presence of a magnetic field are already evident in Eq. 1.1 — To quote Mueller *et al.*[58], this is — *'identical to the Hamiltonian of an electron in a magnetic field in a harmonic potential of reduced frequency* $\left(\omega^2-\Omega^2\right)$*'* . The allowed energies are,

$$E_{p,q} = \hbar\left(\omega+\Omega\right)p + \hbar\left(\omega-\Omega\right)q + \hbar\omega \quad (1.2)$$

where $p, q \geq 0$ are integers (vibrational quantum numbers). In the limit $\Omega \to \omega$, the single-particle Hamiltonian above (Eq. 1.1) reduces to,

$$\mathcal{H} \;=\; \frac{1}{2m}\left(\Pi_x^2 + \Pi_y^2\right) \quad (1.3)$$

and the ground state becomes infinitely degenerate. This is shown for the lowest few energy levels in Fig. 1.3. The lowest set of states is referred to as the 'Lowest Landau Level' (LLL). The single-particle Hamiltonian above can be compared with that for a single electron in the presence of a magnetic field,

$$\mathcal{H}_e \;=\; \frac{1}{2m_e}\left(\Pi_{e,x}^2 + \Pi_{e,y}^2\right) \quad (1.4)$$

where $\Pi_e \equiv \mathbf{p} - e\left(\mathbf{B}\times\mathbf{r}\right)/2$. The Hamiltonians in Eqs. 1.3 and 1.4 coincide if rotations are identified with an effective magnetic field according to $2\mathbf{\Omega} \to \mathbf{B}$.

When many electrons are introduced into the system, they occupy different degenerate single particle states due to Coulombic repulsion[1] and accordingly, the many-particle ground state is highly fragmented. If the magnetic field is quantized in terms

[1] For many particles to occupy the degenerate single particle states, it is not necessary that the repulsion be coulombic. It is sufficient that the inter-particle interaction potential be a contact delta interaction (see Ezawa [25]).

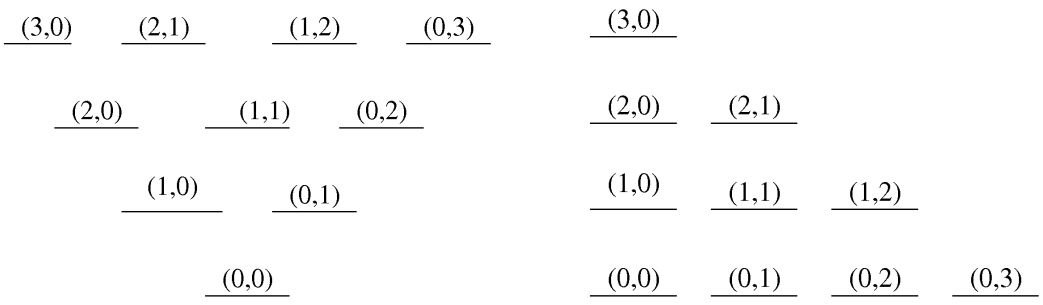

Figure 1.3: Shown here are the lowest few energy levels labelled by (p, q) in Eq. 1.2 for a single particle in a 2D harmonic oscillator in a frame rotating with an angular velocities (*left*) $\Omega = 0$ and (*right*) $\Omega = \omega$. The lowest set of infinitely degenerate energies on the right is known as the lowest Landau level.

of flux quanta then the nature of the ground state is characterized by the filling factor which is the ratio of the number of electrons per unit area to the number of flux quanta within the same area. The filling factor increases with magnetic field intensity and decreases with electron density. For simple rational values of the filling factor, the ground state becomes incompressible giving rise to the FQHE. Further discussion about the FQHE in electrons is resumed in Sec. 5.2.

Due to the similarity with the electron system, the physics of the FQHE should emerge for a two-dimensional (2D) condensate rotating at a frequency matching that of the confining harmonic trap [84, 19, 83, 61, 27, 13, 7]. Achieving this regime experimentally is a significant goal of the field at this time. The direct approach of spinning-up a BEC to reach the regime of strongly correlated effects is challenging, because of the need to reach a parameter regime of low particle number per vortex and extremely low temperature [72]. This is challenging because of two reasons: it is difficult to confine condensates at rotation speeds matching the trapping frequency and vortex shears destroy condensates at high rotation.

In this context, it is useful to look at optical lattices. Optical lattices can be used to both reduce the number of particles per vortex and enhance interactions. As the laser

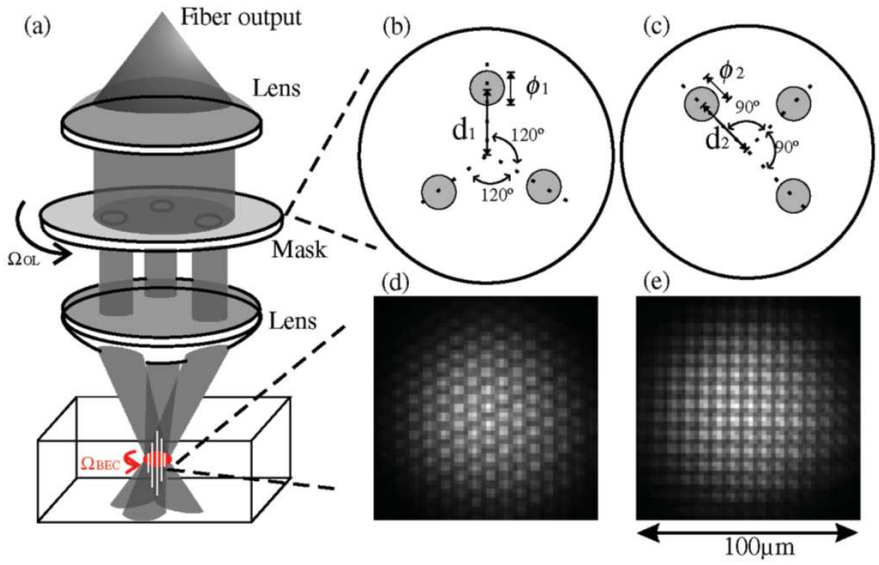

Figure 1.4: (a) Schematic diagram of the setup used by Tung *et al.* [79] for the rotating quasi-2D optical lattice. Triangular (b) and square masks (c) are used for triangular (d) and square (e) optical lattices respectively.

fields are made more intense, the interactions are enhanced, because the atoms become more strongly confined in the lattice wells. Introducing a co-rotating optical lattice in the tight-binding regime, in which particles on a lattice site can only tunnel to adjacent sites, provides strong confinement and enhances interactions to enable entry into the strongly-correlated regime. It is thus a natural question to pose as to whether one can combine the intriguing physics of the rotating gas with the enhanced interactions in an optical lattice. The motivation is to move the regime of quantum Hall physics in ultracold atomic gases towards a parameter space that is experimentally achievable.

Theoretical research in this area has been active. Connections have been made to the FQHE for cold atoms in a lattice in the presence of an effective magnetic field by Mueller [57], Sørenson *et al.* [73] and Palmer *et al.* [60]. Further, in a recent paper, Umucalilar *et al.* [80] presented the phase diagram for bosons in an optical lattice in the presence of an effective magnetic field.

In an early experiment with a rotating optical lattice, Tung *et al.* [79] recently

demonstrated vortex pinning in a weakly interacting BEC. The rotating lattice was realized by passing a laser beam through a mask that contains holes arranged in a particular configuration and then focusing the laser beams to form the lattice interference pattern (Fig. 1.4). The two dimensional optical lattice is rotated by spinning the mask.

The need for more theoretical methods to study the strongly-correlated FQHE regime for bosons in a rotating optical lattice is urgent, as experimental capabilities to realize such systems are rapidly coming to bear. The two main characteristics of this regime, which can also be called the fractional statistics regime, are: site number densities of order unity stemming from strong interactions and filling factors (particles per vortex) of order unity (Fig. 1.5). The latter allows for the creation of composite particles necessary to observe quantum Hall phenomena. Accordingly, the first experimental requirement is for an optical lattice in the tight-binding regime with lattice spacing of order $d \sim 0.5\ \mu m$. The second requirement is for the energy associated with rotation to be of the order of the lattice recoil energy or, equivalently, for the associated Larmor radius to be of the same order as the lattice spacing. Both requirements have been separately satisfied [29, 72]. An immediate benefit of such experiments is the measurement of the equivalent of the flux quantum (h/e^2) constant for mass transport.

1.3 Overview

The work presented in this thesis is oriented towards understanding the behavior of bosons in a 2D rotating optical lattice and probing for FQHE physics in such a system. The parameter regime of interest is shown in gray in Fig. 1.5. Including the introduction, this thesis is divided into six chapters. Most of the work presented in this thesis has been published in Refs. [10, 12, 11, 62].

The second chapter derives and discusses the Bose-Hubbard Hamiltonian in rotating frame coordinates. It is possible to describe the system using two Hamiltonians that look very different. A detailed comparison of the two approaches is presented

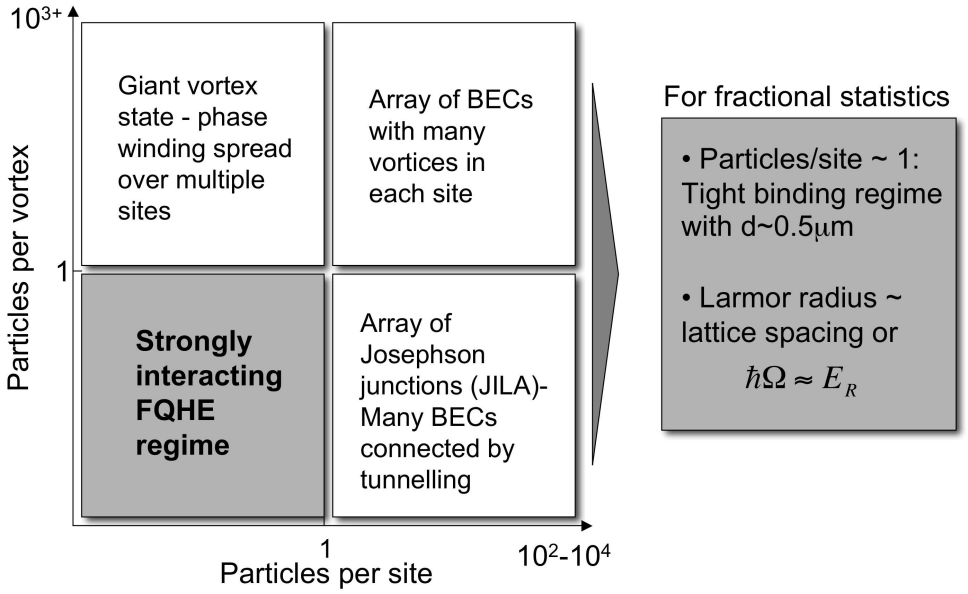

Figure 1.5: Parameter regime for bosons in rotating optical lattices. The shaded area marks the regime of interest for the work in this thesis. The parameter space represented by the two squares on the right side have been experimentally realized by Tung *et al.* [79].

using analytical and imaginary time propagation (ITP) techniques. The first is more suitable for studying the symmetry properties of the system at low rotation while the second is more general and works better for larger rotation. Connections are made to the condensed-matter literature on Bloch electrons in a magnetic field by deriving the Harper equation in the continuous limit of the Bose-Hubbard Hamiltonian in rotating-frame coordinates and showing that the single-particle energy spectra for the latter is the Hofstadter butterfly.

The third chapter describes the symmetry properties of the system. Evidence is presented for vorticity in the presence of a very deep lattice. The notion of quasiangular momentum associated with the discrete rotational symmetry of the system is developed. Changes in the ground-state symmetry with change in angular velocity of the lattice are identified as quantum phase transitions.

The fourth chapter is devoted to the transport characteristics of the system. Operators are defined for the onsite density and the particle current between sites. Increasing repulsive interaction between particles is shown to inhibit inter-site particle current. The Kubo formula to study the linear response of the system to a time-periodic (AC) perturbation is formally developed.

The fifth chapter studies the connection between bosons in a 2D rotating optical lattice and the Quantum Hall effect and is divided into three main sections. The first section presents the QHE as a topological invariant. A weak lattice is introduced to the regular QHE setup in the second section and its effects on the Hall resistance is evaluated using a perturbative analysis. The last section shows that aspects of the QHE are indeed present for the system under study. When the lattice is subjected to AC tilting, signatures are seen in the current and density responses at simple rational values of α.

The last chapter of the thesis explores Monte Carlo methods for non-abelian systems (as defined by multi-valued wavefunctions under adiabatic transport) such as the one under study. A brief description of Markov Chain Monte Carlo methods is presented with a focus on the World Line Monte Carlo technique. This technique is then extended to non-abelian systems with a discussion of the negative sign problem inherent in this method.

Chapter 2

Derivation of Hamiltonian

2.1 Introduction

Studying bosons in a rotating optical lattice is intriguing because it combines rotation with a periodic potential. This combination presents challenges because both elements are best described in different coordinate systems. Rotation about an axis is best captured using polar or cylindrical coordinates while periodic lattice potentials lend themselves naturally to cartesian coordinates. This fundamental difference manifests itself as one tries different approaches to study the system. Approaches with a strong cartesian nature work well for small rotation (see following section), while approaches with strong rotation character work well for a weak periodic potential (*e. g.* Sec 5.4).

In this chapter, we develop a modified Bose-Hubbard Hamiltonian using two approaches. The first uses a passive transformation into rotating-frame coordinates. This method is confined to a description using only the lowest Wannier states which becomes an increasingly poor approximation with increasing rotation. The second approach uses a local gauge transformation in addition to rotating frame coordinates to capture the effects of rotation. Both methods would be identical if Wannier states in all higher bands were used to construct the site-specific creation/annihilation field operators. However, subtle differences crop up when only Wannier states in the lowest band are retained. We present qualitative and numerical comparisons between the two approaches for a small system.

2.2 Derivation using passive transformation into rotating frame coordinates

This section presents one Hamiltonian that can be used to study bosons in a deep rotating 2D lattice and is divided into three parts. The first part introduces the Bose-Hubbard Hamiltonian commonly used to study bosons in a stationary periodic potential. The second part shows how one can use a passive transformation into rotating frame coordinates. The last part describes the Bose-Hubbard Hamiltonian in rotating frame coordinates as obtained after retaining only the lowest Wannier states used to study a non-rotating system.

2.2.1 Bose-Hubbard Hamiltonian for bosons in a stationary 2D optical lattice

The study of interacting bosons in a lattice using a Hubbard Hamiltonian was broached by M. P. A. Fisher *et al.* in 1989 [28]. In a landmark paper, they explored the competing effects of repulsive interactions and pinning by a lattice potential and predicted the presence of the Mott insulator-superfluid quantum phase transition. Jaksch *et al.* [38] showed that this description could be extended to cold bosonic atoms in an optical lattice. In an exciting development, the Mott-insulator-superfluid transition was experimentally realized[1] at Munich in 2002 [29] thus opening up a new area of research with cold gases in optical lattices.

An optical lattice is an off-resonant light-intensity pattern created by the interference of several laser beams. Due to the AC Stark effect, the atoms feel a potential proportional to the intensity of the light field. For 2D optical lattices, like that used in the Munich experiment, the effective potential energy experienced by the atoms is,

$$V^{\mathrm{lat}}(\mathbf{x}) = V_0 \left[\cos^2\left(\frac{\pi x}{d}\right) + \cos^2\left(\frac{\pi y}{d}\right)\right] , \tag{2.1}$$

[1] A recent claim by Diener *et al.* [21] contests the 'quantum' nature of the transitions stating that the visibility measure used doesn't adequately distinguish between normal and superfluid phases.

where d is the lattice spacing and V_0 is proportional to the laser power intensity. The Hamiltonian for a single particle in this potential is,

$$\mathcal{H}_0(\mathbf{x}) = -\frac{\hbar^2}{2m}\nabla^2 + V^{(\mathrm{lat})}(\mathbf{x})\,, \tag{2.2}$$

where m is the single particle mass. The eigen solutions to the Schrödinger equation, $\mathcal{H}_0(\mathbf{x})\phi^l_{\mathbf{q}}(\mathbf{x}) = E^l_{\mathbf{q}}\phi^l_{\mathbf{q}}(\mathbf{x})$, are Bloch functions, which can be obtained by solving the Mathieu equation [1, 6]. Here, l is the band-index and $\mathbf{q}$ denotes the quasimomentum associated with the eigenfunctions. For any band l, the Bloch functions can be combined using a discrete Fourier transform to yield a set of orthonormal Wannier basis functions,

$$W^l_S(\mathbf{x}-\mathbf{x}_i) = \frac{1}{\sqrt{N}}\sum_{\mathbf{q}} e^{-i\mathbf{q}.\mathbf{x}_i}\phi^l_{\mathbf{q}}(\mathbf{x})\,, \tag{2.3}$$

where $\mathbf{x}_i$ denotes the center of the i^{th} site and N is the total number of sites. This gives site-localized wavefunctions. If the energies due to interaction and rotation are small compared to the energy separation between the lowest and first excited band, the particles are confined to the lowest Wannier orbitals. We consider this regime only and henceforth drop the band index l. To extend the single-particle picture, we introduce repulsive interactions between particles using a s-wave contact model for two-body scattering in a dilute gas. We thus use the following second quantized Hamiltonian,

$$\hat{\mathcal{H}}_0 \equiv \int d\mathbf{x}\ \hat{\Phi}^\dagger(\mathbf{x})\left[\mathcal{H}_0(\mathbf{x}) + \frac{g}{2}\hat{\Phi}^\dagger(\mathbf{x})\hat{\Phi}(\mathbf{x})\right]\hat{\Phi}(\mathbf{x})\,, \tag{2.4}$$

where g is the coupling constant for repulsive two-body s-wave scattering via a contact interaction. The bosonic field operator $\hat{\Phi}$ obeys the commutation relation $\left[\hat{\Phi}(\mathbf{x}), \hat{\Phi}(\mathbf{x}')^\dagger\right] = \delta(\mathbf{x}-\mathbf{x}')$ and can be expanded in terms of the Wannier basis, $W_S(\mathbf{x}-\mathbf{x}_i)$, and the corresponding site-specific annihilation operators, $\hat{a}_i$, as

$$\hat{\Phi}(\mathbf{x}) = \sum_{i=1}^{N}\hat{a}_i W_S(\mathbf{x}-\mathbf{x}_i)\,. \tag{2.5}$$

In the tight-binding regime, Wannier functions extend to only the nearest neighboring sites and tunneling between sites which are not nearest neighbors can be neglected

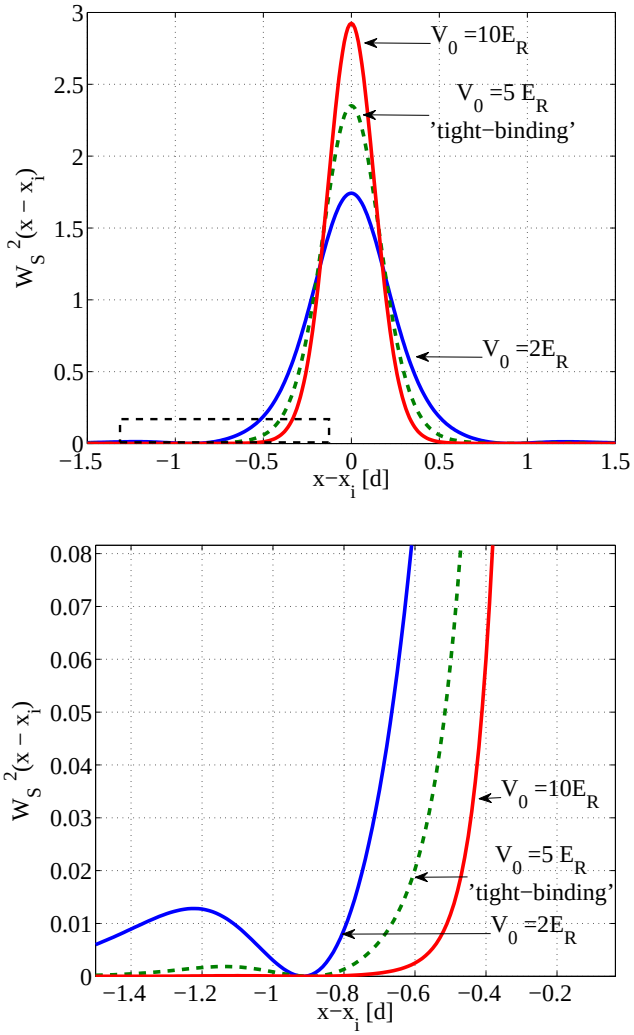

Figure 2.1: (Top) Single particle density profiles for three lattice depths described using Wannier functions. The dashed line shows the density profile for $V_0 = 5E_R$, a depth at which the system roughly enters the 'tight-binding' regime where the Wannier functions extend up to nearest neighboring sites. In the 'tight-binding' regime $V_0 > 5E_R$ where E_R is the lattice recoil energy (Eq. 2.9), the Wannier function is taken to extend to nearest neighboring sites and no further. (Bottom) Zoom-in (dashed box in left figure) of the single-particle density tails. Despite being orders of magnitude smaller than the central peak, the smaller peaks contribute significantly to the hopping energy. Due to this, approximating the Wannier functions by a Gaussian captures the onsite energy well but leads to large errors in the hopping energy.

(Fig. 2.1). The interaction between particles on nearest neighbor sites can also be neglected. Using this approximation and substituting for $\hat{\Phi}(\mathbf{x})$ and $\hat{\Phi}^{\dagger}(\mathbf{x})$ in Eq. 2.4 yields the well-known Bose-Hubbard Hamiltonian [28],

$$\hat{\mathcal{H}}_0 = -J\sum_{\langle i,j\rangle}\left(\hat{a}_i^{\dagger}\hat{a}_j + \hat{a}_i\hat{a}_j^{\dagger}\right) + \epsilon\sum_i \hat{n}_i + \frac{U}{2}\sum_i \hat{n}_i(\hat{n}_i - 1)\,, \tag{2.6}$$

where i and j are site indices, $\langle i,j\rangle$ indicates that the sum is over nearest neighbors, and $\hat{n}_i$ is the number operator for site i. The parameters, J and ϵ, are integrals describing hopping (or tunneling) and onsite zero-point energy respectively:

$$J \equiv \int d\mathbf{x}\; W_S^*(\mathbf{x}-\mathbf{x}_i)\mathcal{H}_0(\mathbf{x})W_S(\mathbf{x}-\mathbf{x}_j)\,, \tag{2.7}$$

$$\epsilon \equiv \int d\mathbf{x}\; W_S^*(\mathbf{x}-\mathbf{x}_i)\mathcal{H}_0(\mathbf{x})W_S(\mathbf{x}-\mathbf{x}_i)\,, \tag{2.8}$$

where Eq. 2.7 assumes J to be independent of the choice $\langle i,j\rangle$. Wannier functions along the x and y directions can be decoupled for a square lattice, and, accordingly, the integrals can be reduced to one-dimension. These overlap integrals (Eqs. 2.7 and 2.8) are plotted for the sinusoidal potential (Eq. 2.1) in Fig. 2.2. A convenient unit for studying this system is the recoil energy,

$$E_R = \frac{\hbar^2\pi^2}{2md^2}\,. \tag{2.9}$$

All energies described in this thesis are in units of the recoil energy except in the last chapter where energies are in units of the hopping energy J. The third term in the Hamiltonian, Eq. (2.6), describes the interaction between particles on the same site. For an s-wave scattering length a_s [38, 88],

$$U \equiv \frac{4\pi a_s\hbar^2}{M}\int d\mathbf{x}\;\left|W_S(\mathbf{x}-\mathbf{x}_i)\right|^4\,. \tag{2.10}$$

2.2.2 Transformation to rotating-frame coordinates

Complicated time dependence in rotating potentials can be avoided by switching to a coordinate system rotating with the same angular velocity as the potential. In this

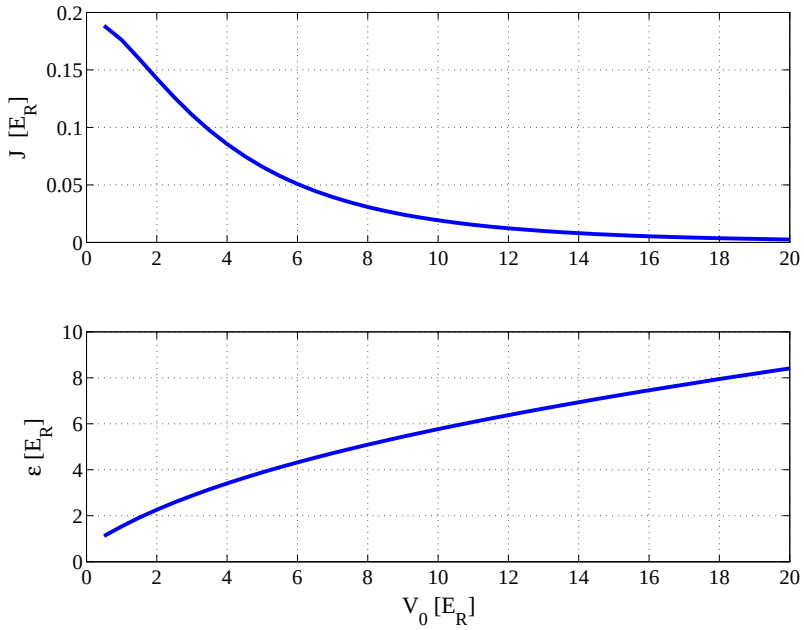

Figure 2.2: Overlap integrals represent the hopping energy J (Eq. 2.7) and zero-point onsite energy ϵ (Eq. 2.8)) as a function of lattice depth for a standing wave optical lattice described by $V^{\rm lat}(\mathbf{x}) = V_0(\cos^2(\pi x/d) + \cos^2(\pi y/d))$. The overlap integrals correspond to the hopping and zero-point onsite energies respectively. All energies are expressed in units of the recoil energy (Eq. 2.9).

sub-section, we rewrite the Hamiltonian using rotating-frame coordinates. We begin using a classical free particle as an example.

Consider a particle rotating about the z-axis with an angular velocity, ω in the stationary frame.[2] The position vector of the particle is $\mathbf{r}$ ($\equiv \mathbf{r}_0$) and the velocity in the stationary frame[3] is $\mathbf{v}_0 = \omega \times \mathbf{r}$. The angular momentum in the stationary frame is $\mathbf{L}_0 = m(\mathbf{r} \times \mathbf{v}_0) = \mathbf{r} \times \mathbf{p}_0$. The Lagrangian (in the stationary frame) is

$$\mathcal{L}_0 = \frac{1}{2} m v_0^2 = \mathcal{H}_0 \,, \tag{2.11}$$

where $\mathcal{H}_0$ is the Hamiltonian for the system in the stationary coordinate system.

[2] This section outlines the relevant discussion from *Landau and Lifshitz, Mechanics*. For the complete discussion, please see Section 39 of Ref. [45].

[3] In this subsection, subscripted quantities indicate representation in stationary frame coordinates while non-subscripted quantities are described using rotating-frame coordinates.

Now, examine the particle in a frame of reference which is rotating with an angular velocity Ω with respect to the stationary frame. The principle of least action is frame independent, but in order to derive Lagrange's equations of motions the variable in Eq. 2.11 (i.e. $\mathbf{v}_0$) needs to be expressed using rotating-frame coordinates. The velocity of the particle in the rotating frame is

$$\mathbf{v} = \mathbf{v}_0 - \Omega \times \mathbf{r} = (\omega - \Omega) \times \mathbf{r}\,. \tag{2.12}$$

The Lagrangian in rotating frame coordinates is

$$\begin{aligned} \mathcal{L} &= \mathcal{L}_0 = \frac{1}{2}mv_0^2 = \frac{1}{2}m(\mathbf{v} + \Omega \times \mathbf{r})^2 \\ &= \frac{1}{2}mv^2 + m\mathbf{v} \cdot (\Omega \times \mathbf{r}) + \frac{1}{2}m\left(\Omega \times \mathbf{r}\right)^2\,, \end{aligned} \tag{2.13}$$

and the conjugate momentum is given by

$$\mathbf{d}\mathcal{L} = m\mathbf{v} \cdot d\mathbf{v} + m(\Omega \times \mathbf{r}) \cdot d\mathbf{v} + m\mathbf{v} \cdot (\Omega \times d\mathbf{r}) + m\left(\Omega \times d\mathbf{r}\right).(\Omega \times \mathbf{r})\,, \tag{2.14}$$

$$\mathbf{p} = \frac{\partial \mathcal{L}}{\partial \mathbf{v}} = m\mathbf{v} + m(\Omega \times \mathbf{r}) = m\mathbf{v}_0 = \mathbf{p}_0\,. \tag{2.15}$$

Note that the angular momentum in the rotating frame (constructed using the conjugate momentum, $\mathbf{p}$) is the same as the angular momentum operator in the stationary frame,

$$\mathbf{L} = \mathbf{r} \times \mathbf{p} = \mathbf{r} \times \mathbf{p_0} = \mathbf{L}_0\,. \tag{2.16}$$

The Hamiltonian in the rotating frame is then,

$$\begin{aligned} \mathcal{H} &= \mathbf{p} \cdot \mathbf{v} - \mathcal{L} = mv^2 + m\mathbf{v} \cdot (\Omega \times \mathbf{r}) - \frac{1}{2}mv^2 - m\mathbf{v} \cdot (\Omega \times \mathbf{r}) - \frac{1}{2}m\left(\Omega \times \mathbf{r}\right)^2 \\ &= \frac{1}{2}mv^2 - \frac{1}{2}m\left(\Omega \times \mathbf{r}\right)^2 \\ &= \frac{1}{2}m\left(\mathbf{v}_0 - \Omega \times \mathbf{r}\right)^2 - \frac{1}{2}m\left(\Omega \times \mathbf{r}\right)^2 \\ &= \frac{1}{2}mv_0^2 - \Omega \cdot (\mathbf{r} \times \mathbf{p_0}) = \frac{p_0^2}{2m} - \Omega \cdot \mathbf{L} \\ &= \mathcal{H}_0 - \Omega \cdot \mathbf{L}_0\,. \end{aligned} \tag{2.17}$$

This coordinate transformation facilitates the calculation of the ground state in the laboratory frame since it renders the Hamiltonian time independent. While this example

is for a single classical particle, the analogy can be extended to other systems with many particles as long as the system is undergoing uniform rotation [45].

2.2.3 Bose-Hubbard Hamiltonian in rotating-frame coordinates

Using the standard procedure described in the previous subsection and Ref. [45], the Hamiltonian for bosons in a rotating optical lattice in the reference frame co-rotating with the same angular velocity Ω about the z-axis is

$$\hat{\mathcal{H}} = \hat{\mathcal{H}}_0 - \int d\mathbf{x}\, \hat{\Phi}^\dagger(\mathbf{x}) \Omega L_z \hat{\Phi}(\mathbf{x}) = \hat{\mathcal{H}}_0 + \hat{\mathcal{H}}_L \tag{2.18}$$

where $\hat{\mathcal{H}}_0$ is the Hamiltonian in the laboratory frame and $\hat{\mathcal{H}}_L$ is the additional term due to the rotation. The angular momentum is

$$L_z = -i\hbar(x\partial_y - y\partial_x)\,. \tag{2.19}$$

Substituting for the field operator (Eq. 2.5), the angular velocity dependent portion of the Hamiltonian can be written as,

$$\hat{\mathcal{H}}_L = i\hbar\Omega \sum_{\langle i,j\rangle} \hat{a}_i^\dagger \hat{a}_j \int d\mathbf{x}\, W_S^*(\mathbf{x}-\mathbf{x}_i)\,(x\partial_y - y\partial_x)\, W_S(\mathbf{x}-\mathbf{x}_j)\,. \tag{2.20}$$

Again, the Wannier functions can be factorized into x- and y-dependent parts. For the instance of a 2D lattice created by retro-reflected laser beams, this is possible if orthogonal polarizations are used for the two directions. The overlap integral can be computed numerically for different lattice geometries and lattice depths and Eq. 2.20 reduces to,

$$\hat{\mathcal{H}}_L = -i\hbar\Omega \sum_{\langle i,j\rangle} K_{ij} \left(\hat{a}_i \hat{a}_j^\dagger - \hat{a}_i^\dagger \hat{a}_j\right) \tag{2.21}$$

where Ω is in units of $E_R/\hbar$ and

$$K_{ij} = \frac{\beta}{d}(x_i y_j - x_j y_i) \tag{2.22}$$

$$\beta \equiv \int dx\, W_S^*(x-d)\partial_x W_S(x)\,. \tag{2.23}$$

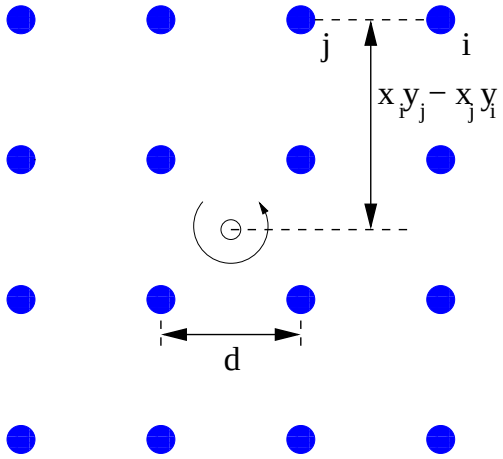

Figure 2.3: Schematic for a 4×4 lattice rotating in the counter-clockwise direction. Sites labeled i and j are nearest neighbors. The rotation-driven hopping between neighbouring sites is governed by the parameter $K_{ij} = \beta(x_i y_j - x_j y_i)/d$, where β is given by the overlap integral Eq. 2.23 and the second factor is the perpendicular distance of the line joining the two neighboring sites from the center of rotation.

The term in the parenthesis in Eq. 2.22 is the perpendicular distance of the line joining sites i and j from the center of rotation (Fig. 2.3). In Eq. 2.23, β is an overlap integral dependent on the geometry and form of the lattice. Note that the Wannier functions above are one-dimensional. The overlap integral can be computed by numerically evaluating the lowest-band Bloch solutions to the Mathieu equation and fitting a cubic spline to the spatial Fourier transform of the complete set to obtain a smooth expression for the Wannier function $W_S(\mathbf{x} - \mathbf{x_i})$. The integration is then performed numerically over an interval of six sites which adequately covers the extent of the adjacent Wannier functions in the tight-binding regime ($V_0 > 5E_R$) with the error in the norm smaller than 0.1%.

Substituting Eq. 2.21 into Eq. 2.18, the lowest-band modified Bose-Hubbard

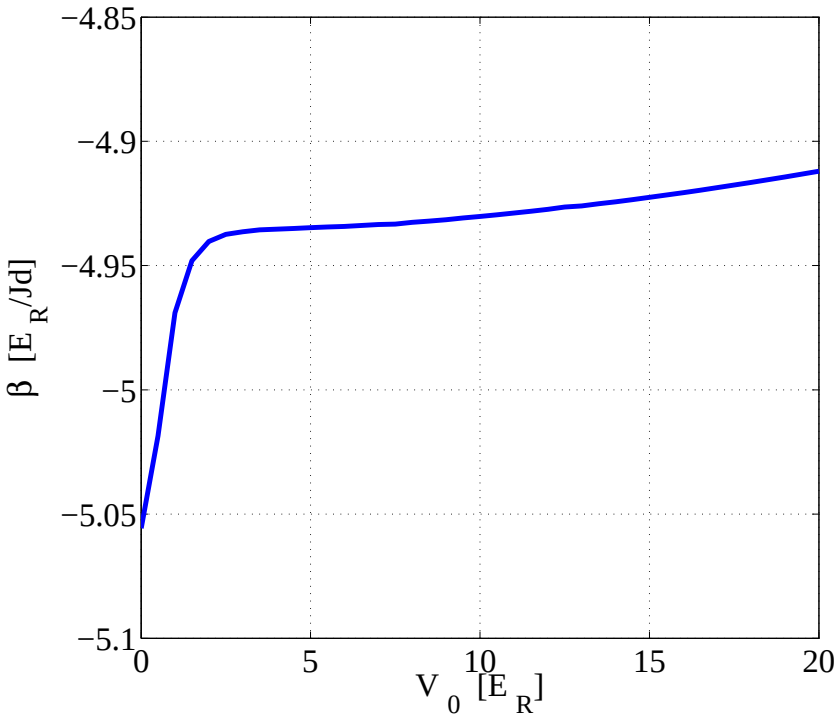

Figure 2.4: The overlap integral β (Eq. 2.23) is plotted as a function of lattice depth $V_0 s$. The y-axis is in units of the hopping energy. In the tight-binding regime, $\beta \approx -(\pi^2/2)Jd/E_R$.

Hamiltonian can be written as,

$$\hat{\mathcal{H}}_1 = -J\sum_{\langle i,j\rangle}\left(\hat{a}_i\hat{a}_j^\dagger + \hat{a}_i^\dagger\hat{a}_j\right) + \epsilon\sum_i \hat{n}_i + \frac{U}{2}\sum_i \hat{n}_i\left(\hat{n}_i - 1\right) - i\hbar\Omega\sum_{\langle i,j\rangle} K_{ij}\left(\hat{a}_i\hat{a}_j^\dagger - \hat{a}_i^\dagger\hat{a}_j\right). \tag{2.24}$$

Qualitative and quantitative discussion of the merits and shortfalls of this Hamiltonian will be held off until after the next section where an alternative formulation is presented.

2.3 Derivation using a local gauge transform

In this section, we present the derivation of a modified Bose-Hubbard Hamiltonian using a symmetric gauge transformation. The angular velocity Ω is mapped onto the parameter α used commonly in quantum Hall literature. An analogy of this system is

drawn with that of Bloch electrons in a magnetic field by looking at the single-particle energy spectrum.

The system to be described is a cloud of a fixed number of bosons rotating with an angular velocity Ω about the z-axis. This cloud is trapped in a 2D optical lattice co-rotating with the same angular velocity Ω in the presence of an additional, superimposed two-dimensional harmonic trapping potential of frequency ω. For a non-rotating system ($\Omega = 0$), the Hamiltonian $\hat{\mathcal{H}}_0$ has components corresponding to the kinetic energy, the lattice and harmonic trapping potentials, and the energy due to interactions between particles. As described in Sec 2.2.2, the effect of rotation is included by using time-independent rotating-frame coordinates by means of the transformation, $\hat{\mathcal{H}} = \hat{\mathcal{H}}_0 - \int d\mathbf{x}\hat{\Phi}^\dagger(\mathbf{x})\Omega L_z\hat{\Phi}(\mathbf{x})$ [45]. The Hamiltonian in time-independent rotating frame coordinates is,

$$\hat{\mathcal{H}} = \int d\mathbf{x}\ \hat{\Phi}^\dagger(\mathbf{x})\left[-\frac{\hbar^2}{2m}\nabla^2 + V^{\rm lat}(\mathbf{x}) + V^{\rm t}(\mathbf{x}) + \frac{g}{2}\hat{\Phi}^\dagger(\mathbf{x})\hat{\Phi}(\mathbf{x}) - \Omega L_z\right]\hat{\Phi}(\mathbf{x})\,. \quad (2.25)$$

The sinusoidal square lattice potential $V^{\rm lat}$ is described by Eq. 2.1. In this section, we introduce a trapping potential, $V^{\rm t}(\mathbf{x}) = m\omega^2 r^2/2$ with $r \equiv |\mathbf{x}|$. This new term will be useful in studying the system in the lowest Landau level limit. Note that this was not included in $\hat{\mathcal{H}}_1$. Equation (2.25) can now be rewritten as,

$$\begin{aligned}\hat{H} &= \int d\mathbf{x}\ \hat{\Phi}^\dagger(\mathbf{x})\left[\frac{1}{2m}\left(\frac{\hbar}{i}\partial_x + m\Omega y\right)^2 + \frac{1}{2m}\left(\frac{\hbar}{i}\partial_y - m\Omega x\right)^2\right.\\ &\quad \left. + \frac{1}{2m}\left(\omega^2 - \Omega^2\right)r^2 + \frac{g}{2}\hat{\Phi}^\dagger\hat{\Phi}\right]\hat{\Phi}(\mathbf{x}) \quad (2.26)\\ &= \int d\mathbf{x}\ \hat{\Phi}^\dagger(\mathbf{x})\left[\frac{\mathbf{\Pi}^2}{2m} + V^{\rm lat}(\mathbf{x}) + \frac{1}{2}m(\omega^2 - \Omega^2)r^2 + \frac{g}{2}\hat{\Phi}^\dagger\hat{\Phi}\right]\hat{\Phi}(\mathbf{x})\,. \quad (2.27)\end{aligned}$$

Here, the covariant momentum is,

$$\mathbf{\Pi}(\mathbf{x}) \equiv -i\hbar\nabla + m\mathbf{A}(\mathbf{x})\,, \quad (2.28)$$

and the equivalent of a magnetic vector potential (in the symmetric gauge) stemming from the rotation is,

$$\mathbf{A}(\mathbf{x}) \equiv \mathbf{x} \times \mathbf{\Omega}\,. \quad (2.29)$$

The field operator $\hat{\Phi}$ can be expanded in several ways. One common expansion for the stationary lattice problem uses the Wannier orbitals $W_S^l(\mathbf{x}-\mathbf{x_i})$ introduced in Sec. 2.2.1, where the sites are indexed by i and the bands by l [82]. If the energy separation between the lowest Bloch band and the first excited band is large compared to the interaction energy and the angular velocity is low ($\hbar\Omega \sim 0.01E_R$), then a good description is obtained by retaining only Wannier orbitals constructed from the lowest Bloch band, *i. e.*, $l = 0$. With this approximation, the phase of the single-particle wavefunction is flat within a particular lattice site with sharp gradients at site boundaries (Sec. 2.5 expands on this topic). However, for larger angular velocities ($\hbar\Omega \sim 0.1E_R$), the ΩL_z-term mixes in higher bands to a non-negligible extent. The primary effect of this mixing is to modify the phase structure within sites. Consider a modified Wannier basis given by

$$W_R(\mathbf{x}-\mathbf{x_i}) = \exp\left(-i\frac{m}{\hbar}\int_{\mathbf{x_i}}^{\mathbf{x}} \mathbf{A}(\mathbf{x}')\, d\mathbf{x}'\right) W_S(\mathbf{x}-\mathbf{x_i})\,, \tag{2.30}$$

where $W_R(\mathbf{x}-\mathbf{x_i})$ and $W_S(\mathbf{x}-\mathbf{x_i})$ are connected by the transform,

$$\mathbf{\Pi} W_R(\mathbf{x}-\mathbf{x_i}) = \exp\left(-i\frac{m}{\hbar}\int_{\mathbf{x_i}}^{\mathbf{x}} \mathbf{A}(\mathbf{x}')\, d\mathbf{x}'\right) \frac{\hbar}{i}\nabla W_S(\mathbf{x}-\mathbf{x_i})\,. \tag{2.31}$$

This choice captures some of the effect of higher bands by making the azimuthal phase gradient within a site proportional to Ω. The lower limit in the integral is chosen to coincide with the site center to ensure that at $\mathbf{x} = \mathbf{x_i}$ the Wannier orbital is real, *i. e.*, $W_R(0) = W_S(0)$. A path of integration needs to be chosen such that the basis set defined by $W_R(\mathbf{x}-\mathbf{x_i})$ is orthonormal. In addition, calculations for the square-lattice problem are greatly simplified if the choice of path allows for each two-dimensional Wannier orbital to be decoupled into a product of one-dimensional Wannier orbitals. One particular choice of path that meets both criteria is along straight lines parallel to the lattice axes (dashed lines in Fig. 2.5).

Testing orthonormality: The relevant path integral can be broken into two

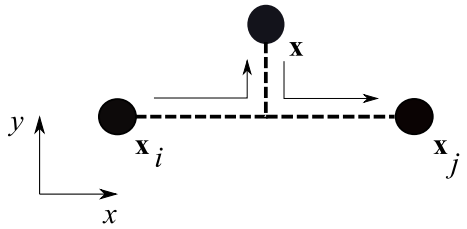

Figure 2.5: A particular choice for the path of integration (Eq. 2.32) is along straight lines (dashed) parallel to the lattice axes.

parts,

$$\begin{aligned}\int_{\mathbf{x}_i}^{\mathbf{x}} \mathbf{A}(\mathbf{x}').d\mathbf{x}' &= \int_{x_i\hat{x}+y_i\hat{y}}^{x\hat{x}+y_i\hat{y}} \mathbf{A}(\mathbf{x}').d\mathbf{x}' + \int_{x\hat{x}+y_i\hat{y}}^{x\hat{x}+y\hat{y}} \mathbf{A}(\mathbf{x}').d\mathbf{x}' = \int_{x_i}^{x} \Omega y_i dx' + \int_{y_i}^{y} (-\Omega x)\, dy' \\ &= \Omega y_i(x-x_i) - \Omega x(y-y_i) = \Omega\left[2xy_i - x_iy_i - xy\right] \qquad (2.32)\end{aligned}$$

The norm of the newly defined Wannier functions is trivially equal to unity since the new Wannier functions only differ by a phase factor. Now consider the inner product of Wannier functions centered on nearest neighboring sites. This quantity should be equal to zero for the orthogonality condition to be satisfied.

$$\begin{aligned}&\int d\mathbf{x}\; W_R^*(\mathbf{x}-\mathbf{x}_i)W_R(\mathbf{x}-\mathbf{x}_j) \\ &\quad= \int d\mathbf{x}\; e^{i(m\Omega/\hbar)(2xy_i - x_iy_i - xy - 2xy_j + x_jy_j + xy)} W_S^*(\mathbf{x}-\mathbf{x}_i)W_S(\mathbf{x}-\mathbf{x}_j) \\ &\quad= e^{i(m\Omega/\hbar)(x_iy_i + x_jy_j)}\left[\int dx\; e^{i(m\Omega/\hbar)(2x(y_i-y_j))} W_S^*(x-x_i)W_S(x-x_j)\right. \\ &\qquad\left.\times \int dy\; W_S^*(y-y_i)W_S(y-y_j)\right] \qquad (2.33)\end{aligned}$$

To evaluate Eq. 2.33, we consider the two cases of neighboring sites along the x- and y-directions respectively:

- Case i. $x_j = x_i \pm d; y_j = y_i$

$$\begin{aligned}&\int d\mathbf{x}\; W_R^*(\mathbf{x}-\mathbf{x}_i)W_R(\mathbf{x}-\mathbf{x}_j) = e^{i(m\Omega/\hbar)(x_iy_i + x_jy_j)} \\ &\times\left[\int dx\; W_S^*(x-x_i)W_S(x-x_j)\int dy\; W_S^*(y-y_i)W_S(y-y_i)\right] = 0\,. \qquad (2.34)\end{aligned}$$

- Case ii. $x_j = x_i; y_j = y_i \pm d$

$$\int d\mathbf{x}\, W_R^*(\mathbf{x}-\mathbf{x}_i) W_R(\mathbf{x}-\mathbf{x}_j) = e^{i(m\Omega/\hbar)(x_i y_i + x_j y_j)} \times \left[\int dx\, e^{\mp i(m\Omega/\hbar)(2xd)} W_s^*(x-x_i) W_s(x-x_i) \int dy\, W_s^*(y-y_i) W_s(y-y_j) \right] = 0\,. \tag{2.35}$$

Hence the Wannier basis set represented by $W_R(\mathbf{x}-\mathbf{x}_i)$ is orthonormal and can be factorized into one-dimensional Wannier functions along the cartesian axes for the path that we have chosen (Fig. 2.5). Note that this path is not unique. Also, factorization of the 2D Wannier function, while it simplifies computations, is not necessarily required to to evaluate the overlap integrals. A quantitative assessment using imaginary-time propagation techniques presented in the next section shows that the modified Wannier basis set $W_R(\mathbf{x}-\mathbf{x_i})$ describes the phase gradient within a site better than the regular Wannier basis $W_S(\mathbf{x}-\mathbf{x_i})$.

Using the modified Wannier basis $W_R(\mathbf{x}-\mathbf{x_i})$, the field operator can now be expressed as

$$\hat{\Phi}(\mathbf{x}) = \sum_i \hat{a}_i W_R(\mathbf{x}-\mathbf{x_i})\,, \tag{2.36}$$

where $\hat{a}_i$ is a site-specific annihilation operator. A modified Bose-Hubbard Hamiltonian is obtained by substituting Eq. (2.36) into Eq. (2.27) and using the tight-binding approximation,

$$\begin{aligned}\hat{\mathcal{H}}_2 = &-\sum_{\langle i,j\rangle} \left(J + \frac{m(\Omega^2-\omega^2)}{2} A_1 \right) (\hat{a}_i \hat{a}_j^\dagger e^{i\phi_{ij}} + \hat{a}_i^\dagger \hat{a}_j e^{-i\phi_{ij}}) \\ &+ \sum_i \left(\epsilon - \frac{m(\Omega^2-\omega^2)}{2}(r_i^2 + A_2) \right) \hat{n}_i + \frac{U}{2}\hat{n}_i(\hat{n}_i - 1)\,,\end{aligned} \tag{2.37}$$

where $\langle i,j\rangle$ indicates the sum over nearest-neighbor site pairs and $\hat{n}_i \equiv \hat{a}_i^\dagger \hat{a}_i$ is the number operator. The parameters J and ϵ are the overlap integrals defined in Eqs. 2.7 and 2.8 respectively and are identical to the hopping and onsite zero-point energies

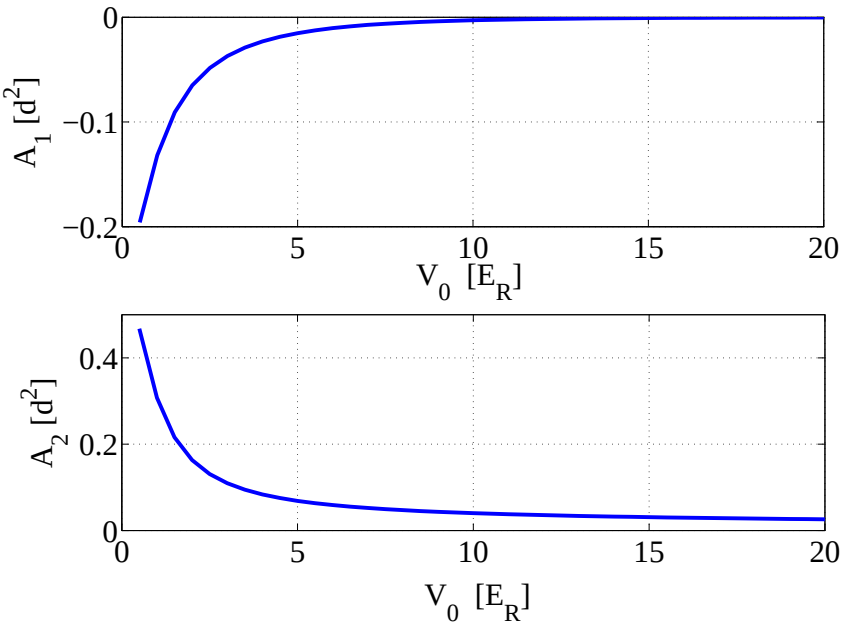

Figure 2.6: Overlap integrals A_1 (Eq. 2.39) and A_2 (Eq. 2.40) as a function of lattice depth for a standing-wave optical lattice described by $V^{(\mathrm{lat})}(\mathbf{x}) = V_0(\cos^2(\pi x/d) + \cos^2(\pi y/d))$. The lattice depth is given in units of the recoil energy $E_R = \hbar^2\pi^2/2md^2$. A_1 and A_2 are in units of d^2. In the tight-binding regime ($V_0/E_R > 5$), $A_1 \approx -0.273\exp\left(-V_0^{0.656}\right)$ and $A_2 \approx 0.368\exp\left(-V_0^{0.337}\right)$.

associated with the standard Bose-Hubbard model [28]. The phase in the hopping term is

$$\phi_{ij} \equiv \frac{m}{\hbar}\int_{\mathbf{x_j}}^{\mathbf{x_i}} \mathbf{A}(\mathbf{x}')\cdot d\mathbf{x}' = \frac{m\Omega}{\hbar}(x_i y_j - x_j y_i)\,. \tag{2.38}$$

Here, the angular velocity Ω is expressed in units of $E_R/\hbar$. The modifications to the hopping and onsite energies due to rotation are proportional to $(\Omega^2 - \omega^2)$ and to two new overlap parameters given by

$$A_1 \equiv \int dx\; W_S^*(x - x_i)\;(x - x_i)^2\; W_S(x - x_j)\,, \tag{2.39}$$

$$A_2 \equiv 2\int dx\; W_S^*(x - x_i)\;(x - x_i)^2\; W_S(x - x_i)\,. \tag{2.40}$$

There is an additional factor of two in A_2 because of identical onsite overlaps along the x- and y-directions. Changes in the lattice potential affect both new parameters

(Fig. 2.6). The last term in the Hamiltonian describes the onsite interaction energy (Eq. 2.10) which remains unchanged.

There are three main approximations implicit in our approach. The first is the tight-binding approximation. This approximation becomes valid when V_0 exceeds $5E_R$. Our numerical calculations are well in the tight-binding regime with typical lattice depths, $V_0 = 10E_R$. The second approximation is the use of infinite-lattice Wannier functions for a finite lattice. Due to this, edge effects are not accounted for correctly when only Wannier functions from the lowest band are used although the approximation gets better with increased lattice size. The third and most severe approximation stems from using only the lowest Bloch band. While this approximation is perfectly valid for stationary systems, it comes under pressure in the presence of rotation as higher states are mixed in.

Note that the modified Bose-Hubbard Hamiltonian in Eq. 2.37 is obtained using the symmetric gauge for the vector potential $\mathbf{A}(\mathbf{x})$. An expression equivalent to that used by Jaksch *et al.* [39] can be obtained using the Landau gauge in which $\mathbf{A}_L(\mathbf{x}) = \Omega y\hat{x}$ and setting the trapping frequency equal to the angular velocity ($\omega = \Omega$). The two different Hamiltonians are connected though the transformation $\hat{\mathcal{H}}_{\text{Landau}} = P_L\hat{\mathcal{H}}_2P_L^{-1}$ where $\hat{\mathcal{H}}_{\text{Landau}}$ is the Hamiltonian in the Landau gauge and,

$$P_L = \exp\left(i\frac{m\Omega}{\hbar}\int_{\mathbf{x_0}}^{\mathbf{x}} x'dy'\right) . \tag{2.41}$$

One useful way of describing the difference between the two gauge choices in the context of the rotating lattice problem is to show how a particle picks up phase on going around a plaquette. In the symmetric gauge, the particle can pick up phase along four sides of the plaquette (defined below) while in the Landau gauge, the particle picks up phase only along either the x-direction or the y-direction. Other salient features of the latter are illustrated in Sec. 2.5.3 where connections are drawn to the Harper equation using the Landau gauge.

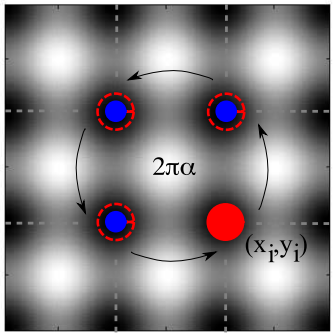

Figure 2.7: Schematic for a particle going around a plaquette in a square lattice. Regions shaded dark correspond to lattice sites and the light regions indicate maxima in the lattice potential. In the tight-binding regime, the particle can tunnel through the grey regions connecting sites. Using Eq. 2.38, it can be shown that the particle picks up a phase of $2\pi\alpha = 2md^2\Omega/\hbar$ as it returns to its original position as marked by the solid circle. If the path of the particle encloses P plaquettes then the phase picked up is $2\pi\alpha P$.

2.3.1 Mapping angular velocity onto winding number

Several two-dimensional problems are characterized by multiply-connected domains where singularities in the topology are typically due to quantized magnetic flux lines (*e. g.* Aharonov-Bohm effect [2]) or strongly repulsive particles (*e. g.* quantum Hall effect [42, 78]). In this context, it is useful to introduce a winding number $2\pi\alpha$ that describes the phase picked up by a particle when it goes around such a singularity. Inaccessible regions in the topology can also be created by means of a suitable restrictive potential.

Consider the lattice potential shown in Fig. 2.7. The light shaded regions correspond to peaks in the lattice potential that are inaccessible to particles in the tight binding regime. The phase accumulated by a particle adiabatically going around one such simply-connected inaccessible region (a plaquette) can be calculated by first breaking the loop into four parts as indicated. For each part, the phase change associated with destroying a particle at a site and creating it in a neighboring site is given by

Eq. 2.38. This phase is identical to that associated with the hopping term in the Hamiltonian (Eq. 2.37). The relationship between the angular velocity Ω and α is obtained by summing the contributions and is given by

$$\alpha = \frac{md^2}{\pi\hbar}\Omega = \frac{\pi}{2}\left(\frac{\hbar\Omega}{E_R}\right) . \tag{2.42}$$

For large Ω, in the absence of a lattice, the vortex density is given by $n_v = m\Omega/\pi\hbar$ [65] and α describes the number of vortices contained in a cell of area d^2.

2.4 Method

We exploit Hamiltonians $\hat{\mathcal{H}}_1$ and $\hat{\mathcal{H}}_2$ by first constructing a truncated Fock-number basis for the desired number of sites. In the two-state approximation for strongly repulsive (hard-core) bosons, the allowed Fock states for each site are $|0\rangle$ and $|1\rangle$ and each state can be considered as a binary number where each place corresponds to a site. If the particle number is not fixed, the largest system that is numerically tractable on our computers[4] is four particles in a 16-site lattice. However, both Hamiltonians, $\hat{\mathcal{H}}_1$ and $\hat{\mathcal{H}}_2$ are number-conserving and are therefore block-diagonal with each block corresponding to a fixed number of particles. The problem of determining the basis set for each block (*i. e.* for a fixed number of particles) can be solved recursively where the n^{th} particle is moved around as the remaining $n-1$ particles are held fixed. This allows for an order of magnitude improvement in the size of the system that can be studied (up to 4 particles in a 36-site lattice). In addition, larger systems can be studied for a smaller numbers of particles (2 particles in a 256-site lattice). The lattices are truncated using infinite box boundary conditions.

Using this basis set, the diagonal components of Hamiltonian are easy to construct. The off-diagonal components are obtained by identifying states which are connected by a hopping term. For example, if the basis states in the two-state approx-

[4] The basic configuration used for these calculations was a desktop machine with a 3.6-3.8 GHz dual processor CPU with 2 GB of RAM.

imation are in an ordered set then the hopping term $\hat{a}_i^\dagger \hat{a}_j$ connects states which are $2^{j-1} - 2^{i-1}$ places apart. The Hamiltonian obtained is sparse and the lowest eigenvalues/eigenstates can be extracted using standard *Matlab* or *Mathematica* routines to obtain both, energy spectra and energy eigenstates. The version of *Matlab* we used could diagonalize matrices of maximum size $\sim 60,000 \times 60,000$ corresponding to 4 particles in a 36-site lattice (Fig. 6.1). Operators can be constructed in a manner similar to that used for building the Hamiltonian. Expectation values are obtained using matrix multiplication.

2.5 Comparison between approaches

Sections 2.2 and 2.3 presented two different Hamiltonians, $\hat{\mathcal{H}}_1$ (Eq. 2.24) and $\hat{\mathcal{H}}_2$ (Eq. 2.37). An important step at this juncture is to reconcile the two — both qualitatively and quantitatively. Comparisons establish that both $\hat{\mathcal{H}}_1$ and $\hat{\mathcal{H}}_2$ share similar symmetry properties and are equivalent for small α. However, as α gets larger, the description afforded by $\hat{\mathcal{H}}_1$ suffers because the phase space it describes is confined to the lowest Bloch band. The Hamiltonian $\hat{\mathcal{H}}_2$ fares better for bigger α by including an approximate description for the phase modification due to higher bands. Quantitative differences between the two approaches for small systems are studied using imaginary-time propagation techniques.

2.5.1 Equivalence in the small α limit

In this discussion, $\hat{\mathcal{H}}_1$ is first rewritten in terms of α and then shown to be equivalent to first order to a Taylor expansion in α of $\hat{\mathcal{H}}_2$.

The site-dependent hopping parameter K_{ij} in $\hat{\mathcal{H}}_1$ given by Eq. 2.22 can be rewritten in terms of ϕ_{ij} (Eq. 2.38),

$$K_{ij} \equiv \beta \frac{\phi_{ij}}{\pi \alpha} \tag{2.43}$$

Also, from Fig. 2.4, we know that in the tight-binding regime,

$$\beta \approx -4.93J \sim -\frac{\pi^2}{2}J \tag{2.44}$$

An alternative expression for the rotation-dependent portion of $\hat{\mathcal{H}}_1$ can be obtained by substituting for Ω (Eq. 2.42) and using the just defined relationships in the expression for $\hat{\mathcal{H}}_L$ (Eq. 2.21),

$$\begin{aligned}\hat{\mathcal{H}}_L &= -i\hbar\Omega \sum_{\langle i,j\rangle} K_{ij}\left(\hat{a}_i\hat{a}_j^\dagger - \hat{a}_i^\dagger\hat{a}_j\right) = i\frac{2}{\pi}\alpha\cdot\frac{\pi^2}{2}J\sum_{\langle i,j\rangle}\frac{\phi_{ij}}{\pi\alpha}\left(\hat{a}_i\hat{a}_j^\dagger - \hat{a}_i^\dagger\hat{a}_j\right)\\ &= iJ\sum_{\langle i,j\rangle}\phi_{ij}\left(\hat{a}_i\hat{a}_j^\dagger - \hat{a}_i^\dagger\hat{a}_j\right)\end{aligned} \tag{2.45}$$

Replacing for $\hat{\mathcal{H}}_L$ in Eq. 2.24, we get,

$$\begin{aligned}\hat{\mathcal{H}}_1 &= -J\sum_{\langle i,j\rangle}\left(\hat{a}_i\hat{a}_j^\dagger + \hat{a}_i^\dagger\hat{a}_j\right) - iJ\sum_{\langle i,j\rangle}\phi_{ij}\left(\hat{a}_i\hat{a}_j^\dagger - \hat{a}_i^\dagger\hat{a}_j\right) + \epsilon\sum_i\hat{n}_i + \frac{U}{2}\sum_i\hat{n}_i\left(\hat{n}_i-1\right)\\ &= -J\sum_{\langle i,j\rangle}\left[\hat{a}_i\hat{a}_j^\dagger(1+i\phi_{ij}) + \hat{a}_i^\dagger\hat{a}_j(1-i\phi_{ij})\right] + \epsilon\sum_i\hat{n}_i + \frac{U}{2}\sum_i\hat{n}_i\left(\hat{n}_i-1\right)\,.\end{aligned} \tag{2.46}$$

Now consider $\hat{\mathcal{H}}_2$ without a harmonic trapping potential. The small-α Taylor expansion for the exponential in Eq. 2.37 is,

$$\exp\left(i\phi_{ij}\right) = \exp\left[i\pi\alpha\left(x_iy_j - x_jy_i\right)\right] = 1 + i\phi_{ij} + \mathcal{O}(\alpha^2) + \ldots \tag{2.47}$$

Substituting for Ω in Eq. 2.37 and expanding in α,

$$\begin{aligned}\hat{\mathcal{H}}_2 \approx &-\sum_{\langle i,j\rangle}\left(J + \frac{m\pi^2\hbar^2}{2m^2d^4}A_1\alpha^2\right)\left[\hat{a}_i\hat{a}_j^\dagger(1+i\phi_{ij}+\mathcal{O}(\alpha^2)) + \hat{a}_i^\dagger\hat{a}_j(1-i\phi_{ij}+\mathcal{O}(\alpha^2))\right]\\ &+\sum_i\left(\epsilon - \frac{m\pi^2\hbar^2}{2m^2d^4}(r_i^2+A_2)\alpha^2\right)\hat{n}_i + \frac{U}{2}\hat{n}_i(\hat{n}_i-1)\,.\end{aligned} \tag{2.48}$$

Dropping terms $\mathcal{O}(\alpha^2)$ and higher, we arrive at,

$$\hat{\mathcal{H}}_2 \approx -J\sum_{\langle i,j\rangle}\left[\hat{a}_i\hat{a}_j^\dagger(1+i\phi_{ij}) + \hat{a}_i^\dagger\hat{a}_j(1-i\phi_{ij})\right] + \epsilon\sum_i\hat{n}_i + \frac{U}{2}\hat{n}_i(\hat{n}_i-1)\,, \tag{2.49}$$

which is identical to Eq. 2.46. Hence the two Hamiltonians are equivalent in the tight-binding regime for small α to $\mathcal{O}(\alpha)$.

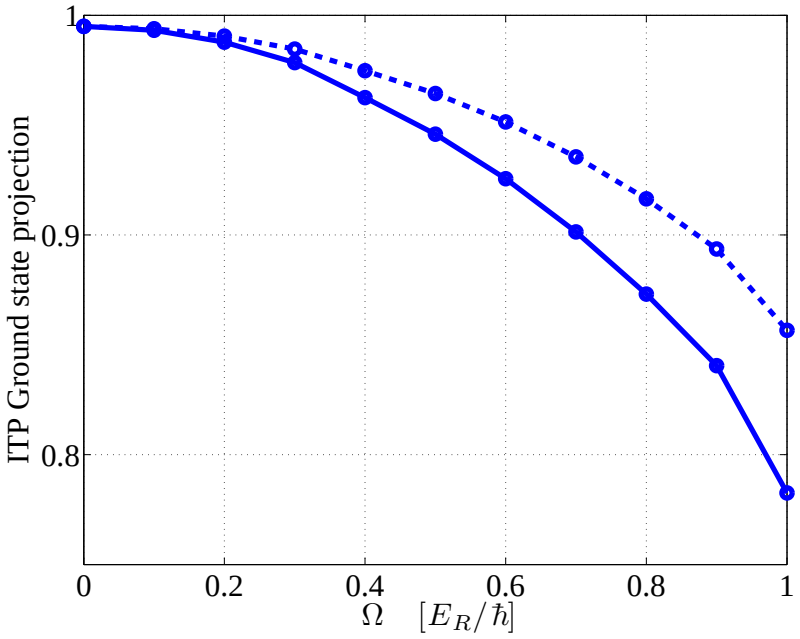

Figure 2.8: Projection of the ITP ground state onto the Hilbert space spanned by the eigenvectors obtained using $\hat{\mathcal{H}}_1$ (solid line) (Eq. 2.24) and $\hat{\mathcal{H}}_2$ (dashed line) (Eq. 2.37) for a 2×2 lattice with a lattice depth of $V_0 = 10E_R$. The overlap is good even up to $\Omega = E_R/\hbar \sim 50J$ where J is the hopping energy.

2.5.2 Quantitative comparison

Many aspects of studying the characteristics of bosons in a rotating optical lattice map onto the extensively studied problem of Bloch electrons in the presence of a magnetic field [43, 14, 82, 36]. This subsection makes a connection with the electron problem, while exploring, in parallel, the limitations of using the lowest-band Bose-Hubbard Hamiltonian. A Hamiltonian similar to $\hat{\mathcal{H}}_2$ has been used earlier to study bosons in an optical lattice in the presence of an effective magnetic field [39, 60] and for bosons in a rotating optical lattice [86].

In this subsection, the two approaches discussed in Secs. 2.2 and 2.2 are compared with results for a single particle obtained from imaginary time propagation (ITP) in a 2×2 lattice. The ITP is performed using the continuous first-quantized Hamiltonian *i. e.* without invoking Wannier functions. We reach three conclusions:

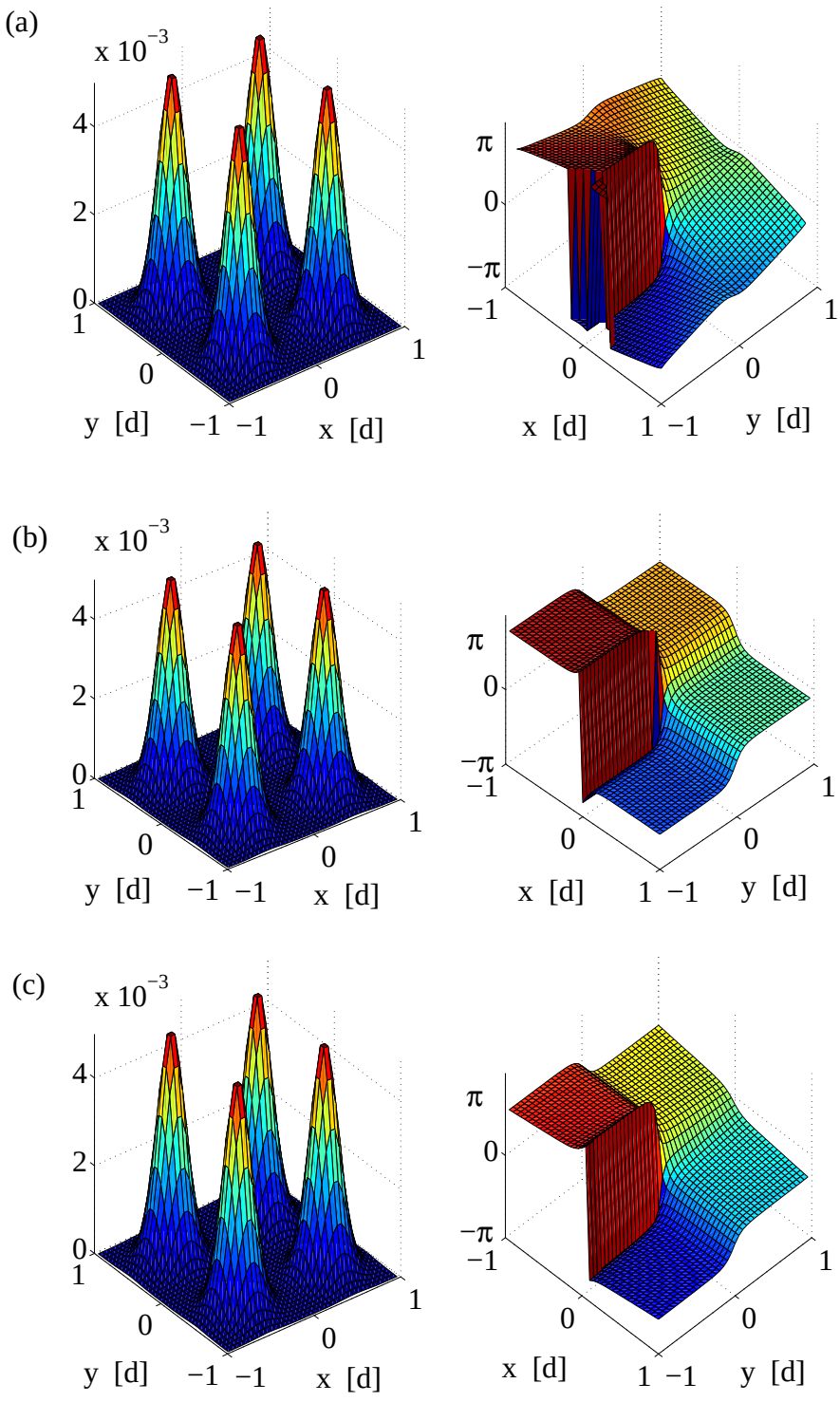

Figure 2.9: Spatial ground state number density (left) and phase (right) for one particle in a 2×2 sinusoidal lattice with $\Omega = 0.5E_R/\hbar$ and $V_0 = 10E_R$ obtained using (a) Imaginary time propagation, (b) Hamiltonian $\hat{\mathcal{H}}_1$ (Eq. 2.24) and (c) Hamiltonian $\hat{\mathcal{H}}_2$ (Eq. 2.37).

Firstly, the ground state of the Hamiltonian $\hat{\mathcal{H}}_1$ described in Eq. 2.24 no longer depends on the increase in Ω once a maximum phase difference of $\pi/2$ between neighboring sites has been reached,*i. e.*, all the vortex entry transitions possible within the lowest band have occurred. For one particle in a 2×2 lattice, the corresponding maximum phase winding is 2π. This limitation does not apply to the Hamiltonian $\hat{\mathcal{H}}_2$ (Eq. 2.37).

Secondly, the Hilbert spaces spanned by the eigenstates of both Hamiltonians Eq. 2.24 and Eq. 2.37 capture most of the exact ground state wavefunction for $\hbar\Omega \leq E_R$. Note that $\hbar\Omega \sim E_R$ is large from an experimental point of view. For the case of one particle in a 2×2 lattice, the projection of the exact wavefunction on either Hilbert space is $\geq 90\%$ for $\hbar\Omega \sim 0.5E_R$ (Fig. 2.8). Both approaches yield accurate density profiles for large Ω ($\sim E_R/\hbar$) but differ from the ITP-result, and from each other, with regard to the velocity pattern. Note that $\hat{\mathcal{H}}_1$ and $\hat{\mathcal{H}}_2$ involve different approximations to the phase gradient. The Hamiltonian $\hat{\mathcal{H}}_1$ allows for phase changes only in the region of overlap of next-neighbor Wannier functions $W_S(\mathbf{x} - \mathbf{x}_i)$,*i. e.*, yields a uniform phase around the site center (Fig. 2.9(b)). The Hamiltonian $\hat{\mathcal{H}}_2$ requires phase gradients to be proportional to Ω and allows for non-zero phase gradients within each well (Fig. 2.9(c)). The density is low between sites so the phase in that region is not as crucial as the phase within a site. Better description of the in-site phase (such as that afforded by $\hat{\mathcal{H}}_2$) gives better estimates for quantities such as the kinetic energy.

Finally, the lattice rotation frequencies at which the first vortices appear (see also Sec. 3.2) are different in the two cases over the range of interest due to the different influence of higher bands in the three formulations.

2.5.3 Harper Equation

In the previous subsection, a quantitive case was presented for the analogy between bosons in a rotating lattice and electrons in a magnetic field. In this subsection, the analogy is extended by formally obtaining the Harper equation from the modified

Bose-Hubbard Hamiltonian $\hat{\mathcal{H}}_2$ derived in Sec. 2.3. The Harper equation was the expression originally used to obtain the single particle energy spectra for a Bloch electron in a magnetic field or the 'Hofstadter butterfly' by Hofstadter in 1976 [36]. For this subsection only, a two index subscript is used to label sites with the indices representing site numbers along the x- and y- directions respectively.

Consider the modified Bose-Hubbard Hamiltonian $\hat{\mathcal{H}}_2$ (Eq. 2.37). As in the previous subsection, the centrifugal force due to the rotation ($\sim m\Omega^2 r^2/2$) is cancelled out by setting the 2D harmonic trap frequency equal to the rotation frequency. The interaction term vanishes since we are considering a single-particle picture. Including these two changes and switching to a two index notation, the modified Bose-Hubbard Hamiltonian is,

$$\hat{\mathcal{H}}_2 = -J \sum_{\langle ij,kl \rangle} \hat{a}_{ij}\hat{a}^\dagger_{kl} e^{i\phi_{ij,kl}} + \hat{a}^\dagger_{ij}\hat{a}_{kl} e^{-i\phi_{ij,kl}} \tag{2.50}$$

Kets and wavefunctions in real space can be defined in the usual manner,

$$|\psi_{ij}\rangle = \hat{a}^\dagger_{ij} |0\rangle \ , \tag{2.51}$$

$$\psi(x_i, y_j) = \langle \mathbf{x} | \psi_{ij} \rangle \, . \tag{2.52}$$

From the definition of creation and annihilation operators, the effect of the hopping term in Eq. 2.50 is to transfer a particle from one site to the next.

$$\langle \mathbf{x}| \, \hat{a}^\dagger_{i+1,j}\hat{a}_{i,j} \, |\psi_{ij}\rangle = \langle \mathbf{x}|\psi_{ij}\rangle = \psi(x_i + d, y_j) \ . \tag{2.53}$$

Now consider ϕ in the Landau gauge $\mathbf{A} = \Omega(0, x, 0)$.

$$\phi_{ij,(i+1)j} = -\frac{2m}{\hbar} \int_{i,j}^{i+1,j} \mathbf{A}(\mathbf{x}') \cdot d\mathbf{x}' = 0 \tag{2.54}$$

$$\phi_{ij,i(j+1)} = -\frac{2m}{\hbar} \int_{i,j}^{i,j+1} \mathbf{A}(\mathbf{x}') \cdot d\mathbf{x}' = -\frac{2\Omega d^2 m}{\hbar} i \tag{2.55}$$

Hence, in the Landau gauge, a particle picks up a phase hopping along the y-direction and nothing along the x-direction. For a loop around an unit cell,

$$\phi_{\text{unitcell}} = \frac{2\Omega d^2 m}{\hbar} \left[0 + (i+1) - 0 - i\right] = \frac{2\Omega d^2 m}{\hbar} = 2\pi\alpha \, . \tag{2.56}$$

Letting the Hamiltonian act on the wavefunction at one lattice site, we pick up linkages to neighboring sites. The time independent Schrödinger equation becomes,

$$\hat{\mathcal{H}}_2 \left|\Psi_{i,j}\right\rangle = -t\left(\left|\psi_{i+1,j}\right\rangle + \left|\psi_{i-1,j}\right\rangle + e^{-i2\pi\alpha x_i/a}\left|\psi_{i,j+1}\right\rangle + e^{i2\pi\alpha x_i/a}\left|\psi_{i,j-1}\right\rangle\right) = E_0\left|\psi_{i,j}\right\rangle \ , \tag{2.57}$$

or,

$$\psi\left(x_{i+1},y_j\right) + \psi\left(x_{i-1},y_j\right) + e^{-i2\pi\alpha x_i/a}\psi\left(x_i,y_{j+1}\right) + e^{i2\pi\alpha x_i/a}\psi\left(x_i,\psi_{j-1}\right) = \quad \varepsilon\psi\left(x_i,y_j\right) \ , \tag{2.58}$$

where $\varepsilon = -E_0/J$. Rewriting $x_i = md, y_j = nd$ with $m, n \in \mathbb{Z}$,

$$\psi\left((m+1)d,nd\right) + \psi\left((m-1)d,nd\right) + e^{-i2\pi\alpha m}\psi\left(md,(n+1)d\right) + e^{i2\pi\alpha m}\psi\left(md,(n-1)d\right) = \varepsilon\psi\left(md,nd\right) \ . \tag{2.59}$$

Since the coefficients are independent of n, we can assume a plane wave solution along the y-direction, *i. e.*, $\psi(md,nd) = e^{in\nu}g(m)$. Substituting this in Eq. 2.59, we get

$$e^{in\nu}g(m+1) + e^{in\nu}g(m-1) + e^{-i2\pi\alpha m + i(n+1)\nu}g(m) + e^{i2\pi\alpha m + i(n-1)\nu}g(m) = \varepsilon e^{in\nu}g(m) \, . \tag{2.60}$$

After some algebra, this becomes

$$g(m+1) + g(m-1) + \left[-\varepsilon + 2\cos\left(2\pi\alpha m - \upsilon\right)\right]g(m) = 0 \tag{2.61}$$

Equation 2.61 is called the Harper equation and, was most famously, used to study the energy spectra of a single Bloch electron in the presence of a magnetic field in 1976 by Hofstadter [36].

2.5.4 Single-particle energy spectra

Having derived the Harper equation starting from $\hat{\mathcal{H}}_2$, a useful crosscheck is to compare the single-particle energy spectrum with that for a Bloch electron in the presence of a magnetic field (Fig. 2.10a). The energy spectrum for a single particle in a

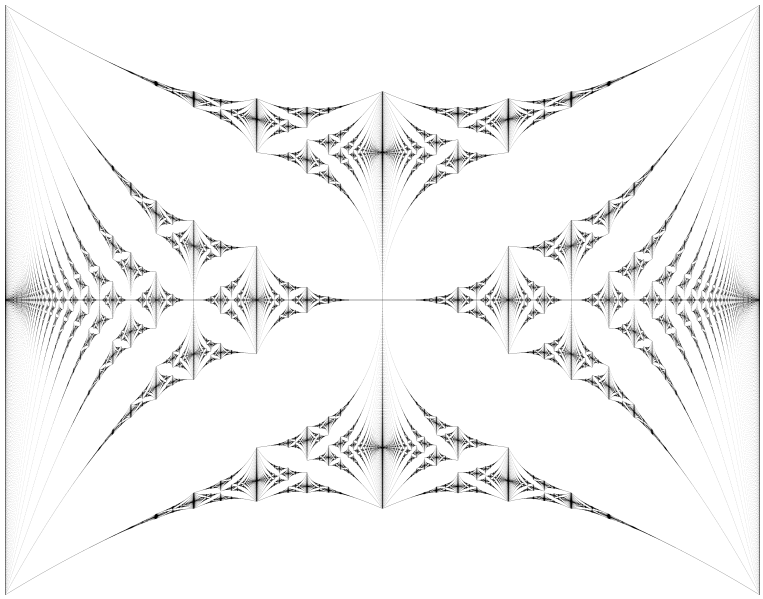

(a) Infinite lattice energy spectra for a single Bloch electron in the presence of a magnetic field.

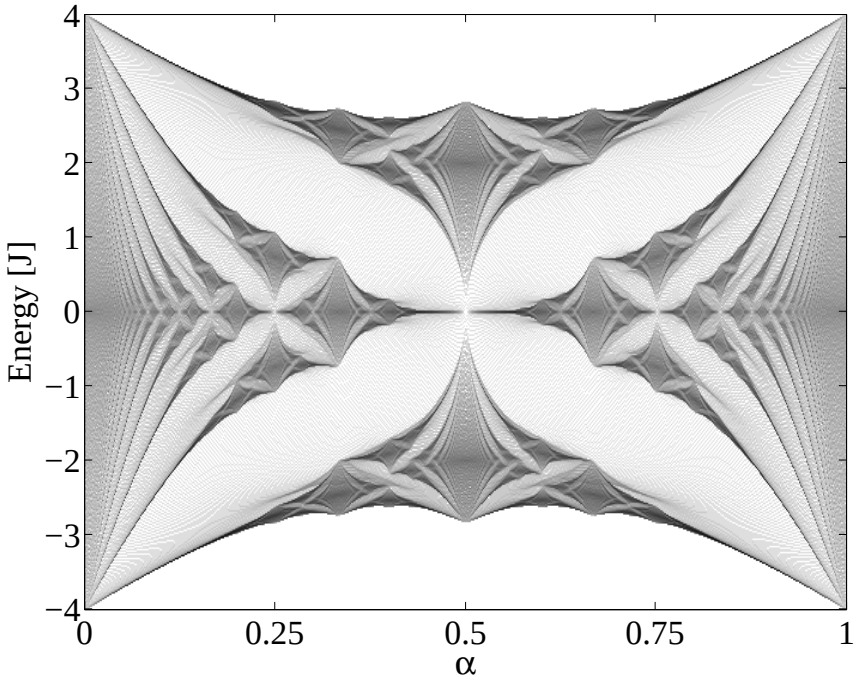

(b) Finite lattice energy spectra for a single boson in a rotating lattice

Figure 2.10: (a) This plot was obtained from the original Hofstadter paper [36]. The x-axis describes $\alpha = d^2H/2\pi(\hbar c/e)$ where H is the magnetic field and the y-axis describes energy. (b)Single particle energy spectra as a function of the rescaled angular velocity α for a 40×40 lattice. The $x-$ axis here describes $\alpha = d^2\Omega/2\pi(\hbar/2m)$ and y-axis describes energy in units of the hopping energy. Darker shading indicates greater density of states. The origin of the y-axis has been shifted to coincide with the onsite energy.

40×40 lattice obtained using exact diagonalization is plotted as a function of α in Fig. 2.10. The energy contribution due to the centrifugal force is eliminated by setting the trapping frequency equal to the angular velocity ($\omega = \Omega$). This is identical to the condition necessary to reach the highly degenerate lowest Landau level (LLL) for the same problem in the absence of a lattice. Applying the LLL condition in the lattice context has two consequences for the energy spectrum: first, the spectrum becomes periodic as a function of α with a periodicity $\Delta\alpha = 1$ and second, the spectrum is symmetric about $\alpha = 0.5$ and takes on the shape of the Hofstadter butterfly — originally used to describe the energy spectra for an electron in a periodic potential in the presence of a magnetic field [36]. For $\omega \neq \Omega$, both the symmetry of the energy spectra about $\alpha = 0.5$ and the periodicity are disrupted as the entire spectrum shifts up or down as a function of $\left(\Omega^2 - \omega^2\right)$. As shown by Analytis *et al.* [4], the fractal nature of the spectra becomes increasingly well-defined as the size of the lattice under consideration grows.

The grayscale in Fig. 2.10 describes the density of states and the finite nature of the lattice manifests itself in the sparse energy levels between bands. For $\alpha \ll 1$, the lowest bands (regions with a high density of states) are linearly proportional to α leading one to draw comparisons to the Landau energy spectra for a single particle in a 2D harmonic oscillator. The Landau energy levels are given by $E_n = (n+1/2)\hbar\omega_c$ where n is an integer and ω_c is the cyclotron frequency. For small α in the spectra shown in Fig. 2.10, the slopes (ratios of band energy to α) are not similarly proportional to the band index, *e. g.*, for the five lowest bands, the slopes are $\sim$ 6, 17, 27, 35 and 43.

2.6 Conclusions

In the tight-binding limit, bosons in a co-rotating lattice can be studied using a Bose-Hubbard Hamiltonian ($\hat{\mathcal{H}}_2$) with modified hopping and onsite energy terms. The new hopping term leads to a $2\pi\alpha$ change in the phase of the many-body wavefunction when a particle goes around a plaquette. For small angular velocities, a simpler Hamilto-

nian $\hat{\mathcal{H}}_1$ with the same symmetry properties is sufficiently accurate. For larger angular velocity, the lowest-band restriction is more severe for $\hat{\mathcal{H}}_1$ than it is for $\hat{\mathcal{H}}_2$. In the continuum limit, $\hat{\mathcal{H}}_2$ can be used to obtain the Harper equation and the single-particle energy spectrum is given by the Hofstadter butterfly. The system is equivalent to spin-polarized Bloch electrons in the presence of a magnetic field (without the long-range Coulombic repulsion between electrons).

Chapter 3

Symmetry

3.1 Introduction

Many classical rotating systems possess continuous rotation symmetry and are rigid. When this is true, the structural description of the system can be encapsulated in the moment of inertia tensor and dynamical quantities of interest such as the angular momentum[1] can be expressed as derivatives of the azimuthal angle. Quantum rotating systems, on the other hand, feature many interesting phenomena, particularly when the system has a significant condensate fraction. The condensate fraction is present and significant when the largest eigenvalue of the one-body density matrix is macroscopic [63] (*i. e.* of $\mathcal{O}(N)$ where N is the total number of particles). Systems with a macroscopic condensate fraction often display superfluid properties. This was first demonstrated in liquid Helium by Kaptiza [40] in 1937. A striking property of superfluids is that of irrotational flow. A superfluid placed in a slowly rotating bucket will not rotate uniformly with the bucket. Rotation is, instead, characterized by the entry of vortices with change in the phase winding of the superfluid order parameter.

The theoretical study of superfluid Helium is complicated in particular owing to the presence of strong interactions between particles. The system that we have undertaken to study — hardcore bosons in a rotating lattice — is further complicated

[1] More precisely, the angular momentum about the principle axes of the moment of inertia tensor is accessible using the derivative of the azimuthal angle.

by a lattice potential that breaks continuous rotational symmetry. Due to this, it is imperative that the language used to describe classical and quantum rotating systems be re-examined carefully in the new context. This chapter uses fundamental symmetry arguments to do this. The second section of this chapter establishes the possibility of seeing vortices in the system just described. The third section discusses the concept of quasi-angular momentum — a quantity that captures the discrete rotational symmetry of the system. The last section shows how the idea of discrete rotational symmetry can be used to demonstrate quantum phase transitions in the system.

Section 3.2 presents unpublished work while parts of Secs. 3.3 and Secs. 3.4 were published in Refs. [10, 12, 62].

3.2 Circulation and vorticity

Superfluidity and vortex properties have been explored in depth for continuously connected systems (see, for instance, Ref. [63]). On the other hand, particle currents in a lattice are described by inter-site tunneling, which establishes phase relationships across the system much like the phase of the superfluid order parameter. We term as 'circulation' the current flow due to inter-site hopping and restrict the use of the moniker 'vortex' for quantized circulation as seen in a superfluid. In this section, the connection of circulation to superfluidity is drawn by trying to answer two questions:

(1) How does the circulation of a superfluid change when a deep lattice is superimposed?

(2) To what extent does a condensate remain condensed in the presence of a lattice and rotation?

The first question is answered by using imaginary-time propagation (as described in Appendix A) to numerically find the ground state wavefunction for different lattice depths. The second can, similarly, be answered numerically by looking at the structure

of the one-body density matrix. Note that the calculations in this section are free of the lowest-band and tight-binding approximations entailed in the Bose-Hubbard approach discussed in the previous chapter because we use the full Hamiltonian (Eq. 3.1).

3.2.1 Vortex formation in a box (in the absence of a lattice)

Consider the toy model of a single particle in a 2×2 lattice bounded by a box. Since there is only one particle, the system has a well-defined phase at all times. Before we examine the effects of the lattice, it is useful to establish vortex properties for a particle in a box rotating about its center. The single-particle Hamiltonian for the system in rotating-frame coordinates, (see also Sec. 2.2) is,

$$\mathcal{H} = -\frac{\hbar^2}{2m}\nabla^2 + V_{box}(x,y) + i\frac{2}{\pi}\frac{\hbar^2}{m}\alpha\left(x\partial_y - y\partial_x\right). \tag{3.1}$$

where, $V_{box}(x,y)$ describes the potential corresponding to a box with very high walls.

In the absence of significant numerical noise, the imaginary-time propagation method preserves the topology of the initial state, *i. e.* if an initial state has a particular phase winding, the final state will correspond to the lowest energy level for that particular phase winding. We use this property to obtain the energy-level diagram corresponding to the lowest energies for phase windings equal to $0, 2\pi, 4\pi$ and 6π (Fig. 3.1). As the rotation increases, there is an exact level crossing (around $\alpha \sim 1.25$) as the energy of the state with a single vortex becomes smaller than the energy of the state without a vortex. This can be corroborated by looking at the ground-state number-density distribution before and after the crossing (Fig. 3.2). The ground state density distribution before the level crossing has the familiar profile for a particle in a box with hard boundary conditions ($\rho(\mathbf{x}) \sim (4/L^2)\cos^2(\pi x/L)\cos^2(\pi y/L)$). The center of the box gets depleted with the entry of a vortex. This corresponds to a vortex core. The annular shape corresponding to the $l = 1$ density distribution is modified by the hard box boundaries in the latter distribution.

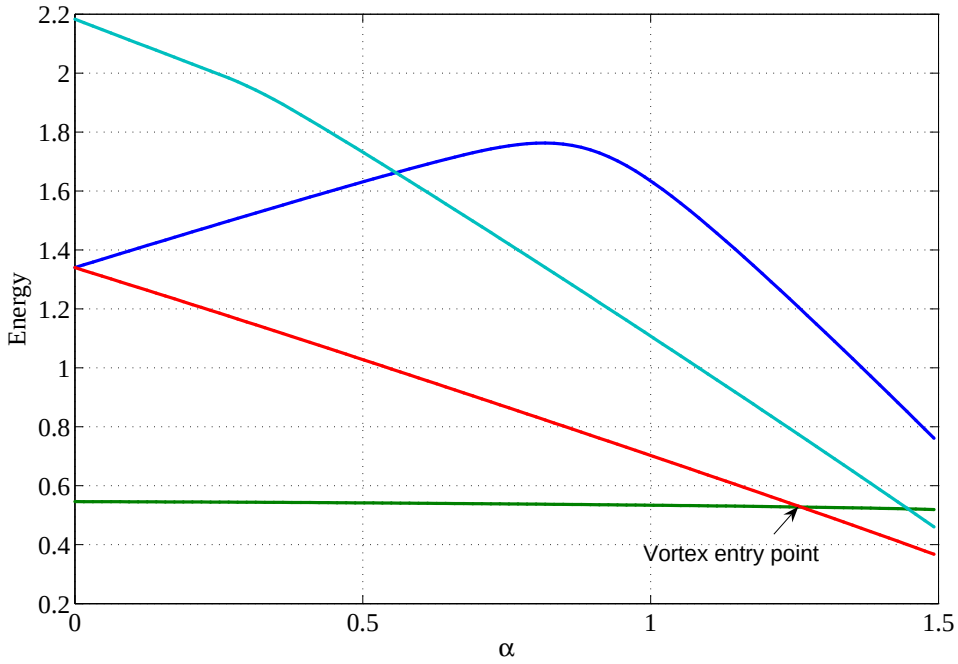

Figure 3.1: Energy spectra (lowest four energies) for a particle in a 2D square box rotating with angular velocity $\Omega = 4\pi\hbar\alpha/mL^2$. The energy is in units of $2\hbar^2\pi^2/mL^2$ where L is the length of the box along any side. The different levels (from low to high at $\alpha = 1$) correspond to phase windings $0, 2\pi, 4\pi$ and 6π.

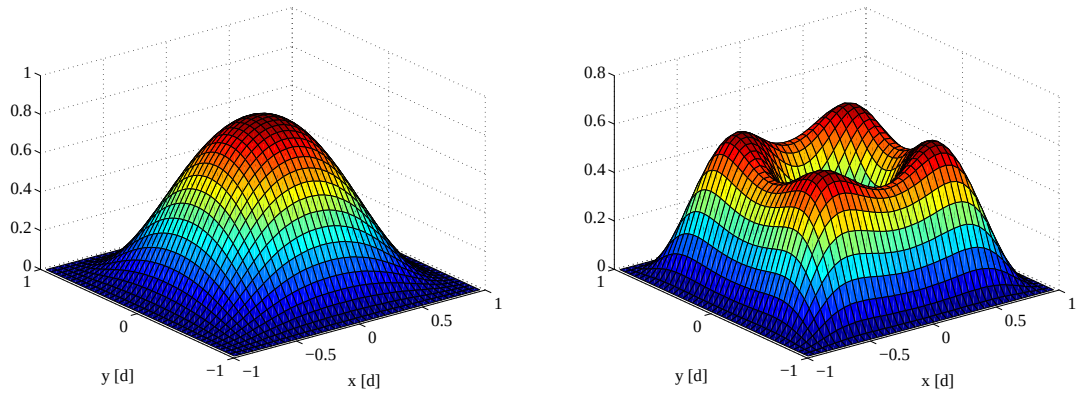

Figure 3.2: (Left) Ground state number density distributions for a single particle in a stationary box ($\alpha = 0$). The distribution is proportional to $\cos^2(\pi x/L)\cos^2(\pi y/L)$ and is accordingly, peaked at the center. (Right) Ground state number density distribution for $\alpha = 1.5$. The center of the box is depleted and marks the vortex core. The additional knobs in the corners are due to the four-fold symmetric hard boundary conditions of the box.

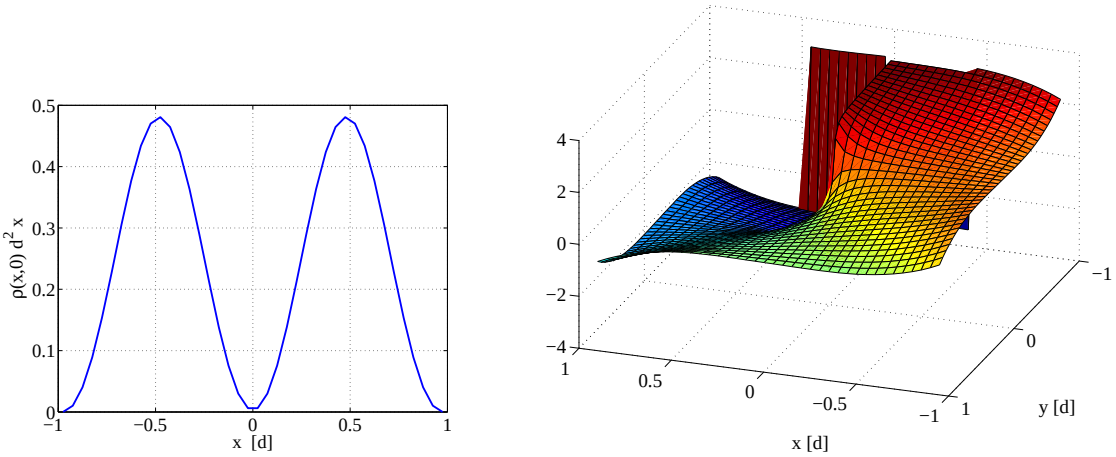

Figure 3.3: (Left) Number density along the y axis of the system for the vortex state in Fig. 3.2. The density at the center drops to zero. (Right) The phase description has a winding of 2π around the axis of rotation.

Taking a slice of the vortex density distribution in Fig. 3.2(right) along the $y = 0$ line confirms that the number density drops to zero in the center (Fig. 3.3 (left)). The last piece of evidence for the presence of a vortex is obtained by looking at the phase description (Fig. 3.3(right)). The phase profile shows a winding of 2π once a vortex has entered the system.

3.2.2 Vortex phase distribution and circulation

In this subsection, we consider the effects of imposing a lattice on the single-particle system just described. The two aspects of the problem that are discussed below are the effect of lattice depth on vortex entry and the change in the phase description when the lattice depth is increased into the tight-binding regime. Also presented is a brief discussion of the superfluid velocity and the quantization of circulation.

Figure 3.4 is a plot of the critical winding number α_{entry} of vortex formation (position of level crossing) as a function of lattice depth. As the lattice depth increases, α_{entry} decreases. Once the system enters the tight binding regime ($V_0 \geq 5E_R$), the

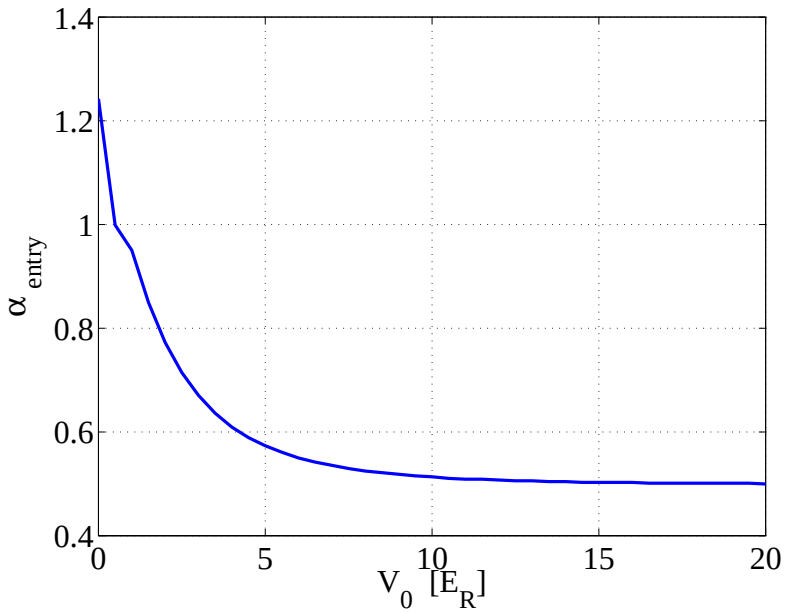

Figure 3.4: Vortex entry point α_{entry} as a function of lattice depth. The lattice depth is expressed in units of the recoil energy $E_R = \hbar^2\pi^2/2md^2 = 2\hbar^2\pi^2/mL^2$. Once well in the tight-binding regime, α_{entry} converges to 0.5

single-band physics dominates and the vortex entry point converges to $\alpha = 0.5$.

Now consider the phase description of the system as the lattice depth changes. When the lattice depth is increased, it becomes more difficult for the particle to tunnel from one site to the next. This is reflected in the phase description of the wavefunction. The particle number density along the site boundaries decreases as the lattice depth increases and the density peaks at the site centers. In order to keep the current constant, the phase gradient between two sites keeps increasing with increasing lattice depth indicating that the particles actually tunnel faster between sites for deeper lattices. Figure 3.5 illustrates how the phase cross-section for a unit vortex changes with lattice depth. The phase gradient is uniform when there is no lattice ($V_0 = 0$) and the phase between two sites converges to a step-like description for increasing lattice depth.

Figure 3.6 shows the superfluid phase around a loop for the case of a single particle in a 2×2 lattice in the tight-binding regime ($V_0 = 10E_R$). There is a 2π winding in

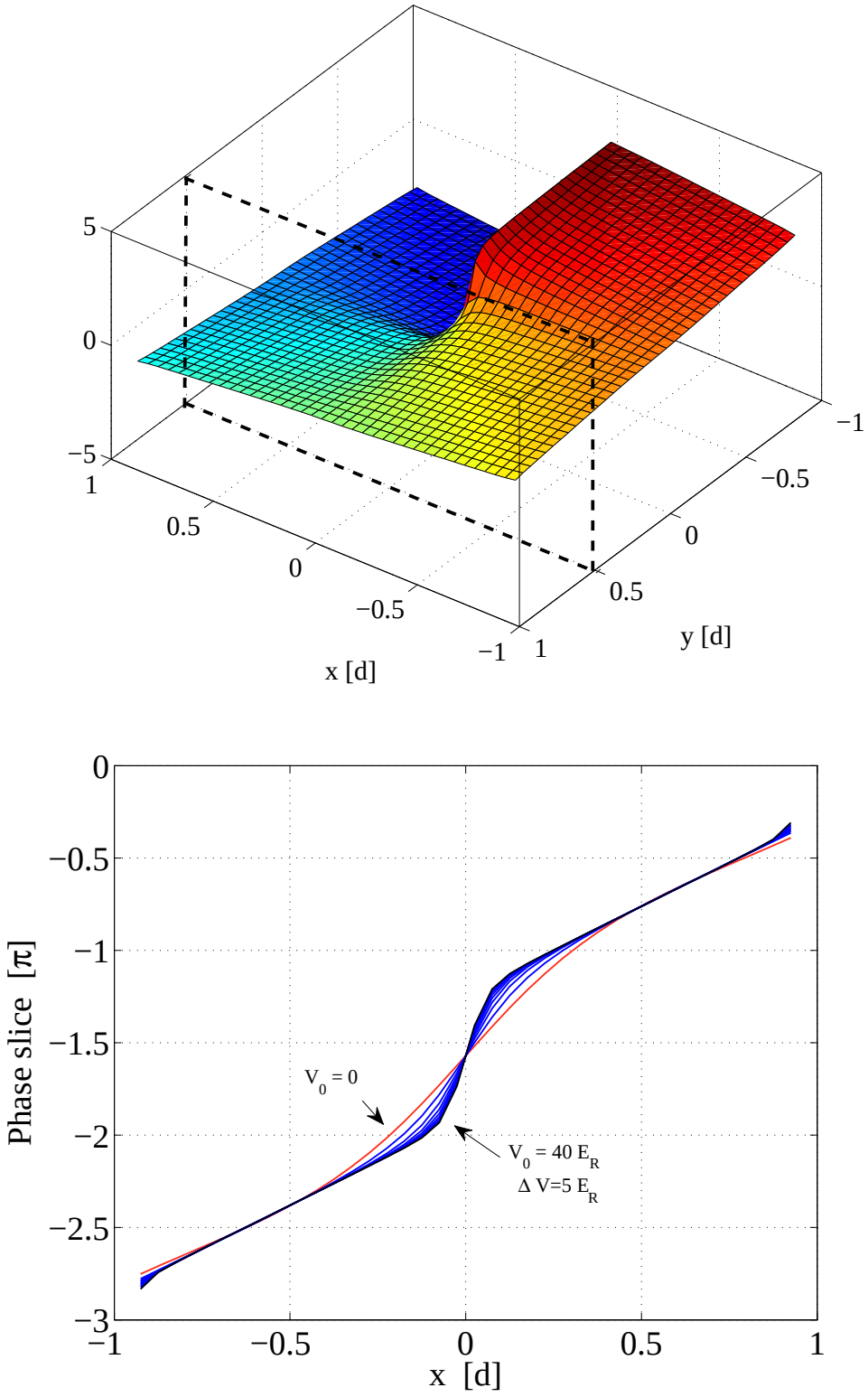

Figure 3.5: (Top) The dashed box marks the slice of the phase description considered. The phase shown here is for $V_0 = 10E_R$; (bottom) The different lines correspond to the phase slice as a function of lattice depth starting from $V_0 = 0$ (red) to $V_0 = 40E_R$ (black) in steps of $5E_R$.

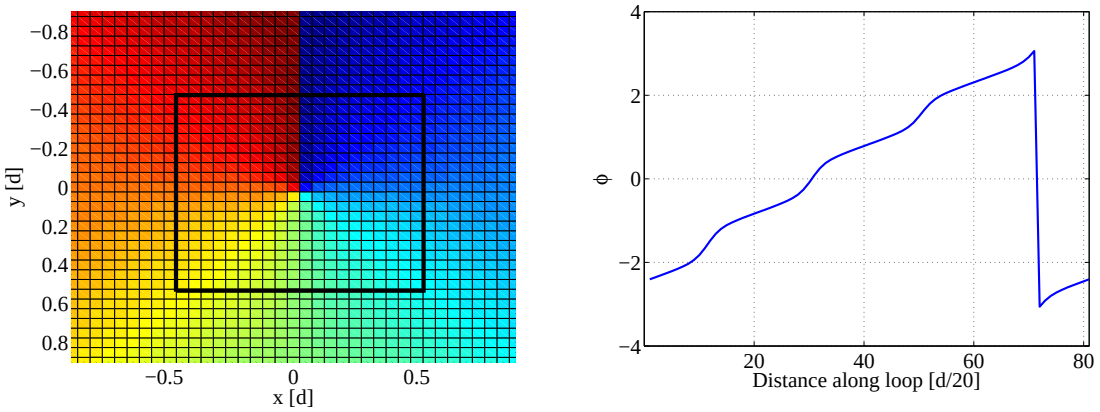

Figure 3.6: (Left) Color plot for a unit vortex in a 2×2 lattice. The dark line marks an arbitrarily chosen loop along which the phase is picked out. (Right) The phase along the loop shown in the left subfigure shows a winding of $2\ \pi$.

the phase description of the system and a loop is chosen by joining the centers of the sites (Fig. 3.6 (left)). The phase gradient along the chosen path is not uniform with a steeper value between site centers (Fig. 3.6 (right)). The superfluid velocity given by the gradient of the phase along the loop accordingly peaks between sites. The circulation is defined by,

$$\Gamma = \int \mathbf{v} \cdot d\mathbf{s} = \int \frac{\partial \phi}{\partial \mathbf{s}} \cdot d\mathbf{s}. \tag{3.2}$$

For a discrete set of points, the integral reduces to,

$$\Gamma = \sum_{loop} \frac{(\phi_{i+1} - \phi_i)}{h} \times h \tag{3.3}$$

where h is the spacing between two grid points. Summing around the phase loop in Fig. 3.6,

$$\Gamma = \ldots \phi_{i+1} - \phi_i + \phi_i - \phi_{i-1} + \ldots = 2\pi \tag{3.4}$$

where the 2π is picked up on going from the red to the blue. Hence, the circulation described is quantized.

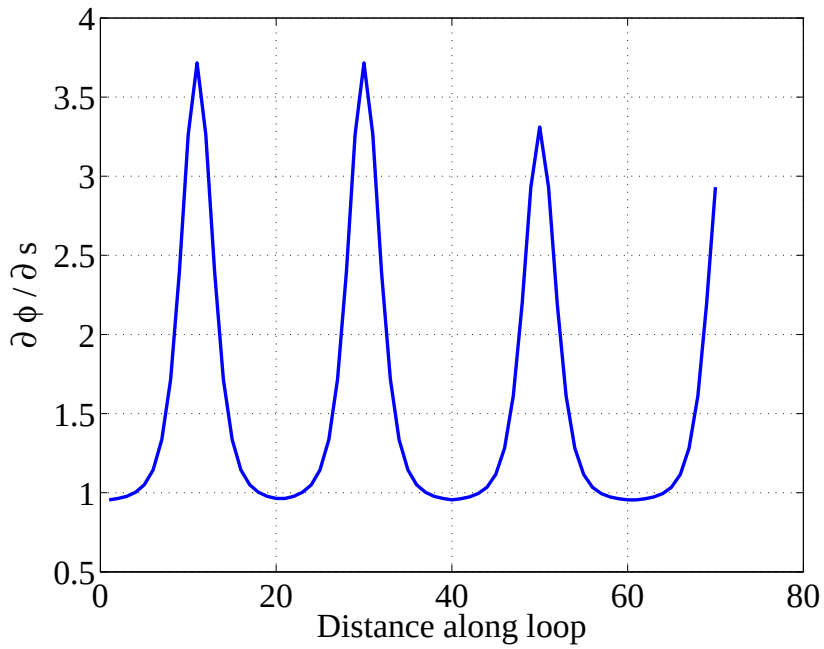

Figure 3.7: The superfluid velocity given by the derivative of the phase along the path for the loop shown in Fig. 3.6. The peaks indicate that the superfluid velocity has maxima as the particle crosses site boundaries. The portion of the loop where the the phase discontinuously jumps by 2π is not shown in order to highlight other features of the velocity.

3.2.3 Condensate fractions

Penrose and Onsager [63] argued that for a Bose-Einstein condensate to be present, the single particle density mode with the largest eigenvalue must be macroscopically occupied. For a lattice system, the elements of the single particle density matrix are obtained by evaluating,

$$\rho_{ji} \equiv \langle \Psi_0 | \, \hat{a}_i^\dagger \hat{a}_j \, | \Psi_0 \rangle \ , \tag{3.5}$$

where Ψ_0 is the ground state of interest and $\hat{a}_i^\dagger$ ($\hat{a}_j$) is the usual site-dependent creation (annihilation) operator. The eigenvectors of ρ are the single-particle modes for the ground state and the corresponding eigenvalues give the occupation of these modes.

We probe the ground-state condensate fraction as a function of rotation for a small many-particle system by first numerically diagonalizing the Hamiltonian to ob-

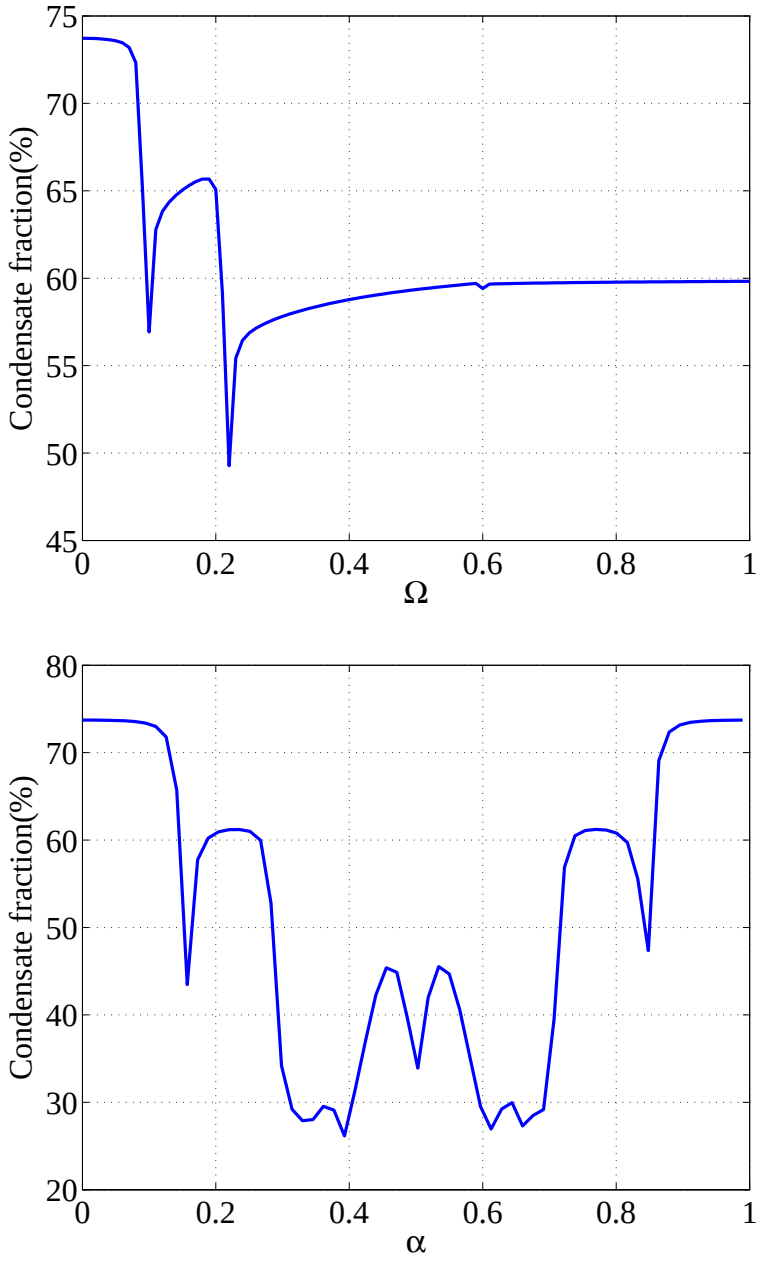

Figure 3.8: Condensate fraction as a function of angular velocity. Both plots show a significant condensate fraction as a fraction of angular velocity for 4 particles in a 4×4 lattice with lattice depth $V_0 = 10E_R$. The plots were generated using $\hat{\mathcal{H}}_1$(top) and $\hat{\mathcal{H}}_2$(bottom) respectively. The sharp dips mark the position where the ground state topology changes.

tain the ground state and then finding the largest eigenvector of the single particle density matrix [65]. As shown in Fig. 3.8, even a rudimentary calculation shows that the condensate fraction is significant (at least for small systems). In general, when the ground state changes, the change in the condensate fraction is discontinuous. In the example illustrated, the dips are continuous because the number of particles is commensurate with the symmetry of the system. Further discussion of this topic is presented in Sec. 3.4.

Note that the plot generated using $\hat{\mathcal{H}}_1$ (Eq. 2.24) has Ω as a measure of angular velocity while the plot obtained using $\hat{\mathcal{H}}_2$ (Eq. 2.37) has α for the same purpose. The relationship between the two is given by Eq. 2.42. We use the different notations to keep distinct the results obtained using $\hat{\mathcal{H}}_1$ and $\hat{\mathcal{H}}_2$. Since both show the similar four-fold rotational symmetry properties, the simpler $\hat{\mathcal{H}}_1$ is used for the rest of this chapter.

3.3 Discrete rotational symmetry and quasiangular momentum

The presence of the lattice breaks the continuous rotational symmetry of the system. The eigenvalues of the angular-momentum operator are therefore no longer good quantum numbers because the rotational symmetry associated with $\hat{L}$ has been replaced with a discrete rotational symmetry. In this section, ideas of discrete translational symmetry and Bloch's theorem are mapped onto the discrete rotational symmetry problem to generate quasi-angular momentum states. We present exact results for the modified Bose-Hubbard model in the context of a single particle one-dimensional ring, and connections are made with the square lattice.

Consider a one-dimensional lattice with periodic boundary conditions,*i. e.*, a ring lattice of N sites. A rotation of $2\pi/N$ leaves the system invariant and hence the rotation operator $\mathrm{R}\,(2\pi/N)$ commutes with the Hamiltonian. This is also true for a square ($N = 4$) because the site dependent parameter K_{ij} in the Hamiltonian (Eq. 2.24) depends on the perpendicular distance of the line connecting two nearest-neighbor sites

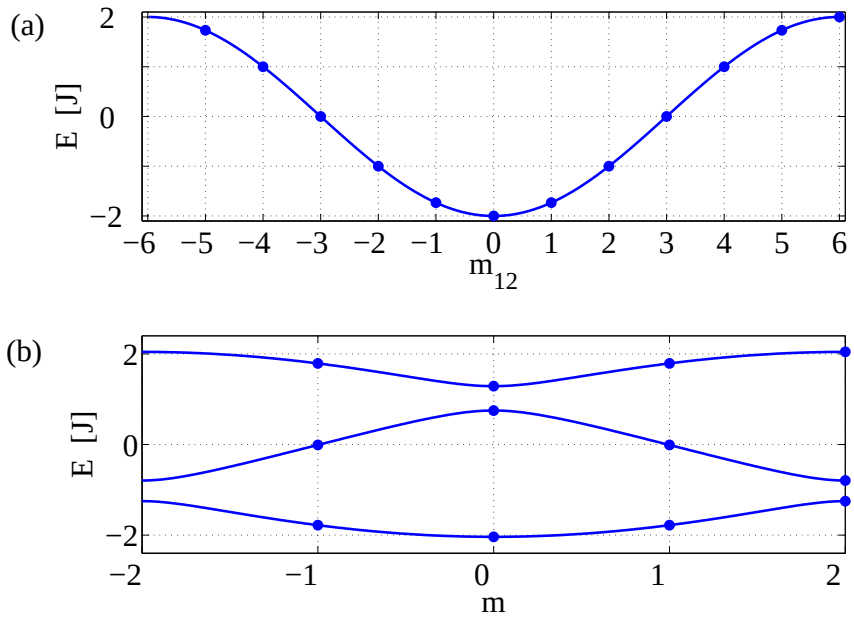

Figure 3.9: (a) Energy-quasi angular momentum dispersion relationship for a 12-site ring. Positive and negative m_{12} values indicate rotation in opposite directions. The velocity of the particles in any state is given by the slope of the dispersion curve at the point. Accordingly, the velocity is maximum at $m = \pm 3$ (b) Energy—quasi-angular momentum dispersion relationship for a 12-site ring with a small four-fold periodic potential. Note the lines joining states are obtained by extrapolating for an infinite system.

from the center of rotation. The energy eigenstates can be labeled using the eigenvalues m of $\mathbf{R}\,(2\pi/N)$:

$$\mathbf{R}\,(2\pi/N)\,|m\rangle = e^{i2\pi m/N}\,|m\rangle : m \in \{0, \ldots, N-1\}, \tag{3.6}$$

where the original eigenstate is retrieved after applying $\mathbf{R}\,(2\pi/N)$ N times.

At this point, it is useful to make a connection with conventional Bloch theory. $\mathbf{R}(\pi/2)$ is analogous to the discrete translation operator $\mathbf{T}(d)$ for a stationary one-dimensional lattice of period d [6],

$$\mathbf{T}(d)\Psi(x_1, \ldots, x_n) = e^{iqd}\Psi(x_1, \ldots, x_n), \tag{3.7}$$

where $\Psi(x_1, \ldots, x_n)$ is an eigenfunction of the translation operator. The eigenvalues of

$\mathbf{T}(d)$ are described by the quasi-momentum q. In a way exactly analagous to that of quasi-momentum Bloch states for a discrete translation operator, we can identify the m-values in Eq. (3.6) as quasi-angular momenta. Note that this discussion so far is completely general and applies to both the single-particle and many-particle cases.

To illustrate the role of the quasi-angular momentum and the connection with the quasi-momentum in systems with discrete translational symmetry, consider one particle in a 12-site static ring. Each of the sites is indexed by the azimuthal coordinate ϕ_i. The energy spectrum takes on the well-known dispersion relation observed for the lowest Bloch band of a particle in a 1D lattice with periodic boundary conditions in the tight-binding regime (Fig. 3.9(a)). Since the system has 12-fold symmetry, the quasi-angular momentum, m, can take on 12 possible values. The slope of the energy plot provides the velocity of the particle. As discussed before (Chapter 2), rotation is introduced by adding a term, $-(\hbar\Omega/i)\partial_\phi$, to the Hamiltonian in order to obtain the ground state in rotating-frame coordinates. As Ω is ramped in a particular direction, the ground-state quasi-angular momentum changes from $m = 0$ to $m = 3$ in steps of 1 (not shown here). The $m = 3$ state corresponds to the maximum slope of the dispersion and the largest particle velocity. A particle in the $m = 4$ state has the same velocity as the $m = 2$ state but with a higher energy. Quasi-angular momenta $m = 7, \ldots, 11$ correspond to $m = -5, \ldots, -1$ and describe circulation in the opposite direction. This is described by the C_{12} point symmetry group.

Consider now a 12-site ring perturbed by a four-fold symmetric periodic potential. The Hamiltonian, $H = H_{12} + V$, is the sum of two terms, the 12-site Hamiltonian H_{12} which has a 12-fold rotation symmetry and a potential V which has a four-fold rotation symmetry. Figure 3.9(b) is the energy dispersion relation as a function of quasi-angular momentum for this system. Since the potential increases the rotational symmetry from $d = 2\pi/12$ to $d = 2\pi/4$, the Brillouin zone is narrowed down to $m = -2, \ldots, 2$. Three energy bands are created in place of one. States on adjacent bands with the same m

value — for example $m_{12} = -2$ and $m_{12} = 2$ — are mixed by the four-fold symmetric potential V, thereby leading to an energy gap at this m value.

An analogous situation occurs when we try to qualitatively understand the properties of a square 4×4 lattice, which has 12 sites on the boundary. We adopt a perturbative approach by breaking the system into two non-interacting 12-site and 4-site rings and considering an interaction between them,*i. e.*, $H = H_{12} + H_4 + V$. The interaction with the four-site ring breaks the 12-fold symmetry of the outer ring, reducing it to a four-fold discrete rotational symmetry.

The above example illustrates that a particle in a square lattice is characterized by a four-fold discrete rotational symmetry. The same symmetry considerations hold for many particles in the system. Hence, the energy eigenstates for many particles in a four-fold symmetric potential are quasi-angular momentum states with $m \in \{-2, 1, 0, 1, 2\}$.

In the following, we show how the rotation of the lattice leads to a change in quasi-angular momentum in the groundstate of the system in the single-particle case (Sec. 5.5.1) and in the many-body case (Sec. 3.4). In addition, we show how these transitions affect other properties of the system, such as its average angular momentum and its vorticity.

3.3.1 Single-particle analysis

This section examines the response of one particle in a square lattice to rotation. The advantage in first considering only one particle is that it allows one to distinguish general characteristics of the system from interaction effects.

Figure 3.10 describes the response of the system as a function of the angular velocity Ω. Figures 3.10(a) and 3.10(b) show that for increasing Ω the ground-state energy E_0 in the rotating frame decreases with a discontinuous derivative as different states become energetically favorable. Note that $\langle L_z \rangle$ takes on non-quantized values which illustrates that the energy eigenstates are not eigenstates of continuous angular

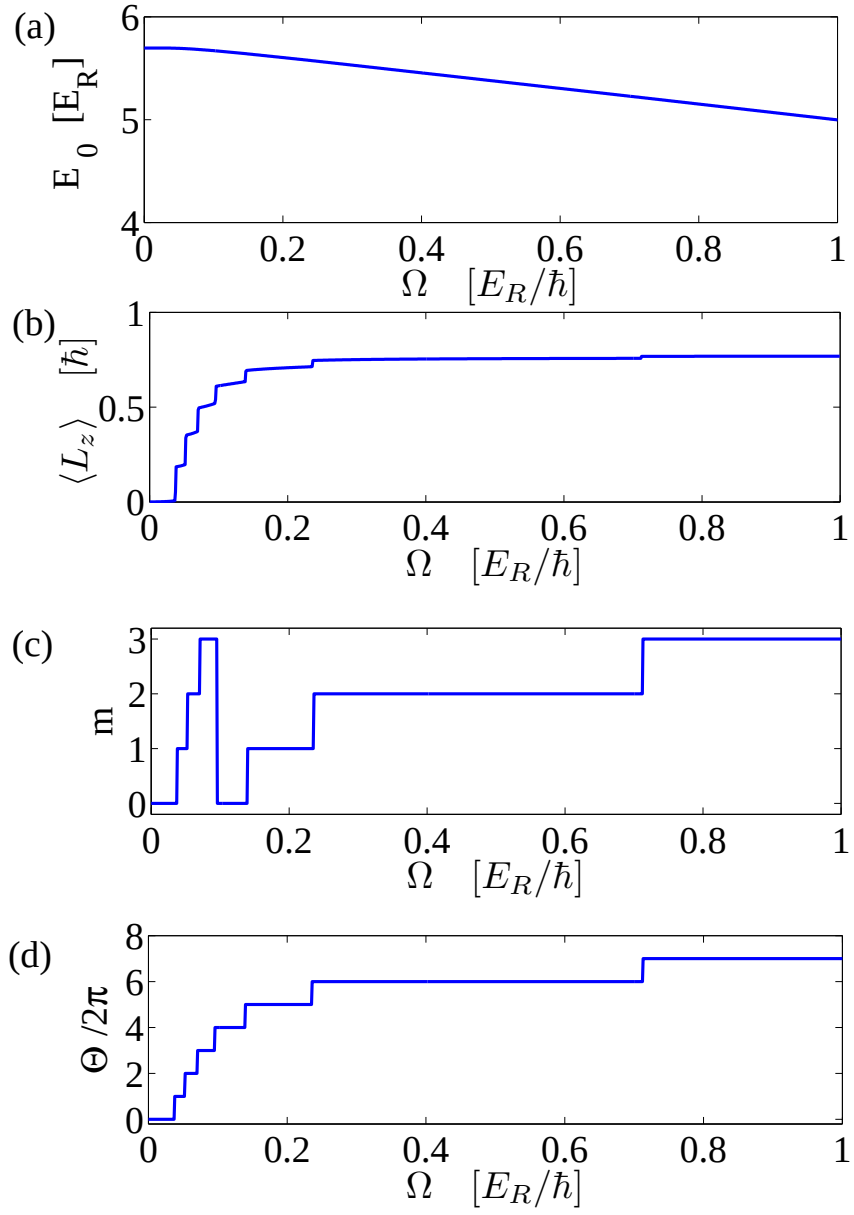

Figure 3.10: One particle in an 8×8 lattice. (a) Ground state energy, E_0 vs. Ω. (b) Average angular momentum $\langle L_z \rangle$ vs. Ω. Note that the expectation value of angular momentum Eq. 2.19) is not quantized. (c) Quasi-angular momentum m vs. Ω. In direct analogy to quasi-momentum values for linear lattices, m repeats itself (Eq. 3.8). (d) The phase winding, $\Theta/2\pi$, vs. Ω. For the 8×8 lattice, the maximum phase winding is $7 \times 2\pi$.

momentum.

The abrupt changes in average angular momentum $\langle L_z \rangle$ are connected to changes in the quasi-angular momentum m of the groundstate as seen in Fig. 3.10(b) and (c). Since the lattice has four-fold rotational symmetry, the values that the quasi-angular momentum can take are $m \in \{0, 1, 2, 3\}$. For additional transitions, m repeats itself in behavior analogous to that of linear quasi-momentum as one crosses the first Brillioun zone.

The changes in quasi-angular momentum are associated with changes in the phase winding of the single-particle wavefunction. The phase winding Θ jumps by 2π each time the quasi-angular momentum of the groundstate changes (Fig. 3.10(d)). The maximum phase winding of 14π for an 8×8 lattice corresponds to a maximum phase difference of $\pi/2$ between any two sites on the lattice boundary, which in turn, corresponds to the condition for the maximum current attainable within the lowest band Bose-Hubbard model. This result can be generalized to a lattice of size $L \times L$. The number of sites on the circumference of the lattice is $4(L-1)$ and for a phase difference of $\pi/2$ between two adjacent perimeter sites, the maximum phase winding around the circumference is $2\pi(L-1)$ within the lowest band. Since the notions of an order parameter and of superfluidity do not apply to single-particle systems, states with non-zero phase winding can not be referred to as quantized vortices. However, as will be shown in the following, these single-particle results extend to many-particle systems in a straightforward manner.

3.4 Quantum phase transitions

This section probes the effect of strongly repulsive interactions in a many-particle system. We first test the symmetry considerations discussed in Section 3.3. The effect of a symmetry-commensurate filling is explored by considering two different systems - (1) four particles in a 4×4 lattice and (2) five particles in a 4×4 lattice. These two

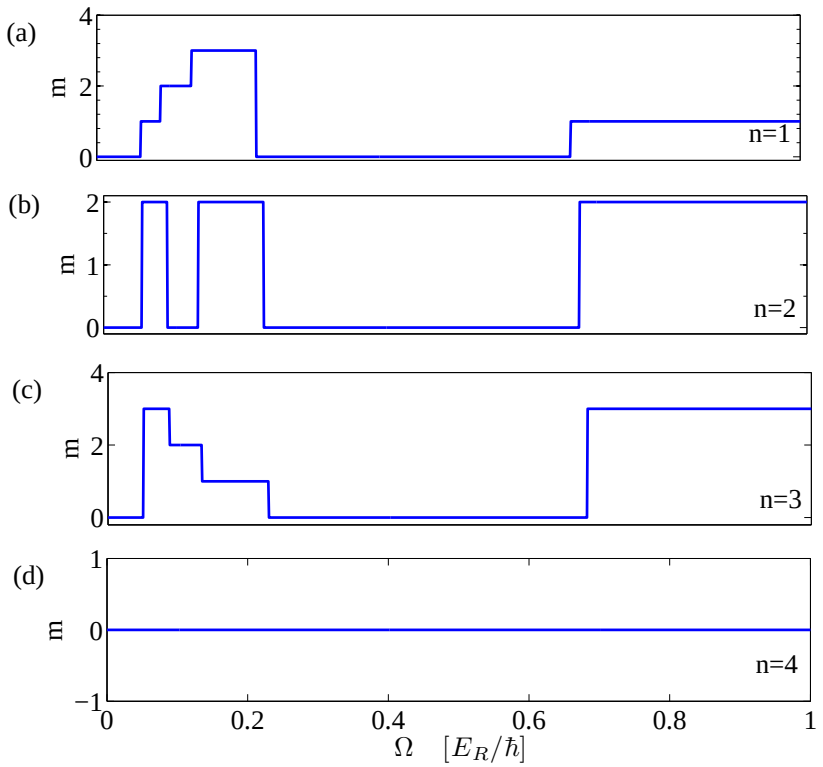

Figure 3.11: Quasi-angular momenta for one through four strongly repulsive bosons in a 6×6 lattice. For multiple particles in the lattice and increasing rotation, the quasi-angular momenta cycles through values given by $m = nl \bmod 4, l = 0, 1, 2, 3$, where n is the number of particles. (a) $n = 1 : m = 0, 1, 2, 3, 0, 1$ (b) $n = 2 : m = 0, 2, 0, 2, 0, 2$ (c) $n = 3 : m = 0, 3, 2, 1, 0, 3$ (d) $n = 4 : m = 0$.

systems correspond to fillings commensurate and incommensurate with the four-fold symmetry of the lattice, respectively.

As discussed in Section 3.3, the four-fold rotational symmetry allows labeling of the many-body states by their quasi-angular momenta. In a static lattice, the ground-state is always characterized by $m = 0$. This value may change when the lattice is rotated at angular velocity Ω, as has been demonstrated in the single-particle case. In contrast to the single-particle case, the many-body groundstate does not necessarily cycle through all possible m-values as Ω is increased. Instead, the values of quasi-angular momenta it can take on depend on the number of particles. As illustrated in Fig. 3.11,

we see that for n particles in the system, the quasi-angular momentum of the ground state cycles through values satisfying the relation

$$m = nl \bmod 4\,, \tag{3.8}$$

where $l \in \{0, 1, 2, 3\}$. The validity of this expression has been verified both numerically for various lattice sizes and particle numbers and analytically within a Jordan-Wigner transformation approach to hard-core bosons in a ring [62]. Hence, only for odd n does the quasi-angular momentum of the groundstate cycle through all values of m. Cases in which the particle number is commensurate with the four-fold symmetry $n = 4, 8, \ldots$ are of particular interest in that these systems always stay in an $m = 0$ state. Note that a simplistic explanation for the validity of Eq. 3.8 is obtained if all particles occupy a condensate mode with quasi-angular momentum $m = 0, 1, \ldots$, yielding a total quasi-angular momentum equal to 0 when $n = 4$.

3.4.1 Symmetry-commensurate filling

When the number of particles is commensurate with the four-fold rotational symmetry, the ground state always has zero quasi-angular momentum. This does not exclude the entry of quantized vortices into the system. To give an example, we analyze the case of four particles in a 4×4 lattice. The largest eigenvalue of the ground state one-body density matrix is found to be $50 - 74\%$ of the total particle number. Since all other eigenvalues are significantly smaller, this number is large enough to refer to the corresponding eigenmode as the condensate wavefunction. The phase winding Θ_{cf} of the condensate wavefunction increases in steps of 2π to a maximum of 6π as the lattice is rotated faster and faster (see Fig. 3.12(a)). This corresponds to a maximum of $L - 1 = 3$ quantized vortices, with $L \times L$ being the size of the lattice. As in the single-particle case, the maximum phase winding that can be observed within a lowest band model is limited by the maximum phase difference of $\pi/2$ between neighboring

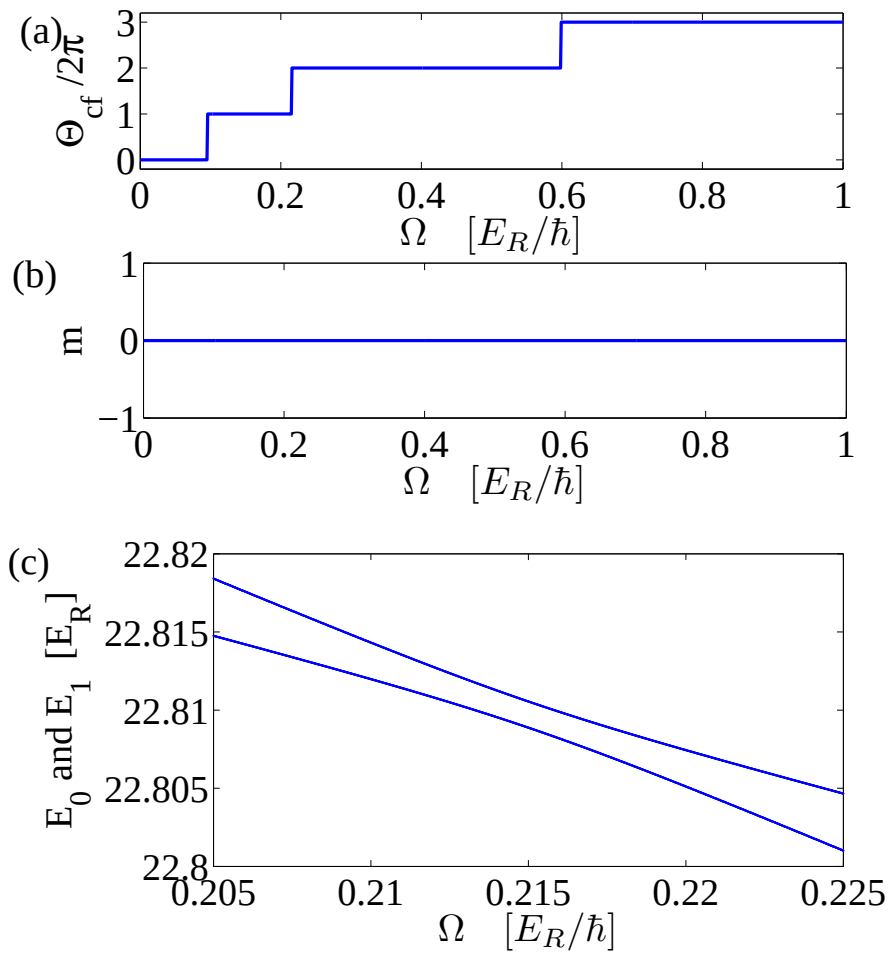

Figure 3.12: Four particles in a 4×4 lattice. (a) Number of vortices, $\Theta_{cf}/2\pi$, vs. Ω. Three vortices enter the 4×4 lattice. (b) Quasi-angular momenta, m vs. Ω. The symmetry of the ground state as indicated by the quasi-momentum $m = 0$ does not change even with three vortices entering the system. (c) Zoom-in of lowest two energy levels around the entry of the second vortex shows an avoided energy level crossing. The mixing of states is possible because the ground states on either side have the same discrete rotational symmetry.

sites.

Each vortex entry is associated with an avoided crossing between ground state and first excited state. This is possible because both states have quasi-angular momentum $m = 0$, allowing them to be coupled near the vortex entry point. This is demonstrated

in Fig. 3.12(c) for the entry of the second vortex.

3.4.2 Symmetry-incommensurate filling

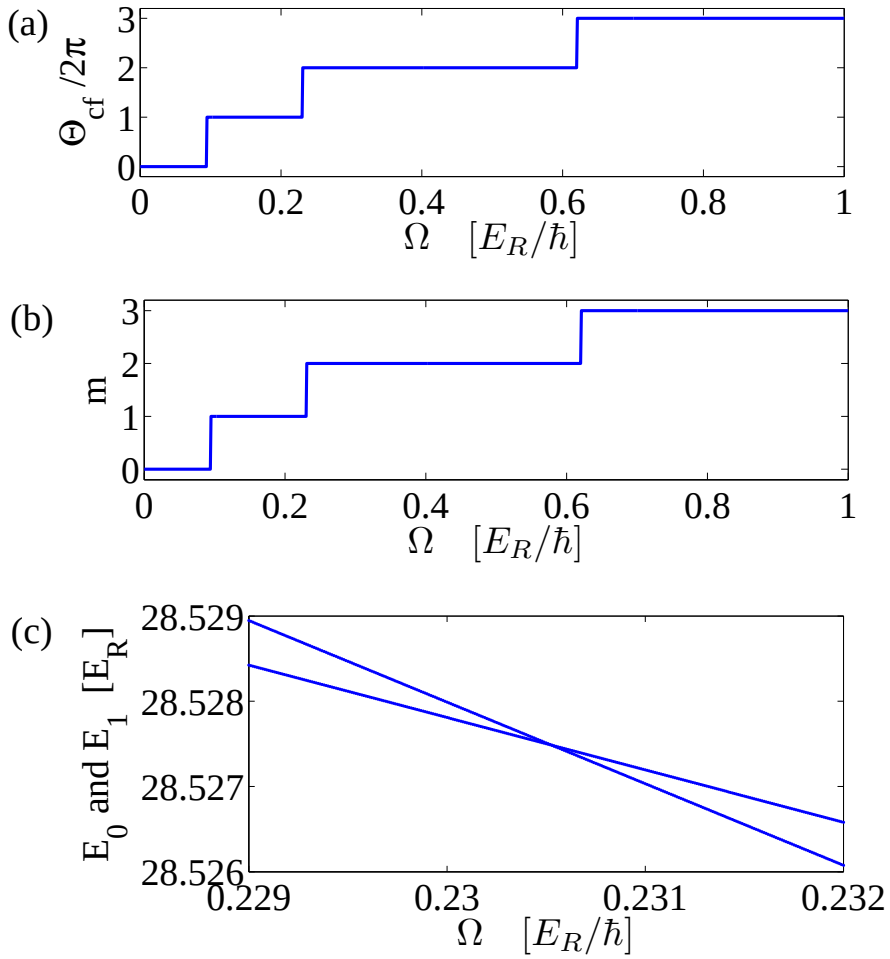

Figure 3.13: Five particles in a 4×4 lattice. (a) Number of vortices $\Theta_{cf}/2\pi$ vs. Ω. As before, a maximum of three vortices enter the system (b) Quasi-angular momenta m vs. Ω. Since the filling is incommensurate with the symmetry, the quasi-angular momenta takes on values $m = 0, 1, 2, 3$ (Eq. 3.8). (c) Zoom-in of lowest two energy levels around the entry of the second vortex shows an energy level crossing as the ground state symmetry changes as a function of a parameter in the Hamiltonian, Ω.

In behavior similar to that for four particles, the eigenmode corresponding to the condensate wavefunction is macroscopically occupied, and $\Theta_{\rm cf}$ for a symmetry-incommensurate number of particles increases in steps of 2π up to a maximum of

$2\pi(L-1)$. Yet, in contrast with a symmetry-commensurate filling, the discrete rotational symmetry of the system changes with each vortex entry. This is demonstrated in Fig. 3.13(a) and (b) where we plot both the phase winding and the quasi-angular momentum as a function of Ω for the case of five particles in a 4×4 lattice. In this setting, the maximum phase winding is given by 6π while the quasi-angular momentum takes the values $m = 0, 1, 2, 3$ in accordance with Eq. (3.8).

For symmetry-incommensurate filling, the symmetry of the many-body wavefunction is different on either side of the jump in the phase winding. Hence, transitions between vortex states cannot occur via the mixing of energy eigenfunctions with the same symmetry. Hence, changes in vorticity are not associated with an avoided crossing between the ground state and the first excited state. Instead, the transition occurs as the energy of an excited state with different quasi-angular momentum and phase winding drops low enough to become the new ground state. The signature of vortex entry is thus a crossing of energy levels with different discrete rotational symmetry and phase winding. Fig. 3.13(c) depicts the level crossing associated with the entrance of a second vortex into a system of five particles in a 4×4 lattice. The level crossings are a non-trivial result for many particles since they correspond to a symmetry change in the ground state as a function of a parameter of the Hamiltonian and are indicative of quantum phase transitions [69].

3.5 Conclusions

A superfluid displays vorticity on being rotated even when loaded in a deep lattice. The phase structure of the superfluid order parameter associated with the vorticity is modified by the lattice. However, the angular momentum of the system is no longer quantized due to the discrete rotational symmetry of the lattice. The discrete rotation operator commutes with the Hamiltonian and hence energy eigenstates can be labelled using quasi-angular momenta. The values of quasi-angular momentum that a system can

take on is determined by the filling. For symmetry-incommensurate fillings, quantum phase transitions are expected when the quasi-angular momentum of the ground state changes as a function of the angular velocity.

Chapter 4

Transport

This section deals with the transport of bosons in optical lattices. Three main topics will be discussed — the derivation of inter-site current and onsite density operators for particles in a lattice, the effect of interactions on current and the derivation of a Kubo formula. In the first section, starting from the continuity equation in real space, we derive the current operator in Wannier space and contrast it with the current operator. We also develop expressions for the discrete position operators. In the second section, the effect of repulsive interaction on current flow in a lattice is illustrated using numerical simulations of interacting bosons on a one-dimensional ring. In the final section, we derive a Kubo formula in the context of an ac perturbation for the lattice system. The formalism developed will be used to study the Hall effect in Chapter 5.

4.1 Transport operators in real space

The second-quantized operators for onsite density and intersite current are formally obtained in this section. The first subsection describes the real-space onsite density operator and shows how it converges to the familiar number density operator for deep lattices. The single-particle Nöther current is obtained in the next subsection using first-quantized notation. The subsequent discussion recasts the expression for the single-particle current using field operators.

4.1.1 The onsite density operator in real space

When representing states using the Fock basis, it is common to evaluate the occupation of a state using the operator $\hat{n}_i \equiv \hat{a}_i^\dagger \hat{a}_i$, where $\hat{a}_i^\dagger$ ($\hat{a}_i$) is the creation (annihilation) operator for a particle in state i. For our lattice discussions, the Fock basis are single-particle Wannier states indexed by i as described in Ch. 2. Though a particular Wannier state is centered at site i, it spills over to neighboring sites (Fig. 2.1). In this subsection, we define a real-space onsite density operator $\hat{\rho}_i$ that returns the particle number within the confines of a lattice site in real space. For an infinite lattice with uniform particle density, the expectation value of the real-space onsite density operator coincides with that of $\hat{n}_i$.

The density field operator is, $\hat{\rho}(\mathbf{r}) = \hat{\Psi}^\dagger(\mathbf{r})\hat{\Psi}(\mathbf{r})$. An on-site density operator can be defined,

$$\hat{N}_i = \int d\mathbf{r}\ \Theta_i(\mathbf{r})\hat{\rho}(\mathbf{r})\,, \tag{4.1}$$

where $\Theta_i(\mathbf{r}) = 1$ if $\mathbf{r}$ is inside site i (*i. e.* $x_i - d/2 < x < x_i + d/2$ and $y_i - d/2 < y < y_i + d/2$) and equal to zero otherwise. Expanding the field operators in terms of annihilation and creation operators,

$$\begin{aligned}
\hat{N}_i &= \int d\mathbf{r}\ \Theta_i(\mathbf{r})\hat{\Psi}^\dagger(\mathbf{r})\hat{\Psi}(\mathbf{r}) \\
&= \int d\mathbf{r}\ \Theta_i(\mathbf{r}) \sum_{j,k} \hat{a}_j^\dagger \hat{a}_k W_R^*(\mathbf{r}-\mathbf{r}_j) W_R(\mathbf{r}-\mathbf{r}_k) \\
&= B_1 \hat{a}_i^\dagger \hat{a}_i + B_2 \sum_{\langle i,j\rangle} \left(\hat{a}_i \hat{a}_j^\dagger e^{i\phi_{ij}} + \hat{a}_i^\dagger \hat{a}_j e^{-i\phi_{ij}} \right)\,,
\end{aligned} \tag{4.2}$$

where, ϕ_{ij} is the phase picked up when a particle hops from site i to site j (Eq. 2.38) and B_1 and B_2 are overlap integrals given by,

$$B_1 = \int d\mathbf{r}\ \Theta_i(\mathbf{r}) W_R^*(\mathbf{r}-\mathbf{r}_i) W_R(\mathbf{r}-\mathbf{r}_i), \text{ and} \tag{4.3}$$

$$B_2 = \int d\mathbf{r}\ \Theta_i(\mathbf{r}) W_R^*(\mathbf{r}-\mathbf{r}_i) W_R(\mathbf{r}-\mathbf{r}_j). \tag{4.4}$$

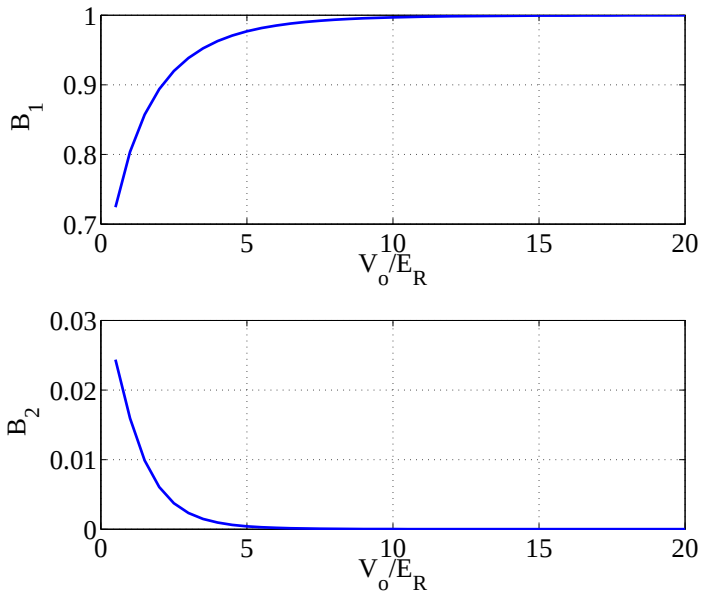

Figure 4.1: Overlap integrals B_1 and B_2 which appear in the onsite density operator $\hat{\rho}_i$ (Eq. 4.2) as a function of lattice depth V_0.

For our calculations we use a lattice depth of $V_0 = 10E_R$ where $B_1 = 0.9969$ and $B_2 = 1.6591 \times 10^{-5}$ respectively. Figure 4.1 shows the dependence of B_1 and B_2 on lattice depth. For very deep lattices, B_1 and B_2 approach one and zero respectively.

4.1.2 Current

The standard expression for the current in stationary-frame coordinates (in first-quantized notation), $\mathbf{J_S}(\mathbf{r}) = \psi^\dagger(\mathbf{r})(-i\hbar\nabla\psi(\mathbf{r})) + (-i\hbar\nabla\psi(\mathbf{r}))^\dagger\psi(\mathbf{r})$, is obtained using the Schrödinger equation of motion and its conjugate (*e. g.*, see Fetter and Walecka [26]). In this subsection, we obtain an expression for the current in rotating-frame coordinates. The expression for the current maps on to the Nöther current where the derivative is replaced by the covariant derivative.

The single particle Schrödinger equation of motion in rotating frame coordinates

for a single particle in a 2D harmonic trap with $\omega = \Omega$ is

$$i\hbar\frac{\partial}{\partial t}\Psi = H\Psi = \frac{1}{2m}\left(\frac{\hbar}{i}\nabla - m\mathbf{A}(\mathbf{x})\right)^2\Psi\,, \tag{4.5}$$

where $\Psi \equiv \Psi(\mathbf{r})$ is the single-particle wavefunction. Multiplying Eq. 4.5 and adding the complex conjugate of the equation we obtain,

$$\frac{\partial}{\partial t}\Psi^*\Psi = \frac{1}{i\hbar}\left[\Psi^* H\Psi - (H\Psi)^*\Psi\right]. \tag{4.6}$$

Using the full form of the Hamiltonian Eq. 4.5, the right hand side becomes,

$$\begin{aligned}\frac{1}{i\hbar}\left[\Psi^* H\Psi - (H\Psi)^*\Psi\right] =& -\frac{\hbar}{2mi}\left[\Psi^*\nabla^2\Psi - \left(\nabla^2\Psi\right)^*\Psi\right] \\ &+ \left[\Psi^*\mathbf{A}\cdot\nabla\Psi + \mathbf{A}\cdot(\nabla\Psi)^*\Psi + \Psi^*(\nabla\cdot\mathbf{A})\Psi\right] \\ =& -\frac{\hbar}{2mi}\nabla\cdot\left(\Psi^*\nabla\Psi - (\nabla\Psi)^*\Psi\right) + \nabla\cdot\left(\Psi^*\mathbf{A}\Psi\right) \\ =& -\frac{1}{2m}\nabla\cdot\left[\Psi^*\left(\frac{\hbar}{i}\nabla - m\mathbf{A}\right)\Psi + \left(\left(\frac{\hbar}{i}\nabla - m\mathbf{A}\right)\Psi\right)^*\Psi\right].\end{aligned} \tag{4.7}$$

We integrate both sides of Eq. 4.6 over an infinitesimal volume V with surface A and apply Stokes' law to the right hand side to obtain a conservation equation,

$$\frac{d}{dt}\int_V \Psi^*(\mathbf{r})\Psi(\mathbf{r})dV = -\int_V dV\nabla\cdot\frac{1}{m}Re\left[\Psi^*\left(\mathbf{p} - m\mathbf{A}\right)\Psi\right] \tag{4.8}$$

$$\frac{d}{dt}\int_V \rho(\mathbf{r}) = \int_A \frac{1}{m}Re\left[\Psi^*\left(\mathbf{p} - m\mathbf{A}\right)\Psi\right]\cdot d\mathbf{a} = -\int_A \mathbf{J}_R(\mathbf{r})\cdot d\mathbf{a}. \tag{4.9}$$

The expression for the current in rotating frame coordinates is obtained by comparing the integrands in the last two expressions,*viz.*

$$\mathbf{J}_R(\mathbf{r}) = \frac{1}{2m}\left[\Psi^*\left(\frac{\hbar}{i}\nabla - m\mathbf{A}\right)\Psi + \left(\left(\frac{\hbar}{i}\nabla - m\mathbf{A}\right)\Psi\right)^*\Psi\right]. \tag{4.10}$$

4.1.3 Second-quantized current operator in rotating frame coordinates

The annihilation operator is defined in terms of the Wannier states (Eqs. 2.3 and 2.30),

$$\hat{\Psi}(\mathbf{r}) = \sum_i \hat{a}_i W_R(\mathbf{r} - \mathbf{r}_i) = \sum_i \hat{a}_i \exp\left[i\frac{m}{\hbar}\int_{\mathbf{r}_i}^{\mathbf{r}}\mathbf{A}(\mathbf{r}')\cdot d\mathbf{r}'\right] W_S(\mathbf{r} - \mathbf{r}_i). \tag{4.11}$$

The second quantized current density operator is obtained by replacing the single particle wavefunction by the field operator in Eq. 4.12,

$$\begin{aligned}\hat{J}_R(\mathbf{r}) &= \frac{1}{2m}\left[\hat{\Psi}^\dagger(\mathbf{r})\left(\frac{\hbar}{i}\nabla - m\mathbf{A}(\mathbf{r})\right)\hat{\Psi}(\mathbf{r}) + \hat{\Psi}(\mathbf{r})\left(-\frac{\hbar}{i}\nabla - m\mathbf{A}(\mathbf{r})\right)\hat{\Psi}^\dagger(\mathbf{r})\right] \\ &= \frac{\hbar}{2mi}\sum_{i,j}\hat{a}_i^\dagger\hat{a}_j e^{-i\phi_{ij}}\left[W_S(\mathbf{r}-\mathbf{r}_i)\nabla W_S(\mathbf{r}-\mathbf{r}_j) - W_S(\mathbf{r}-\mathbf{r}_j)\nabla W_S(\mathbf{r}-\mathbf{r}_i)\right] .\end{aligned} \tag{4.12}$$

In the expression above, note that the terms with $i = j$ cancel. Further, in the tight-binding regime, only overlaps between Wannier orbitals in nearest-neighboring sites are significant. The even parity of Wannier functions about their site centers provides the relationship: $W_S(\mathbf{r}-\mathbf{r}_j)\nabla W_S(\mathbf{r}-\mathbf{r}_i) = -W_S(\mathbf{r}-\mathbf{r}_i)\nabla W_S(\mathbf{r}-\mathbf{r}_j)$. The last two ideas can be used to convert the sum over sites i, j into a sum over links $\langle i, j\rangle$ and the expression for the current rewritten as a sum over currents across nearest-neighbor sites is,

$$\hat{J}_R(\mathbf{r}) = -\frac{\hbar}{mi}\sum_{\langle i,j\rangle}\left[\hat{a}_i\hat{a}_j^\dagger e^{i\phi_{ij}} - \hat{a}_i^\dagger\hat{a}_j e^{-i\phi_{ij}}\right]\left(W_S(\mathbf{r}-\mathbf{r}_i)\nabla W_S(\mathbf{r}-\mathbf{r}_j)\right) . \tag{4.13}$$

At this point, the current operator is still a function of the position $\mathbf{r}$. An inter-site current operator $\hat{J}_{R,ij}$ can be defined by integrating the component of $\hat{J}_R(\mathbf{r})$ normal to the line separating the two sites,

$$\hat{J}_{R,ij} = -\frac{\hbar}{mi}\left[\hat{a}_i\hat{a}_j^\dagger e^{i\phi_{ij}} - \hat{a}_i^\dagger\hat{a}_j e^{-i\phi_{ij}}\right]\int_s ds\left(W_S(\mathbf{r}-\mathbf{r}_i)\nabla W_S(\mathbf{r}-\mathbf{r}_j)\right)_\perp . \tag{4.14}$$

For example, if the two sites are nearest neighbors along the x-direction ($x_j = x_i + d, y_i = y_j$), the integral is,

$$\begin{aligned}\int_{y_i-d/2}^{y_i+d/2} dy\left(W_S(\mathbf{r}-\mathbf{r}_i)\partial_x W_S(\mathbf{r}-\mathbf{r}_j)\right) = W_S\left(x_i + \frac{d}{2} - x_i\right)\partial_x W_S\left(x_i + \frac{d}{2} - x_i - d\right) \\ \times \int_{y_i-d/2}^{y_i+d/2} dy W_S^2\left(y - y_i\right) .\end{aligned} \tag{4.15}$$

Putting it together,

$$\hat{J}_{R,ij} \approx -\frac{\hbar\gamma}{mi}\left[\hat{a}_i\hat{a}_j^\dagger e^{i\phi_{ij}} - \hat{a}_i^\dagger\hat{a}_j e^{-i\phi_{ij}}\right] , \tag{4.16}$$

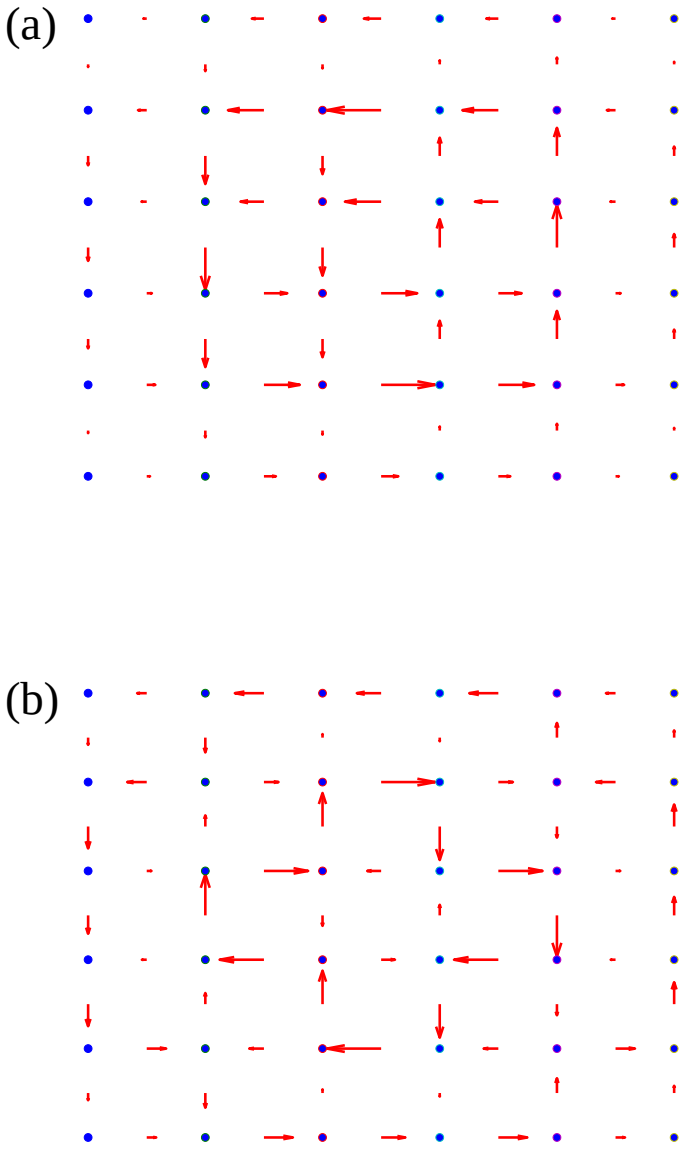

Figure 4.2: Intersite current flow for a single particle in 6×6 lattice for (a) winding number $\alpha = 0.1$ and (b) $\alpha = 0.3$. The length of the each arrow is proportional to the expectation value of the inter-site current (Eq. 4.16) across that link.

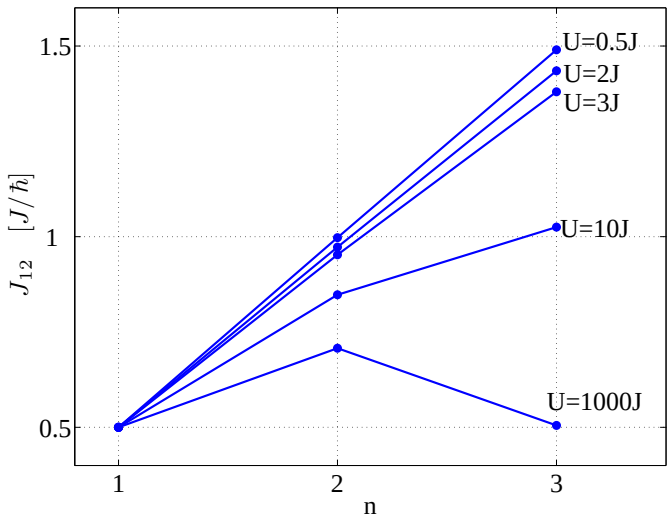

Figure 4.3: Current J_{12} between adjacent sites of a 2×2 site cell lattice as a function of total number of particles n for different values of the ratio between repulsive interaction and hopping U/J at large rotation ($\hbar\Omega \sim 0.6E_R \gg J$). For weak interaction, $U = 0.5J$, the particles can freely cross each other and the current is proportional to the number of particles. As the interaction increases, the current per particle drops as a function of filling. For $U = 1000J$, the current for three particles is the same as that for one particle, indicating a particle-hole symmetry. The current was evaluated using a four-state Fock basis on each site, which allowed three particles per site.

where, the constant $\gamma = W_S^2\left(\frac{d}{2}\right)\int_{-d/2}^{d/2} dy' W_S^2(y')$. Note there are additional contributions to the current from adjoining sites. For a square lattice, these two additional contributions will be much smaller and of order $\gamma_2 = W_S^2\left(\frac{d}{2}\right)\int_{d/2}^{3d/2} dy' W_S^2(y')$ each. For a lattice depth of $V_0 = 10E_R$, $\gamma \approx 0.094d^2$ and $\gamma_2 \approx 7.5 \times 10^{-5} d^2$. The algebraic sum of currents entering or leaving a site is equal to zero. However, as can be seen in Fig. 4.2, deciphering current flow patterns is not straightforward.

4.2 The effect of interactions on lattice current

Repulsive interactions between bosons inhibit current flow by making it difficult for particles to cross each other. To demonstrate this we consider currents in a 2×2 site lattice using a four-state Fock basis on each site. Figure 4.3 is a plot of the current

in the rotating frame J_{12} between two neighboring sites as a function of filling n for different interaction strengths U (see Eq. 2.37 for full Hamiltonian) at fixed angular velocity ($\hbar\Omega \sim 0.6E_R \gg J$). The angular velocity is chosen such that one vortex has entered the system. For weak interactions ($U = 0.5J$), the current is proportional to the number of particles as they can flow independently of each other. However, the current per particle drops with increasing interaction and filling. At large interaction ($U = 1000J$), the current for one hole (three particles) is the same as for one particle in the system. This particle-hole symmetry is characteristic of the regime where bosons are impenetrable, *i. e.*, of the regime where the two-state approximation applies [73]. In fact, currents calculated for $U \geq 100J$ using the two-state approximation, where there can be 0 or 1 particle per site, coincide with those obtained with a larger Fock space. The main results of this thesis are obtained assuming the atoms to be impenetrable and hence are expected to be quantitatively accurate in the regime $U \geq 100J$ for fillings ≤ 1.

4.3 Kubo formula

A Kubo formula captures the linear response of the system to a perturbation. In this section, we present the Kubo formalism used to study the Hall effect in the next chapter. The Hall effect describes the longitudinal and transverse transport responses of a two-dimensional electron gas in the presence of a magnetic field to an applied electric potential gradient. The mapping between magnetic flux density for the 2D electron problem and angular velocity for a rotating gas is valid when the latter problem is formulated in rotating frame coordinates. Accordingly the perturbation is introduced in the rotating frame.

Consider the lattice system sketched in Fig. 4.4. The optical lattice is co-rotating with the condensate about the z-axis with angular velocity Ω. The harmonic trap (not shown) frequency is adjusted to $\omega = \Omega$ such that the centrifugal force is cancelled.

The perturbation is introduced by tilting the lattice along the x-axis in the rotating frame and is modulated by a frequency ν to induce sloshing. An AC perturbation is switched on at time $\tau = 0$. A common mathematical trick to simultaneously extract both quadrature components of the linear response of the system is to use a complex perturbation. In this case, the sine and cosine (phase-shifted) components of $\hat{V}$ will go through and recombine to give a $\exp(i\nu\tau)$ factor in the final result. Accordingly, the perturbation is written as,

$$\hat{V}(\tau) = A\Theta(\tau)e^{i\nu\tau}\hat{X} = A\Theta(\tau)e^{i\nu\tau}\sum_j x_j\hat{n}_j\,, \tag{4.17}$$

where A is the strength of the perturbation, x_i is the x-coordinate of site i, and $\Theta(\tau)$ is the Heaviside function. The effect of the implicit infinite boundaries is mitigated by making the time scales associated with the sloshing small compared to that associated with hopping from one site to the next,*i. e.*, $\hbar\nu >> J$. A brief sketch of the derivation for the change in the expectation value of an observable $\hat{Y}$ due to the perturbation follows (see Refs. [18, 48] for detailed discussions). The density matrix in the interaction picture $\hat{\rho}^I(\tau)$ can be broken into a time-independent part $\hat{\rho}_o$and the change $\Delta\hat{\rho}^I(\tau)$ due to the perturbation,

$$\hat{\rho}^I(\tau) = \hat{\rho}_0 + \Delta\hat{\rho}^I(\tau)\,, \tag{4.18}$$

where the superscript I marks quantities in the interaction picture. The time-independent part $\hat{\rho}_0$ corresponds to the density matrix for the unperturbed system. Retaining the first-order terms in the Liouville equation of motion for the density matrix provides an expression for the second term in Eq. 4.18,

$$\Delta\hat{\rho}^I(\tau) = -\frac{i}{\hbar}\int_{-\infty}^{\tau} e^{-\eta(\tau-\tau')}\left[\hat{V}^I(\tau'),\hat{\rho}_0\right]d\tau'\,. \tag{4.19}$$

Here η is used to fix the boundary conditions and we take the limit $\eta \to 0+$ at the end of the calculation. The expectation value of $\hat{Y}$ is,

$$\langle\hat{Y}(\tau)\rangle = Tr\left\{\hat{Y}(\tau)\hat{\rho}(\tau)\right\} = Tr\left\{\hat{Y}^I(\tau)\hat{\rho}^I(\tau)\right\}\,. \tag{4.20}$$

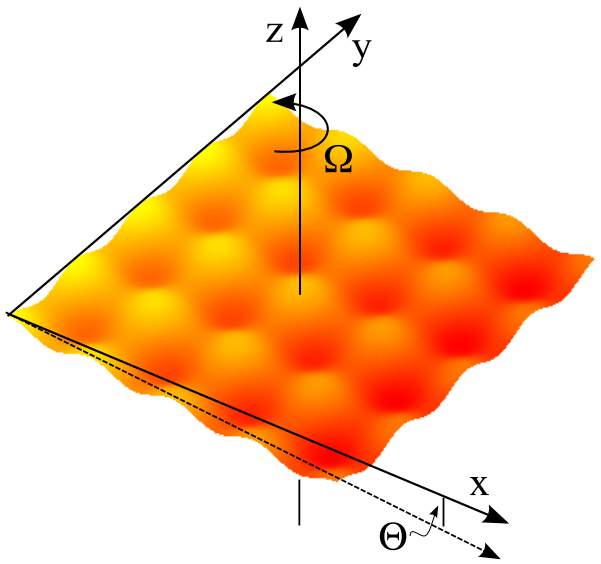

Figure 4.4: Scheme for creating a perturbative linear gradient potential in the system. The lattice potential is tilted by an angle Θ along the x-direction. The 2D trapping potential is cancelled out by the centrifugal force at $\omega = \Omega$ and has not been shown. In order to reduce the effect of the implicit infinite boundary potential walls in our calculations, we consider an AC perturbation where the tilt angle is modulated by a frequency $\nu = d\Theta/d\tau$.

where $\hat{Y}^I$ is the operator in the interaction picture. The expectation value of the response to the perturbation is,

$$\langle \Delta\hat{Y}(\tau)\rangle = Tr\left\{\hat{Y}^I(\tau)\Delta\hat{\rho}^I(\tau)\right\}. \tag{4.21}$$

At low temperatures, the only contribution to the trace comes from the ground state, *i. e.*, $\hat{\rho}_0 \approx |\psi_0\rangle\langle\psi_0|$. The final expression for the expectation value of the response is obtained using this approximation and substituting for $\Delta\hat{\rho}^I(\tau)$ [Eq. (4.19)],

$$\begin{aligned}\langle \Delta\hat{Y}(\tau)\rangle = \frac{Ae^{i\nu\tau}}{\hbar}\sum_{n>0} \\ \Big[\langle\psi_0|\hat{Y}|\psi_n\rangle\langle\psi_n|\hat{X}|\psi_0\rangle\,\frac{e^{-i(\omega_n-\omega_o+\nu)\tau-\eta\tau}-1}{(\omega_n-\omega_o+\nu)-i\eta} \\ +\langle\psi_0|\hat{X}|\psi_n\rangle\langle\psi_n|\hat{Y}|\psi_0\rangle\,\frac{e^{i(\omega_n-\omega_o-\nu)\tau-\eta\tau}-1}{(\omega_n-\omega_o-\nu)-i\eta}\Big],\end{aligned} \tag{4.22}$$

where $|\psi_n\rangle$ are energy eigenstates. The frequency-dependent exponents in the numerators arise from the Fourier transform of the Heaviside function. Note that $n > 0$, because $\langle\psi_0 \left|\hat{X}\right| \psi_0\rangle = 0$ since the unperturbed ground state is symmetric about the y-axis while $\hat{X}$ is not. For the purposes of the discussions in this thesis, the linear response (Eq. 4.22) is evaluated long after the perturbation is switched on ($\tau \to \infty$), damping effects are ignored ($\eta \to 0+$), and the prefactor $\exp(i\nu\tau)$ is excluded from results shown.

Chapter 5

Hall effect

5.1 Introduction

Rotating Bose-Einstein condensates (BECs) have been a subject of great theoretical and experimental interest over the last few years. Starting from the quantum engineering of a single vortex [85], rotating condensates have been used to understand exotic phenomena such as the formation of Abrikosov vortex lattices [47, 32] and the BCS-BEC crossover [89]. Parallels have been drawn between atoms in a rotating condensate and electrons in the presence of a magnetic field; in particular, the fractional quantum Hall effect (FQHE) has been predicted for a two-dimensional (2D) condensate rotating at a frequency matching that of the confining harmonic trap [84, 19, 83, 61, 27, 13]. This strongly correlated FQHE regime has, however, been difficult to achieve experimentally in cold quantum gases due to two problems. First, it is difficult to confine condensates at rotation speeds matching the trapping frequency. Second, vortex shears destroy condensates at high rotation. A potential solution to both problems is the use of a 2D lattice: Introducing a co-rotating optical lattice in the tight-binding regime, in which particles on a lattice site can only tunnel to adjacent sites, provides strong confinement and enhances interactions to enable entry into the strongly-correlated regime. A similar system outside the tight-binding regime has recently been demonstrated experimentally [79]. In this chapter, we study the possibility of realizing Quantum Hall-like effects for bosons in a rotating optical lattice. Connections have previously been made to the FQHE for

cold atoms in a lattice in the presence of an effective magnetic field [39, 60] or induced tunneling loops [73].

The rest of this chapter is divided into four sections. The first provides a short introduction to the Hall effect in a 2D electron gas. The second discusses the proof by Niu *et al.* [59] showing the integer Hall effect to be a topological effect. This proof holds even with an underlying lattice potential and hence is an important first step in drawing our connections with the Quantum Hall effect for bosons in a rotating optical lattice. In the third section, we add a perturbative lattice potential to the cold-atom analog of the electronic Quantum-Hall setup and show that the Quantum Hall effect is still present, even though the Hall resistivity is spatially modulated. In the last and main section of this chapter, we use the Kubo formalism introduced in Sec. 4.3 to describe the system's current and density responses to a perturbative potential gradient. Using a high-frequency perturbation to overcome finite-size effects, we observe FQHE features in a single-particle system. In particular, the system demonstrates plateaus in the transverse resistivity concurrent with dips in the diagonal resistivity for fractional values of α. At these same values, in concordance with Jaksch *et al.* [39], the site number density is modulated with a periodicity $1/\alpha$. Numerical results are also presented with several particles. In direct analogy with the classical Hall effect, a pileup of particles due to the Coriolis force is seen along the transverse direction.

5.2 Hall effect in a 2D electron gas

In 1879, Edwin Hall conducted an experiment where he passed a current through a thin gold leaf and measured the voltage both along and perpendicular to the current path [33]. In the presence of a perpendicular magnetic field, he found that the transverse voltage was proportional to the strength of the magnetic field. This behavior is now known as the Hall effect. The mechanism responsible for the Hall effect can be understood as follows.

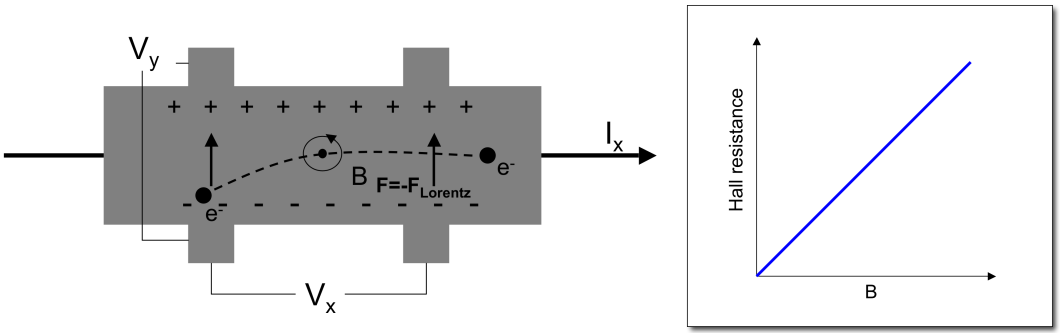

Figure 5.1: (Left) Schematic for Hall effect. (Right) The classical Hall resistance R_H as a function of the magnetic field strength B in arbitrary units. The slope of the line is $1/en_0$ where e is the charge carried by an electron and n_0 is the electron density.

Consider a classical electron with charge $-e$ moving along the negative x-axis with velocity $\mathbf{v}$ in the presence of a magnetic field $\mathbf{B}_\perp$ (Fig. 5.1(left)). The electron experiences a Lorentz force

$$\mathbf{F}_{\text{Lorentz}} = -e\mathbf{v} \times \mathbf{B}_\perp \,. \tag{5.1}$$

If the sample is finite-sized, there is a charge buildup along the upper and lower edges in Fig. 5.1(left) leading to an electric potential difference V_y. Eventually, the potential is large enough to stop the transverse motion, *i. e.*

$$\frac{V_y}{d} \;=\; v_x B_\perp \,, \tag{5.2}$$

where d is the thickness of the two-dimensional sample along the y-axis and v_x is the x-component of the electron velocity. If the electron area density is n_0, the current along the y-axis is $I_x = en_0 dv_x$. The Hall resistance as defined by

$$R_H \;=\; \frac{V_y}{I_x} = \frac{B_\perp}{en_0} \,. \tag{5.3}$$

Hence for a normal conductor, the Hall resistance is directly proportional to the magnetic field (Fig. 5.1(right)).

However a century later, in 1980, von Klitzing found that this simple behavior does not hold for a truly effective 2D electron gas (Si MOSFET) [42]. The resistance

still increases with the magnetic field but only in discrete steps of h/me^2 where m was an integer. The precision of the spacing between plateaus led to a new standard for the quantum of resistance $R_K = h/e^2 = 25.812807449(86)\,k\Omega$ and Klaus von Klitizing was awarded the Nobel Prize in 1985 for discovering what is now known as the integer quantum Hall effect (IQHE). For a system such as that studied by von Klitzing, the number of electrons that can fit into each Landau level is fixed by the magnetic field and the area electron density. Now, consider the case when the LLL is completely full. On lowering the magnetic field, at least one of the electrons has to jump across a finite energy gap to the next Landau level. Surface defects or impurities act as reservoirs for this change in occupancy keeping the Hall resistance steady. In very pure samples such as those studied by Tsui *et al.* [78], plateaus appear, in the Hall resistance, even at fractional values of h/e^2 as shown in Fig. 5.2. This is called the fractional quantum Hall effect (FQHE).

The FQHE can be explained in terms of composite particles created by bringing together electrons and magnetic flux quanta. Instead of the integer m, one uses a filling factor

$$\nu \;=\; \frac{\text{No. of particles}}{\text{No. of flux quanta}}\,. \tag{5.4}$$

For example, in the $\nu = 1/2$ state, each particle is coupled with two flux quanta. If an odd number of flux quanta is coupled to the particle, the composite particle is effectively bosonic and can Bose-condense to generate the quantum Hall state. This explains the drop of the diagonal resistivity to zero at fractional values of ν. The full discussion of the theory behind the FQHE is rich and well beyond the scope of this brief introduction. For a more indepth discussion, the reader is referred to the text by Ezawa [25] and references therein.

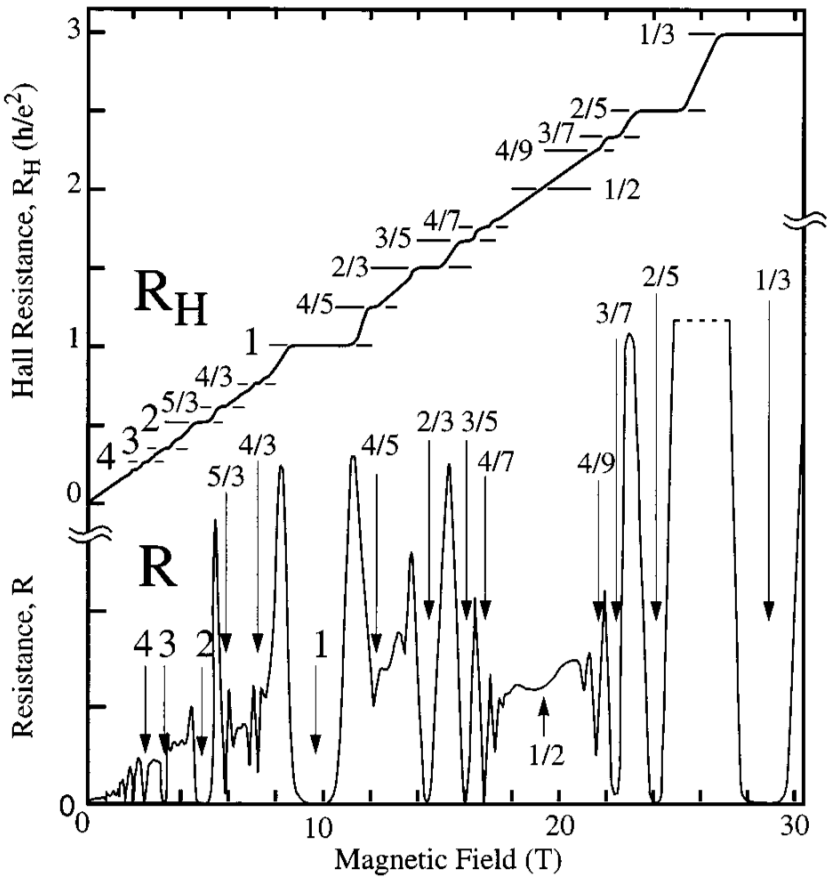

Figure 5.2: FQHE as seen in an ultrahigh-mobility modulation-doped GaAs/AlGaAs 2D electron system. Most of the steps correspond to fractions of the filling factor corresponding to $\nu = p/(2p \pm 1)$ where p is a positive integer. This plot was obtained from a review paper [74] published by Störmer shortly he won the 1998 Nobel prize for discovering the fractional quantum Hall effect along with Tsui and Gossard.

5.3 Hall conductance as a topological invariant

The discussion in this section is based on a beautiful proof by Niu *et al.*[59] for the integer Quantum Hall effect and provides many intermediate steps not shown in the original publication. This discussion is crucial to our study, because it establishes that the features of the integer Quantum Hall effect can be expected even in the presence of an external potential such as the lattice potential used in this thesis.

5.3.1 Hamiltonian for a 2D electron gas

Consider the typical Hall setup — an interacting two-dimensional electron gas in the presence of a magnetic field. The many-particle Hamiltonian for the unperturbed system is

$$\begin{aligned} H &= \sum_{i=1}^{N}\left[\frac{1}{2m}\left(-i\hbar\frac{\partial}{\partial x_i}\right)^2+\frac{1}{2m}\left(-i\hbar\frac{\partial}{\partial y_i}-eBx_i\right)^2\right]+\sum_{i=1}^{N}V(\mathbf{r}_i) \\ &\quad +\sum_{j=1}^{N}\sum_{i=1<j}^{N}U(|\mathbf{r}_i-\mathbf{r}_j|)\,, \end{aligned} \tag{5.5}$$

where i is the particle index of the N electrons with mass m and charge $-e$. The position vector $\mathbf{r}_i$ has two components (x_i, y_i). The magnetic field strength is denoted by B. The external single-particle potential is described by $V(\mathbf{r}_i)$ and the interparticle repulsion is determined by the isotropic potential $U(|\mathbf{r}_i-\mathbf{r}_j|)$. We have neglected the spin of the electron. The velocity operators are,

$$v_x = \sum_{i=1}^{N}\frac{1}{m}\left[-i\hbar\frac{\partial}{\partial x_i}\right] \tag{5.6}$$

$$v_y = \sum_{i=1}^{N}\frac{1}{m}\left[-i\hbar\frac{\partial}{\partial y_i}-eBx_i\right]. \tag{5.7}$$

Consider a section of the 2D sample of size $L_x \times L_y$. The wavefunction is assumed to satisfy periodic boundary conditions in the Landau gauge:

$$\psi(x_i+L_x) = e^{i\alpha L_x}e^{i(eB/\hbar)y_iL_x}\psi(x_i)\,,\ \text{and,} \tag{5.8}$$

$$\psi(y_i+L_y) = e^{i\beta L_y}\psi(y_i)\,. \tag{5.9}$$

A subtlety to note here is the appearance of y_i in the first condition which ensures that the magnetic translation operators commute with the Hamiltonian. The main objective of this calculation, the Hall conductivity, is evaluated by averaging over all periodic boundary conditions. We define a unitary transformation,

$$P = \exp\left[-i\alpha\left(x_1+x_2+\ldots+x_n\right)\right]\exp\left[-i\beta\left(y_1+y_2+\ldots+y_n\right)\right]\,, \tag{5.10}$$

with parameters α and β, which acts on an energy eigenfunction to give,

$$|\phi_n\rangle \;=\; P\,|\psi_n\rangle\,. \tag{5.11}$$

The transformed Hamiltonian is,

$$\begin{aligned} H' &= PHP^{-1} \\ &= \sum_{i=1}^{N}\left[\frac{1}{2m}\left(-i\hbar\frac{\partial}{\partial x_i}+\hbar\alpha\right)^2+\frac{1}{2m}\left(-i\hbar\frac{\partial}{\partial y_i}-eBx_i+\hbar\beta\right)^2\right]+\sum_{i=1}^{N}V(\mathbf{r}_i) \\ &\quad +\sum_{j=1}^{N}\sum_{i=1<j}^{N}U(|\mathbf{r}_i-\mathbf{r}_j|)\,. \end{aligned} \tag{5.12}$$

5.3.2 Hall conductivity

According to the Kubo formula (Sec. 4.3), the Hall conductivity, is given by,

$$\begin{aligned} \sigma_H &= \frac{ie^2\hbar}{A}\sum_{n>0}\frac{\langle\psi_0|v_x|\psi_n\rangle\langle\psi_n|v_y|\psi_0\rangle-\langle\psi_0|v_y|\psi_n\rangle\langle\psi_n|v_x|\psi_0\rangle}{(E_0-E_n)^2} \\ &= \frac{ie^2\hbar}{A}\sum_{n>0}\frac{\langle\phi_0|Pv_xP^{-1}|\phi_n\rangle\langle\phi_n|Pv_yP^{-1}|\phi_0\rangle-\langle\phi_0|Pv_yP^{-1}|\phi_n\rangle\langle\phi_n|Pv_xP^{-1}|\phi_0\rangle}{(E_0-E_n)^2}. \end{aligned} \tag{5.13}$$

Here $A = L_xL_y$ is the area under consideration. Substituting the relations,

$$Pv_xP^{-1} \;=\; \sum_{i=1}^{N}\frac{1}{m}\left[-i\hbar\frac{\partial}{\partial x_i}+\hbar\alpha\right]=\frac{1}{\hbar}\frac{\partial H'}{\partial\alpha} \tag{5.14}$$

$$Pv_yP^{-1} \;=\; \sum_{i=1}^{N}\frac{1}{m}\left[-i\hbar\frac{\partial}{\partial y_i}-eBx_i+\hbar\beta\right]=\frac{1}{\hbar}\frac{\partial H'}{\partial\beta} \tag{5.15}$$

In the expression for σ_H, we find

$$\sigma_H \;=\; \frac{ie^2}{A\hbar}\sum_{n>0}\frac{\left\langle\phi_0\left|\frac{\partial H'}{\partial\alpha}\right|\phi_n\right\rangle\left\langle\phi_n\left|\frac{\partial H'}{\partial\beta}\right|\phi_0\right\rangle-\left\langle\phi_0\left|\frac{\partial H'}{\partial\beta}\right|\phi_n\right\rangle\left\langle\phi_n\left|\frac{\partial H'}{\partial\alpha}\right|\phi_0\right\rangle}{(E_0-E_n)^2}. \tag{5.16}$$

The individual matrix elements are obtained by solving,

$$\left\langle\frac{\partial\phi_0}{\partial\alpha}\middle|H'\middle|\phi_n\right\rangle+\left\langle\phi_0\middle|\frac{\partial H'}{\partial\alpha}\middle|\phi_n\right\rangle+\left\langle\phi_0\middle|H'\middle|\frac{\partial\phi_n}{\partial\alpha}\right\rangle=0 \tag{5.17}$$

For example, the first matrix element in Eq. 5.16 is,

$$\left\langle\phi_0\middle|\frac{\partial H'}{\partial\alpha}\middle|\phi_n\right\rangle=-\left[E_n\left\langle\frac{\partial\phi_0}{\partial\alpha}\middle|\phi_n\right\rangle+E_0\left\langle\phi_0\middle|\frac{\partial\phi_n}{\partial\alpha}\right\rangle\right]. \tag{5.18}$$

Note that,

$$\left\langle \frac{\partial \phi_n}{\partial \beta} \middle| \phi_0 \right\rangle = i \left\langle \phi_n \right| \left(y_1 + y_2 + \ldots + y_N \right) \left| \phi_0 \right\rangle = - \left\langle \phi_n \middle| \frac{\partial \phi_0}{\partial \beta} \right\rangle . \tag{5.19}$$

The matrix elements in Eq. 5.16 reduce to ,

$$\begin{aligned} &\left\langle \phi_0 \middle| \frac{\partial H'}{\partial \alpha} \middle| \phi_n \right\rangle \left\langle \phi_n \middle| \frac{\partial H'}{\partial \beta} \middle| \phi_0 \right\rangle \\ &\qquad = E_n^2 \left\langle \frac{\partial \phi_0}{\partial \alpha} \middle| \phi_n \right\rangle \left\langle \phi_n \middle| \frac{\partial \phi_0}{\partial \beta} \right\rangle - E_n E_0 \left\langle \frac{\partial \phi_0}{\partial \alpha} \middle| \phi_n \right\rangle \left\langle \phi_n \middle| \frac{\partial \phi_0}{\partial \beta} \right\rangle \\ &\qquad - E_n E_0 \left\langle \frac{\partial \phi_0}{\partial \alpha} \middle| \phi_n \right\rangle \left\langle \phi_n \middle| \frac{\partial \phi_0}{\partial \beta} \right\rangle + E_0^2 \left\langle \frac{\partial \phi_0}{\partial \alpha} \middle| \phi_n \right\rangle \left\langle \phi_n \middle| \frac{\partial \phi_0}{\partial \beta} \right\rangle \\ &\qquad = (E_0 - E_n)^2 \left\langle \frac{\partial \phi_0}{\partial \alpha} \middle| \phi_n \right\rangle \left\langle \phi_n \middle| \frac{\partial \phi_0}{\partial \beta} \right\rangle \end{aligned} \tag{5.20}$$

Note that, from parity,

$$\left\langle \frac{\partial \phi_0}{\partial \beta} \middle| \phi_0 \right\rangle = -i \left\langle \phi_0 \right| \left(y_1 + y_2 + \ldots + y_N \right) \left| \phi_0 \right\rangle = 0 = \left\langle \frac{\partial \phi_0}{\partial \alpha} \middle| \phi_0 \right\rangle . \tag{5.21}$$

That allows us to drop the constraint $n > 0$ in the summations in Eq. 5.16. Equation 5.16 becomes,

$$\begin{aligned} \sigma_H &= \frac{ie^2}{A\hbar} \sum_n \frac{(E_0 - E_n)^2 \left\langle \frac{\partial \phi_0}{\partial \alpha} \middle| \phi_n \right\rangle \left\langle \phi_n \middle| \frac{\partial \phi_0}{\partial \beta} \right\rangle - (E_0 - E_n)^2 \left\langle \frac{\partial \phi_0}{\partial \beta} \middle| \phi_n \right\rangle \left\langle \phi_n \middle| \frac{\partial \phi_0}{\partial \alpha} \right\rangle}{(E_0 - E_n)^2} \\ &= \frac{ie^2}{A\hbar} \left[\left\langle \frac{\partial \phi_0}{\partial \alpha} \middle| \frac{\partial \phi_0}{\partial \beta} \right\rangle - \left\langle \frac{\partial \phi_0}{\partial \beta} \middle| \frac{\partial \phi_0}{\partial \alpha} \right\rangle \right] . \end{aligned} \tag{5.22}$$

Defining $\theta = \alpha L_x$ and $\phi = \beta L_y$,

$$\sigma_H = \frac{ie^2}{\hbar} \left[\left\langle \frac{\partial \phi_0}{\partial \theta} \middle| \frac{\partial \phi_0}{\partial \phi} \right\rangle - \left\langle \frac{\partial \phi_0}{\partial \phi} \middle| \frac{\partial \phi_0}{\partial \theta} \right\rangle \right] \tag{5.23}$$

Since we are interested in the bulk conductivity, we average over all boundary conditions. The averaged conductivity is then ,

$$\bar{\sigma}_H = \frac{1}{(2\pi)^2} \frac{ie^2}{\hbar} \int_0^{2\pi} \int_0^{2\pi} d\phi d\theta \left[\left\langle \frac{\partial \phi_0}{\partial \theta} \middle| \frac{\partial \phi_0}{\partial \phi} \right\rangle - \left\langle \frac{\partial \phi_0}{\partial \phi} \middle| \frac{\partial \phi_0}{\partial \theta} \right\rangle \right] \tag{5.24}$$

5.3.3 Quantization of $\bar{\sigma}_H$

In this subsection, using a coordinate transform we show that the Hall conductivity, as defined in Eq. 5.16, is quantized. Consider an abstract 2D space spanned by

θ and ϕ going from 0 to 2π each. In this space, we define a vector

$$\mathbf{F} = \frac{1}{2}\left[\left\langle \frac{\partial\phi_0}{\partial\theta}\middle|\phi_0\right\rangle - \left\langle\phi_0\middle|\frac{\partial\phi_0}{\partial\theta}\right\rangle\right]\hat{\theta} + \frac{1}{2}\left[\left\langle \frac{\partial\phi_0}{\partial\phi}\middle|\phi_0\right\rangle - \left\langle\phi_0\middle|\frac{\partial\phi_0}{\partial\phi}\right\rangle\right]\hat{\phi}\,. \tag{5.25}$$

The curl of $\mathbf{F}$ is,

$$\begin{aligned}\nabla\times\mathbf{F} &= \frac{1}{2}\frac{\partial}{\partial\theta}\left[\left\langle \frac{\partial\phi_0}{\partial\phi}\middle|\phi_0\right\rangle - \left\langle\phi_0\middle|\frac{\partial\phi_0}{\partial\phi}\right\rangle\right] - \frac{1}{2}\frac{\partial}{\partial\phi}\left[\left\langle \frac{\partial\phi_0}{\partial\theta}\middle|\phi_0\right\rangle - \left\langle\phi_0\middle|\frac{\partial\phi_0}{\partial\theta}\right\rangle\right] \\ &= \left[\left\langle \frac{\partial\phi_0}{\partial\phi}\middle|\frac{\partial\phi_0}{\partial\theta}\right\rangle - \left\langle \frac{\partial\phi_0}{\partial\theta}\middle|\frac{\partial\phi_0}{\partial\phi}\right\rangle\right] \\ &\quad + \frac{1}{2}\left[\left\langle \frac{\partial^2\phi_0}{\partial\theta\partial\phi}\middle|\phi_0\right\rangle - \left\langle\phi_0\middle|\frac{\partial^2\phi_0}{\partial\theta\partial\phi}\right\rangle + \left\langle \frac{\partial^2\phi_0}{\partial\phi\partial\theta}\middle|\phi_0\right\rangle - \left\langle\phi_0\middle|\frac{\partial^2\phi_0}{\partial\phi\partial\theta}\right\rangle\right]\,. \end{aligned}\tag{5.26}$$

Before reducing the expression in the second set of braces, we define operators,

$$\hat{X} = (\hat{x}_1 + \hat{x}_2 + \ldots + \hat{x}_N)\,, \tag{5.27}$$

$$\hat{Y} = (\hat{y}_1 + \hat{y}_2 + \ldots + \hat{y}_N)\,. \tag{5.28}$$

We have,

$$\left\langle\phi_0\middle|\frac{\partial\phi_0}{\partial\theta}\right\rangle = -\frac{i}{L_x}\left\langle\phi_0\right|\hat{X}\left|\phi_0\right\rangle \tag{5.29}$$

and,

$$\left\langle \frac{\partial^2\phi_0}{\partial\theta\partial\phi}\middle|\phi_0\right\rangle = -\left\langle\phi_0\right|\hat{X}\hat{Y}\left|\phi_0\right\rangle = \left\langle\phi_0\middle|\frac{\partial^2\phi_0}{\partial\theta\partial\phi}\right\rangle\,, \tag{5.30}$$

$$\left\langle \frac{\partial^2\phi_0}{\partial\phi\partial\theta}\middle|\phi_0\right\rangle = -\left\langle\phi_0\right|\hat{Y}\hat{X}\left|\phi_0\right\rangle = \left\langle\phi_0\middle|\frac{\partial^2\phi_0}{\partial\phi\partial\theta}\right\rangle\,. \tag{5.31}$$

The last term in parenthesis in Eq. 5.26 disappears on substituting Eqs. 5.30 and 5.31 reducing the curl of F to,

$$\begin{aligned}\nabla\times\mathbf{F} &= \left\langle \frac{\partial\phi_0}{\partial\phi}\middle|\frac{\partial\phi_0}{\partial\theta}\right\rangle - \left\langle \frac{\partial\phi_0}{\partial\theta}\middle|\frac{\partial\phi_0}{\partial\phi}\right\rangle \\ &= \left\langle\phi_0\right|\hat{Y}\hat{X} - \hat{X}\hat{Y}\left|\phi_0\right\rangle\,. \end{aligned}\tag{5.32}$$

One can get a deeper understanding of the physical significance of $\mathbf{F}$ by explicitly pulling out the phase component of $|\phi_0\rangle$,

$$|\phi_0\rangle = e^{i\Phi(\phi,\theta)}\,|\chi(\phi,\theta)\rangle \tag{5.33}$$

where Φ is a real function. Then we find,

$$\left\langle \frac{\partial \phi_0}{\partial \phi} \right| = -i\frac{\partial \Phi}{\partial \phi} e^{-i\Phi} \langle \chi| + e^{-i\Phi} \left\langle \frac{\partial \chi}{\partial \phi} \right| \tag{5.34}$$

$$\left\langle \frac{\partial \phi_0}{\partial \phi} \middle| \phi_0 \right\rangle = -i\frac{\partial \Phi}{\partial \phi} + \left\langle \frac{\partial \chi}{\partial \phi} \middle| \chi \right\rangle \tag{5.35}$$

$$\left\langle \phi_0 \middle| \frac{\partial \phi_0}{\partial \phi} \right\rangle = i\frac{\partial \Phi}{\partial \phi} + \left\langle \chi \middle| \frac{\partial \chi}{\partial \phi} \right\rangle . \tag{5.36}$$

Using

$$\left\langle \frac{\partial \chi}{\partial \phi} \middle| \chi \right\rangle = \left\langle \chi \middle| \frac{\partial \chi}{\partial \phi} \right\rangle \tag{5.37}$$

$$\left\langle \frac{\partial \phi_0}{\partial \phi} \middle| \phi_0 \right\rangle - \left\langle \phi_0 \middle| \frac{\partial \phi_0}{\partial \phi} \right\rangle = -2i\frac{\partial \Phi}{\partial \phi} \tag{5.38}$$

we eventually obtain

$$\begin{aligned} \mathbf{F} &= \frac{1}{2}\left[\left\langle \frac{\partial \phi_0}{\partial \theta} \middle| \phi_0 \right\rangle - \left\langle \phi_0 \middle| \frac{\partial \phi_0}{\partial \theta} \right\rangle \right] \hat{\theta} + \frac{1}{2}\left[\left\langle \frac{\partial \phi_0}{\partial \phi} \middle| \phi_0 \right\rangle - \left\langle \phi_0 \middle| \frac{\partial \phi_0}{\partial \phi} \right\rangle \right] \hat{\phi} \\ &= -i\left[\frac{\partial \Phi}{\partial \theta}\hat{\theta} + \frac{\partial \Phi}{\partial \phi}\hat{\phi} \right] \equiv -i\vec{\nabla}_{\theta,\phi}\Phi(\theta,\phi) \end{aligned} \tag{5.39}$$

So $\mathbf{F}$ is the gradient of the phase of $\phi_0(\phi,\theta)$ in an abstract(θ,ϕ) space. Now consider the integral over all boundary conditions,

$$\begin{aligned} \bar{\sigma}_H &= \frac{1}{(2\pi)^2}\frac{ie^2}{\hbar}\int_0^{2\pi}\int_0^{2\pi} d\phi d\theta \left[\left\langle \frac{\partial \phi_0}{\partial \theta} \middle| \frac{\partial \phi_0}{\partial \phi} \right\rangle - \left\langle \frac{\partial \phi_0}{\partial \phi} \middle| \frac{\partial \phi_0}{\partial \theta} \right\rangle \right] \\ &= \frac{1}{(2\pi)^2}\frac{ie^2}{\hbar}\int_0^{2\pi}\int_0^{2\pi} d\phi d\theta \, \vec{\nabla}_{\theta,\phi} \times \mathbf{F} \\ &= \frac{1}{(2\pi)^2}\frac{ie^2}{\hbar}\oint \mathbf{F}\cdot d\mathbf{s} = \frac{1}{(2\pi)^2}\frac{ie^2}{\hbar}\oint \left(-i\vec{\nabla}_{\theta,\phi}\Phi(\theta,\phi) \right)\cdot d\mathbf{s} \\ &= \frac{1}{(2\pi)^2}\frac{e^2}{\hbar}\oint d\Phi \end{aligned} \tag{5.40}$$

Here the integral in the last line is over a closed path. It is equal to $2\pi m$ where m is an integer because Φ has to be single-valued. This gives,

$$\bar{\sigma}_H = m\frac{e^2}{h}, \tag{5.41}$$

which is the result for the integer quantum Hall effect, that is the Hall conductivity is quantized in multiples of e^2/h independent of the external potential V. Correspondingly

the Hall resistivity is,

$$\bar{\rho}_H = \frac{1}{m}\frac{\hbar}{e^2} = \frac{1}{m}R_0\,. \tag{5.42}$$

5.4 Quantum Hall effect in a weak lattice potential

Here, in contrast to the previous section, we consider a 2D rotating cloud of atoms in a harmonic potential. As described earlier, when the angular velocity Ω of the cloud is equal to the frequency ω of the harmonic trap, this system can be mapped to a 2D electron gas in the presence of a magnetic field. The FQHE is seen in the latter setup when a potential difference is applied across one direction and the resistance measured in the perpendicular direction. In this section, we introduce a weak lattice potential and study the change in the Hall resistance.

The single-particle Hamiltonian for a 2D particle in the presence of rotation is,

$$\mathcal{H}_0 = -\frac{\Pi^2}{2m} + \frac{1}{2}m\left(w^2 - \Omega^2\right)r^2\,, \tag{5.43}$$

where Π is the 2D covariant momentum operator (Eq. 2.28). For the lowest Landau level (LLL) condition ($\Omega = \omega$), the unperturbed single particle executes cyclotron motion by circling around a guiding center. The guiding center coordinates are,

$$X \equiv x + \frac{1}{m\Omega}\Pi_y\,, \tag{5.44}$$

$$Y \equiv y - \frac{1}{m\Omega}\Pi_x\,. \tag{5.45}$$

In parallel with the commutation relationships listed on Page 158 in Ref. [25], one has the following for a rotating system,

$$[X, Y] = -il_B^2\,, \tag{5.46}$$

$$[\Pi_x, \Pi_y] = i\frac{\hbar^2}{l_B^2}\,, \tag{5.47}$$

$$[X, \Pi_x] = [Y, \Pi_y] = 0\,, \tag{5.48}$$

$$[X, \Pi_y] = [Y, \Pi_x] = 0\,, \tag{5.49}$$

where the harmonic oscillator length $l_B{=}\sqrt{\hbar/m\Omega}$. To obtain the quantum Hall effect, a field E_x is applied along the $x-$axis as a perturbation, $\mathcal{H}_1 = xmE_x$. The perturbation corresponding to $\mathcal{H}_1$ could, for example, be introduced by tilting the system in the presence of a gravitational field. The effect of doing this is analogous to introducing an electric field to charged particles. In the presence of a gravitational field, the mass m is analogous to the charge. In the presence of that perturbation, the single-particle Hamiltonian for the LLL is,

$$\mathcal{H} \;=\; -\frac{\Pi^2}{2m} + xmE_x. \tag{5.50}$$

The equations of motion for the guiding center of the particle are,

$$\begin{aligned}
i\hbar\frac{dX}{dt} &= [X,\mathcal{H}] = \left[X, \frac{1}{2m}\left(\Pi_x^2+\Pi_y^2\right) + xmE_x\right] = 0\,, && (5.51)\\
i\hbar\frac{dY}{dt} &= [Y,\mathcal{H}] = \left[Y, \frac{1}{2m}\left(\Pi_x^2+\Pi_y^2\right) + XmE_x - \frac{\Pi_y}{m\Omega}mE_x\right] \\
&= mE_x\,[Y,X] = imE_x l_B^2\,, && (5.52)\\
\frac{dY}{dt} &= \frac{E_x}{\Omega}\,. && (5.53)
\end{aligned}$$

For a system with a uniform particle density ρ_0 , the current along the y-direction is given by the product of the number of particles and the relevant component of the velocity of the guiding centers (Eq. 5.53),

$$J_y = m\rho_0 E_x/\Omega\,. \tag{5.54}$$

Now consider the lattice potential as a perturbation

$$V^{\rm lat}(x,y) \;=\; V_0\left(\cos^2\frac{\pi x}{d} + \cos^2\frac{\pi y}{d}\right)\,, \tag{5.55}$$

where V_0 is small in comparison to the other energy scales $\hbar\Omega$,E_x in the problem. The equations of motion for the guiding center (Eqs. 5.53 and 5.52) are now,

$$\begin{aligned}
i\hbar\frac{dY}{dt} &= imE_x l_B^2 + \left[Y, V^{\rm lat}\right] && (5.56)\\
i\hbar\frac{dX}{dt} &= \left[X, V^{\rm lat}\right] && (5.57)
\end{aligned}$$

Consider the equation of motion for Y first. Equation 5.56 reduces to,

$$i\hbar\frac{dY}{dt} = imE_x l_B^2 + \left[Y, V_0\left(\cos^2\frac{\pi}{d}\left(X - \frac{1}{m\Omega}\Pi_y\right) + \cos^2\frac{\pi}{d}\left(Y + \frac{1}{m\Omega}\Pi_x\right)\right)\right] . \quad (5.58)$$

The following commutation relationships can be derived (See Appendix B) by using a Taylor series expansion for the cosine function and $[Y, X^n] = inl_B^2 X^{n-1}$:

$$\left[Y, \cos\left(\frac{\pi}{d}X\right)\right] = -il_B^2\frac{\pi}{d}\sin\left(\frac{\pi}{d}X\right) , \text{ and,} \quad (5.59)$$

$$\left[Y, \sin\left(\frac{\pi}{d}X\right)\right] = il_B^2\frac{\pi}{d}\cos\left(\frac{\pi}{d}X\right) . \quad (5.60)$$

It is also straightforward to show

$$\left[Y, \sin\left(\frac{\pi}{m\Omega d}\Pi_y\right)\right] = \left[Y, \cos\left(\frac{\pi}{m\Omega d}\Pi_y\right)\right] = 0 . \quad (5.61)$$

Plugging these commutation relationships into Eq. 5.58 we find (the reader is referred to Appendix B for details of the calculation):

$$\left[Y, \cos^2\frac{\pi x}{d}\right] = -il_B^2\frac{\pi}{d}\sin\left(\frac{2\pi x}{d}\right) , \quad (5.62)$$

$$\left[Y, \cos^2\frac{\pi y}{d}\right] = 0 . \quad (5.63)$$

The modified equation of motion for Y is,

$$i\hbar\frac{dY}{dt} = imE_x l_B^2 - il_B^2\frac{\pi}{d}V_0\sin\left(\frac{2\pi x}{d}\right) , \quad (5.64)$$

$$\frac{dY}{dt} = \frac{E_x}{\Omega} - \frac{V_0}{m\Omega}\frac{\pi}{d}\sin\left(\frac{2\pi x}{d}\right) . \quad (5.65)$$

Similarly,

$$\frac{dX}{dt} = \frac{V_0}{m\Omega}\frac{\pi}{d}\sin\left(\frac{2\pi y}{d}\right) . \quad (5.66)$$

If the density ρ_0 is assumed to be constant, which is reasonable if the lattice potential is weak, we find for the current along the y-direction (Eq. 5.54),

$$J_y(x) = m\rho_0\frac{dY}{dt} = m\rho_0\left[\frac{E_x}{\Omega} - \frac{V_0}{m\Omega}\frac{\pi}{d}\sin\left(\frac{2\pi x}{d}\right)\right] . \quad (5.67)$$

The Hall resistance R_H is then given by

$$\frac{1}{R_H(x)} = \frac{J_y(x)}{E_x} = m\rho_0 \left[\frac{1}{\Omega} - \frac{V_0}{mE_x\Omega}\frac{\pi}{d}\sin\left(\frac{2\pi x}{d}\right)\right] . \tag{5.68}$$

In the condensed matter literature on the FQHE, one encounters a filling factor defined by the ratio of magnetic flux lines to the number of electrons per unit area. The equivalent quantity in our calculations is

$$\nu = 2\pi l_B^2 \rho_0 . \tag{5.69}$$

Rewriting the expression in terms of ν,

$$\begin{aligned} R_H(x) &= \frac{h}{m^2\nu}\left[1 - \frac{V_0}{mE_x}\frac{\pi}{d}\sin\left(\frac{2\pi x}{d}\right)\right]^{-1} \\ &= \frac{R_0}{\nu}\left[1 - \frac{V_0}{mE_x}\frac{\pi}{d}\sin\left(\frac{2\pi x}{d}\right)\right]^{-1} , \end{aligned} \tag{5.70}$$

where $R_0 = h/m^2$. The quantity R_0 maps onto the quanta of resistance in electronic systems (h/e^2). Expanding R_H to first order in V_0/mE_xd, we find

$$R_H(x) \approx \frac{R_0}{\nu}\left[1 + \frac{V_0}{mE_x}\frac{\pi}{d}\sin\left(\frac{2\pi x}{d}\right)\right] . \tag{5.71}$$

As is well-known for the electronic QHE (in the absence of a lattice), the Hall resistivity takes on simple fractional values of R_0 at fractional filling factors [25]. This calculation shows that the Hall resistance quantum is modulated spatially by a weak lattice potential. The diagonal resistance R_D is similarly modulated about a mean value of zero,

$$R_D(y) = \frac{E_x}{J_x(y)} = -\frac{R_0}{\nu}\left[\frac{V_0}{mE_x}\frac{\pi}{d}\sin\left(\frac{2\pi y}{d}\right)\right]^{-1} . \tag{5.72}$$

A useful connection stemming from this calculation is the connection between the filling factor ν (Eq. 5.69), as defined in the electronic QHE literature, and the flux per plaquette α that we have been using in Chaps. 2,3 and 4:

$$\nu = 2\pi l_B^2\rho_0 = \frac{2\pi\hbar}{m\Omega}\rho_0 = \frac{2d^2}{\alpha}\rho_0 = 2\frac{N_n}{\alpha}, \tag{5.73}$$

where N_n is the filling factor defined by the average number of particles per lattice site. The use of α to denote the flux per plaquette will be favored for the rest of this chapter.

5.5 Quantum Hall effect in rotating lattices: AC response

In this section, we study a BEC in a rotating 2D optical lattice using a Bose-Hubbard Hamiltonian modified by the rotation. Expectation values of observables are computed using wavefunctions calculated by diagonalization. We impose box boundary conditions on the wavefunctions. There are two advantages to using box boundary conditions over periodic boundary conditions. First, periodic boundary conditions are suitable only for values of α in a narrow region around rational values [60], while box boundary conditions can be used to study the system response for both rational and irrational values of α. Second, non-periodic elements (such as a trapping potential or a lattice tilt) can be introduced easily using box boundary conditions. In the case of box boundary conditions, these advantages come with the twin costs of non-negligible boundary effects and limited access, as the study of many-particle systems via the exact-diagonalization method quickly becomes intractable when increasing either lattice size or the number of particles. Since the particles we study carry no charge there is no space charge field created when particles get piled up. Hence it is advantageous to use an ac perturbation. The ac perturbation also mitigates the effects of the infinite box boundary conditions.

5.5.1 Single-particle response

This section presents numerical results for the linear transport response of a single particle in a rotating 40×40 lattice. The system is subjected to a perturbation modulated at high-enough frequency $\nu = E_R/\hbar$. The linear response is characterized in terms of the change in end currents and the sample averaged resistivity.

The ideal way to study the current and voltage characteristics of the system would be to connect it to reservoirs and compute currents between the system and reservoirs, as done in studying open quantum systems. However, this approach becomes numerically

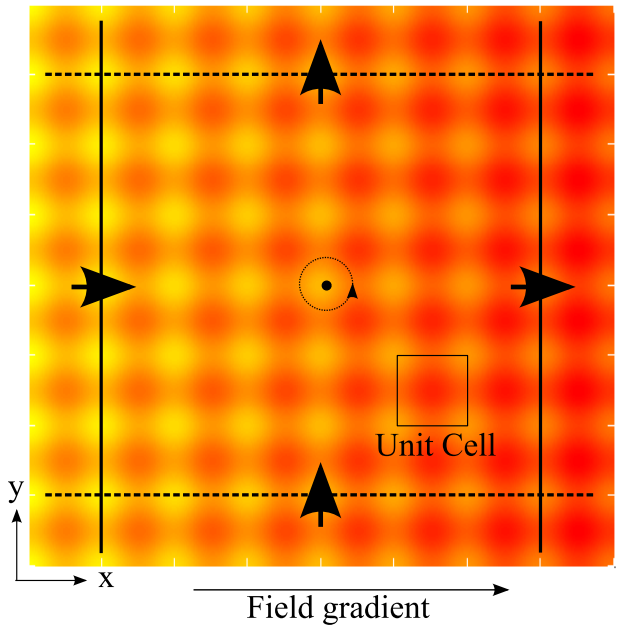

Figure 5.3: Top-view schematic depicting end currents for an 8×8 lattice. The arrows crossing the solid lines mark the longitudinal end currents $\langle \hat{J}_x^E \rangle$ while the arrows crossing the dashed lines indicate the transverse end currents $\langle \hat{J}_y^E \rangle$. The lattice is tilted to the right.

intractable for systems of size $> 4-6$ sites [64]. For an isolated system, proxies for the in and out current response of the system are the end currents — the current response of the system very close to the boundaries of the system. Note that this is true only for a linear response study. The operators for the end currents are obtained by summing current operators across end links as shown in Fig. 5.3. End currents along each direction are added on either side of the lattice in order to capture only additional currents due to the perturbation. The underlying currents and circulation of the system due to the rotation have been described in the previous chapter.

The expectation values for the end currents along the longitudinal and transverse directions are plotted in Fig. 5.4 as a function of the flux per plaquette α defined in Eq. 2.42. The longitudinal end current in Fig. 5.4(a) displays well-defined peaks at fractional values of α. At these fractional values of $\alpha = p/q$ (where p, q are integers), the

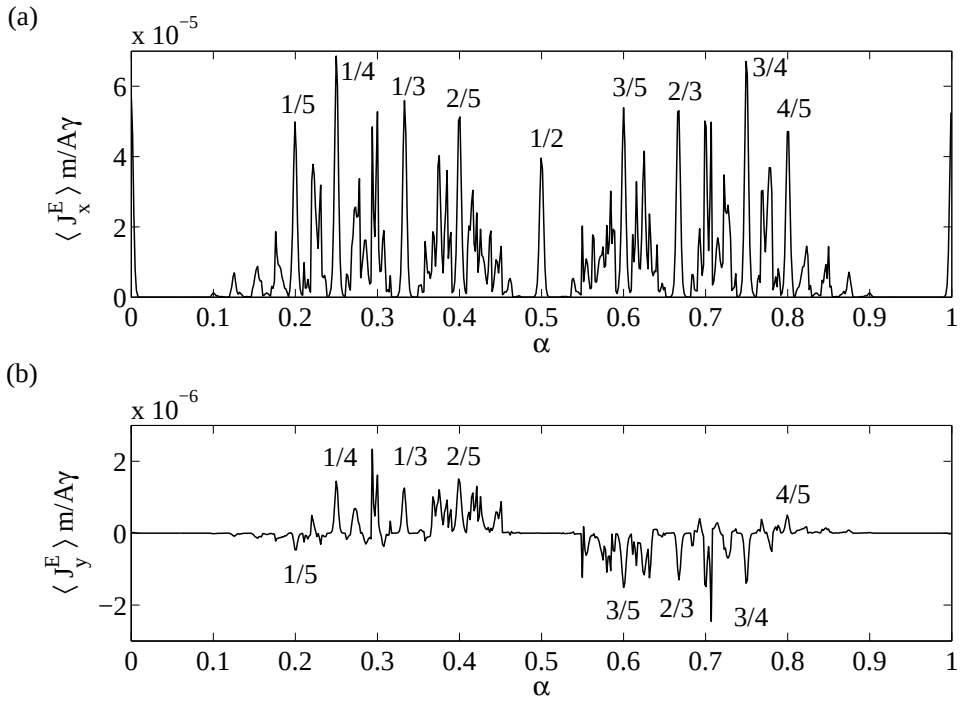

Figure 5.4: Expectation value of end currents, (a) $\langle \hat{J}_x^E \rangle$ (along the x-direction) and (b) $\langle \hat{J}_y^E \rangle$ (along the y direction), as a function of α for a single particle in a 40×40 lattice subject to a linear ramp perturbation of amplitude A modulated with a frequency $\nu = E_R/\hbar$. The mass of the particle is m and γ is a parameter described after Eq. 4.16.

energy spectrum in Fig. 2.10 breaks up into exactly q bands [36]. For low perturbation frequencies ($\hbar\nu \sim J$), the denominator in the Kubo response (Eq. 4.22) is very small for nearly degenerate states within the same band and the linear response is, in general, large. The system described in this section has implicit infinite potential walls due to the box boundary conditions and the perturbation frequency is far off resonance ($\hbar\nu = E_R \sim 50J$) in order to eliminate Bloch oscillations. Therefore, the denominator in Eq. 4.22 does not become resonant for any value of α. The peaks appear due to bigger off-diagonal current matrix elements at fractional values of α and are small due to their non-resonant character. For high frequencies, the height of the peaks goes as $1/\nu$.

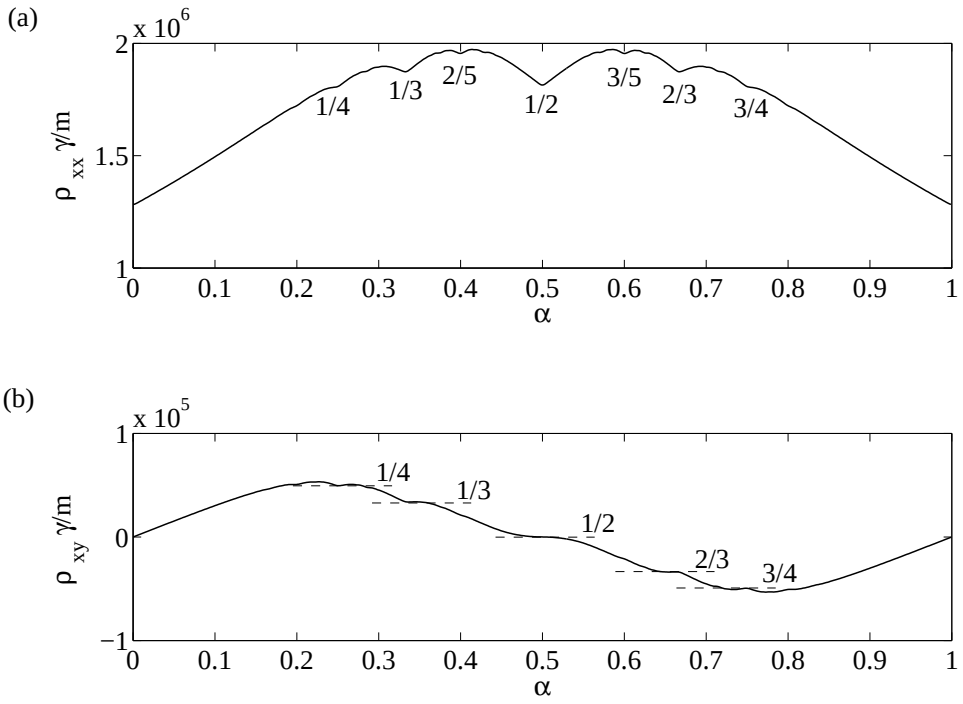

Figure 5.5: (a) Diagonal and (b) transverse resistivity Eq. 5.75 as a function of angular velocity for a single particle in a 40×40 lattice subject to a linear-ramp perturbation of amplitude E modulated with a frequency $\nu = E_R/\hbar$.

The plot of the transverse current in Fig. 5.4(b) displays peaks or dips at the same values of α as Fig. 5.4(a). The transverse end current is antisymmetric about $\alpha = 0.5$. To understand this, consider a value of $\alpha = 1 - \beta$. The corresponding angular velocity is $\Omega = (\pi\hbar/Md^2)(1-\beta)$ according to Eq. 2.42. The phase picked up by a particle going around a plaquette is $2\pi\alpha = (2\pi - 2\pi\beta) \equiv -2\pi\beta$ as shown in Fig. 2.7. The latter phase winding can equivalently be created by rotation in the opposite direction with angular velocity $\Omega = -(\pi\hbar/Md^2)\beta$ for which the Coriolis force ($\sim \mathbf{v} \times \mathbf{\Omega}$) is in the opposite direction.

As the size of the lattice under consideration gets bigger, the peak structure in Fig. 5.4 becomes more well-defined in two ways. First, the peaks become narrower as they get centered closer to exact fractional values of α, and second, more peaks appear

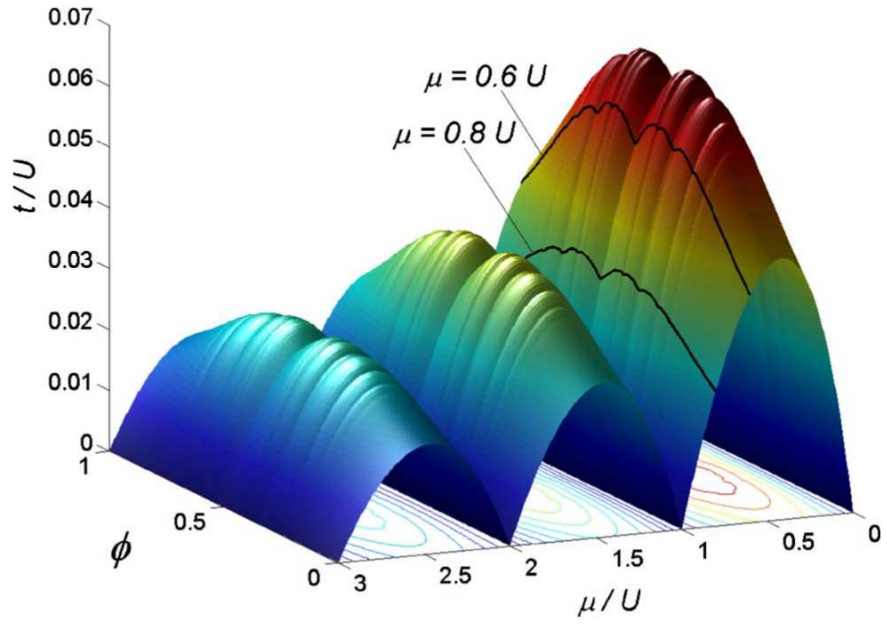

Figure 5.6: The Mott insulator-superfluid phase boundary for the first three Mott lobes as presented by Umucalilar *et al.* [80]. In their notation, the hopping term is denoted by t ($\equiv J$) and the winding parameter is ϕ ($\equiv \alpha$). The shape of the diagonal resistivity plot (Fig. 5.5(a)) resembles the cross-section of the Mott Insulator lobe at $\mu/U = 0.5$. The system behaves as an insulator for the parameter regime within the shell and as a superfluid outside.

at other fractional values of α. Both of these effects correspond to better resolution of the fractal nature of the energy spectra with bigger lattice size. The height of the peaks, however, decreases exponentially with lattice size. For example, consider the current plotted in Fig. 5.4(a). The height of the central peak empirically scales as $\sim 1.7\exp(-0.6L)$ where L is the number of sites along a side of the lattice.

A spatial average of the current response across the system smooths out the peaks in Fig. 5.4. The conductivity tensor σ_{ij} describes the response of the sample averaged current. With a perturbation along the x-direction, we can access the elements

$$\sigma_{x\mu} = \frac{\langle \Delta \hat{J}_\mu \rangle}{A}, \tag{5.74}$$

of the conductivity tensor where $\Delta\hat{J}_\mu$ is the sample averaged current along the μ direction, (*i. e.* the sum of all current operators for links along the μ direction). The

resistivity tensor elements are derived from the conductivity tensor using,

$$\rho_{x\mu} = \frac{\sigma_{x\mu}}{\sigma_{xx}^2 + \sigma_{xy}^2}\,. \tag{5.75}$$

The sample-averaged longitudinal and transverse resistivities are shown as a function of α in Fig. 5.5. The plot of the longitudinal resistivity has dips at all fractional values of α, though the dips are now seen only around prominent fractions such as $\alpha = 1/2, 1/3, 2/3, \ldots$. These fractions are the most common in the sense that for a given range of integers, these fractions can be constructed in the most number of ways. The plot of the transverse resistivity shows plateaus at values of α corresponding to these dips. Both features are signatures of the FQHE seen in a 2D electron gas. This appearance of a many-particle effect in a single-particle system is intriguing. A tentative explanation is given by considering the effect of the optical lattice. In a 2D electron gas, the combined effect of the magnetic field and the Coulombic interaction is to arrange the electrons into a lattice. For a filling factor of one, the electrons fill the lowest Landau level, forming a hexagonal lattice in the nearest neighbor approximation. The lattice spacing is $2\sqrt{\pi/3}l_B$, where $l_B \equiv \sqrt{\hbar/eB_\perp}$ is the magnetic length determined by a magnetic field $B_\perp$ [25]. In addition, the two-dimensional geometry in which electrons cannot cross each other leads to a change in phase equal to $2\pi\alpha$ each time one electron circles another. These effects are reproduced when a lattice is introduced in such a way that the particle picks up a phase of $2\pi\alpha$ going around a plaquette as illustrated in Fig. 2.7.

In Fig. 5.7, square periodic density structures are seen for the single-particle case at certain values of α, where the expectation value of the ground-state site number density for the unperturbed system has been defined as $\langle\hat{n}_i\rangle = \langle\hat{a}_i^\dagger\hat{a}_i\rangle$. At values of $\alpha = p/q$ ($\{p, q\} \in$ integers) corresponding to dips in the longitudinal resistivity, $\langle\hat{n}_i\rangle$ has a periodicity $q = \pi\hbar/md^2\Omega$. This stems from the periodicity of the hopping term in the Hamiltonian Eq. 2.37 (see also Refs. [73, 60, 80]). Bragg scattering is a promising

probe for such structures [39]. Note that the periodicity goes as $1/\Omega$ and not as $1/\sqrt{\Omega}$ as might be expected by direct comparison with the electron gas system.

As discussed in Ref. [60], for $\alpha \ll 1$ in an infinite system, the length scale of the wavefunctions is much larger than the lattice spacing and in this continuum limit, the ground state of the system is the one-half Laughlin state. In addition, the site number density distributions for α and $1-\alpha$ are identical (e. g., Figs. 5.7(b) and (f)). Therefore, the number density distribution for $\alpha = 1$ is the same as that for $\alpha = 0$ and corresponds to a system without rotation or lattice. The concentration of particles at the center [Fig. 5.7(h)] is due to the 2D infinite box potential.

5.5.2 Many-particle response

The introduction of more hard-core bosons to the two-dimensional system described earlier adds additional degrees of freedom to the problem. In the single-particle system, circling a plaquette added a phase of $2\pi\alpha$. This is still true in the many-particle system but there is an additional phase when two particles are exchanged [41], *i. e.*, $\Psi(\mathbf{x}_1, \mathbf{x}_2) = \exp(i2\pi\alpha')\Psi(\mathbf{x}_2, \mathbf{x}_1)$, where α' is a dimensionless winding rate similar to α. This substantially complicates the problem. This section extends the earlier analysis to many-particle systems using numerical results for small systems.

The energy spectrum for two hardcore bosons in a 8×8 lattice is plotted in Fig. 5.8. The overall butterfly outline seen in Fig. 2.10 is preserved. From numerical calculations, we see that for N particles, the total energy band width defined by the maximum energy difference at $\alpha = 0$, is $\Delta E_{max} = 8JN$. The gray shading describes the density of states which is marked by degeneracy at energy $E = 0$. It is difficult to delineate a band structure (if present) due to finite lattice size. However, at the most distinct regions ($\alpha \sim 0.5$), there appear to be three bands as opposed to two seen in Fig. 2.10. Diagonalization of larger many-particle systems quickly becomes intractable due to the exponential scaling of the Hilbert space dimension with particle number.

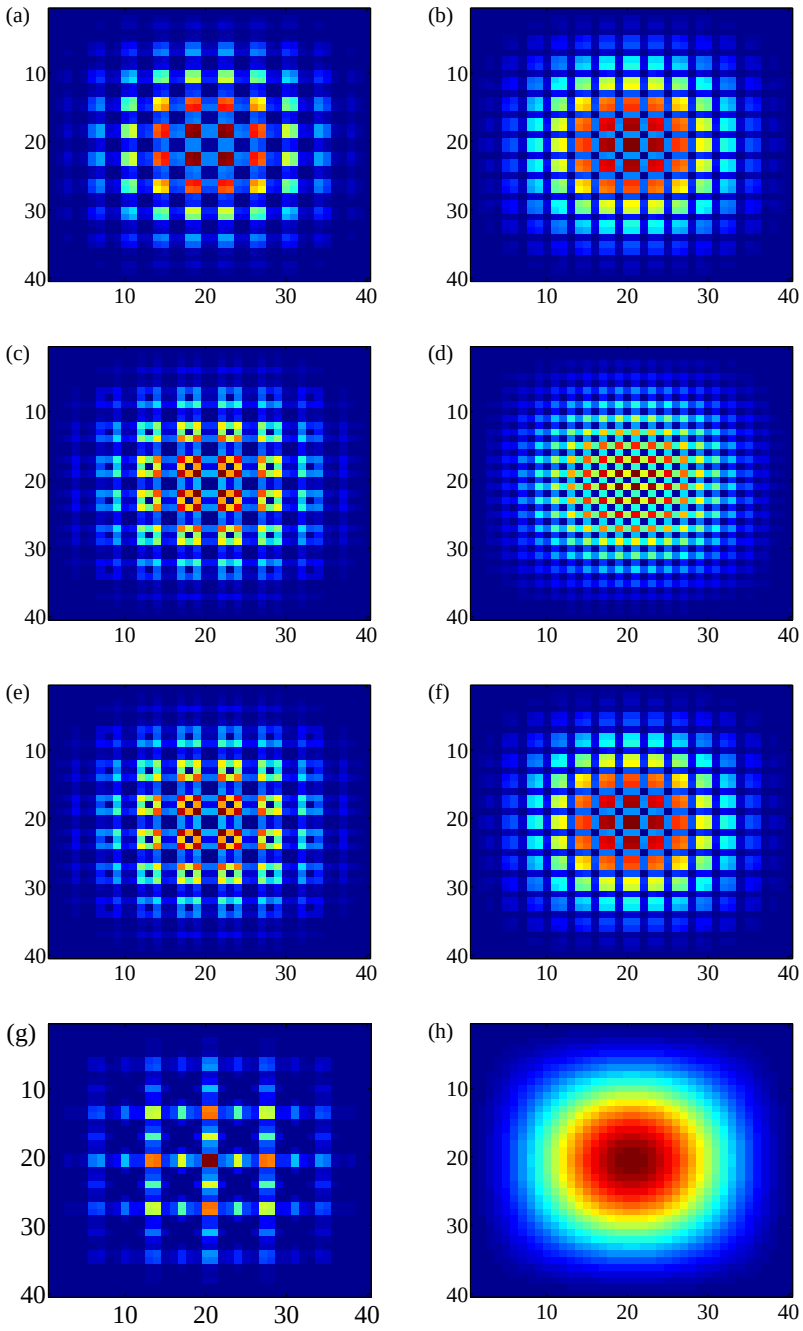

Figure 5.7: Unperturbed ground state site number-density distributions for a single particle in a 40×40 lattice for (a) $\alpha = 1/4$, (b) $\alpha = 1/3$, (c) $\alpha = 2/5$, (d) $\alpha = 1/2$, (e) $\alpha = 3/5$, (f) $\alpha = 2/3$, (g) $\alpha = \pi/11$, and (h) $\alpha = 1$. For simple fractions such as $\alpha = 1/4$ (a) or $\alpha = 1/3$ (b), the site number-density distribution has peaks separated by 4 and 3 sites respectively. For a fractional value such as $\alpha = 2/5$ (c), the number distribution has periodically arranged rings with centers separated by 5 sites. The density distributions for any value of α are the same as those for $1 - \alpha$ (compare (b) and (f) or (c) and (e)). For non rational values, e. g. $\alpha = \pi/11$ (g), the periodicity is complicated, if not destroyed. Figure 5.7(h) can be used as a reference for the color scheme: the number density increases a maximum value towards the center of the lattice. The centered 2D Gaussian-like envelope seen in all the subplots is due to 2D box boundary conditions.

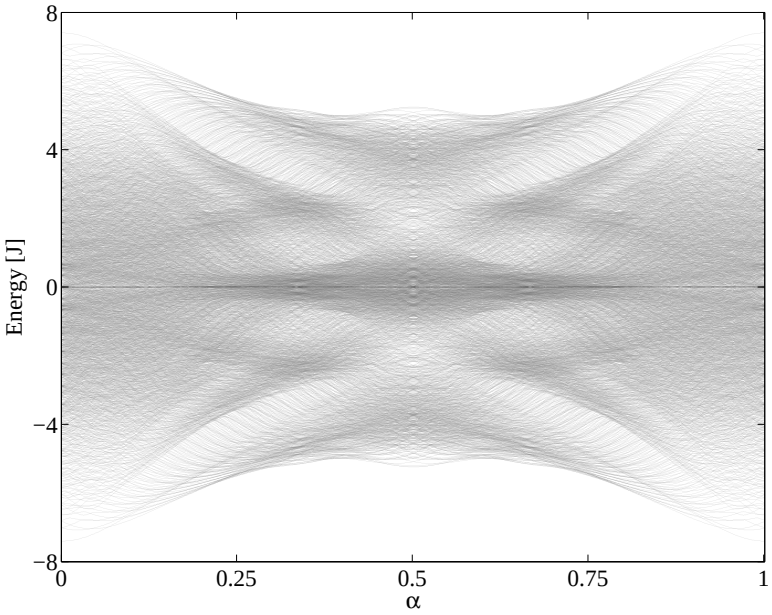

Figure 5.8: Energy spectrum for two particles in a 8×8 lattice. The gray shading marks the density of states on a natural logarithmic scale. The trapping frequency ω is set equal to the angular velocity Ω for LLL. See Fig. 2.10 for the single-particle spectra for a much larger lattice.

A useful tool for understanding the structure of a many-body state is the long range order, which, for a lattice system, can be quantified by the asymptotic behavior of the correlation function

$$g_{ij}^{(2)}(\mathbf{x}_i - \mathbf{x}_j) = \frac{\langle \hat{a}_j^\dagger \hat{a}_i^\dagger \hat{a}_i \hat{a}_j \rangle}{\langle \hat{a}_j^\dagger \hat{a}_j \rangle \langle \hat{a}_i^\dagger \hat{a}_i \rangle} \,. \tag{5.76}$$

The hardcore nature ($U \to \infty$) of the particles results in an anti-correlation envelope in the ground state seen most clearly for $\alpha = 0$ in Fig. 5.9(a). The periodicity in the Hamiltonian for rational α discussed earlier is seen in the long range order of the ground state plotted for $\alpha = 1/2$ and $\alpha = 1/3$ in Figs. 5.9(c) and 5.9(e). The Fourier transforms of the long range order in Figs. 5.9(d) and 5.9(f) show peaks at $q = 1/2d$ and $q = 1/3d$ corresponding to periodicities of two and three lattice sites respectively. Interestingly, every second site is correlated for $\alpha = 1/2$ while every third site is anti-correlated for

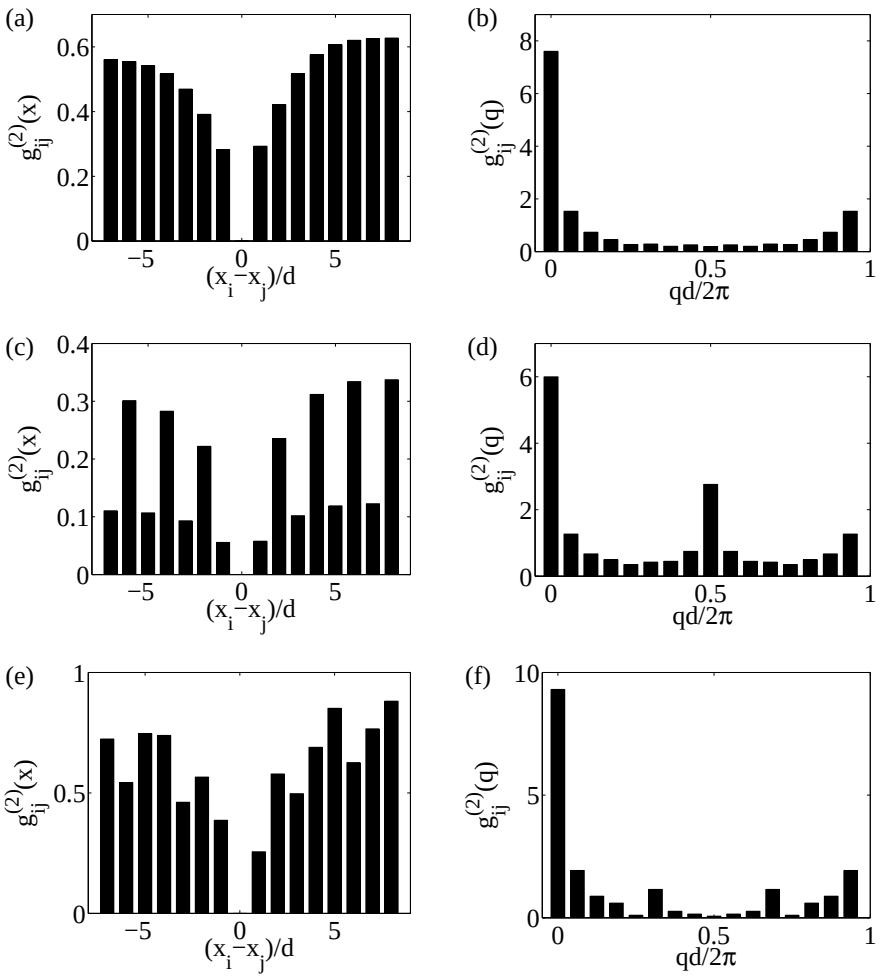

Figure 5.9: Ground state correlations Eq. 5.76 in position ($\mathbf{x}$) and quasi-momentum space (q) for two particles in a 16×16 lattice show long range order at $|x| = x_{max}$ and $q = 0$. The ground states are calculated for $\alpha = 0$ [(a) and (b)], $\alpha = 1/2$ [(c) and (d)], and $\alpha = 1/3$ [(e) and (f)]. One of the two points $\mathbf{x}_i$ is fixed close to the center of rotation while the other point $\mathbf{x}_j$ is moved to the boundary parallel to one of the edges of the lattice. The asymmetry in (a),(c) and (e) is due to $\mathbf{x}_i$ being closer to one of the infinite walls. Note that the size of the lattice under consideration is greater than 8×8 sites. This is possible here because only the ground state is needed while all eigenstates are required for the other calculations in this section.

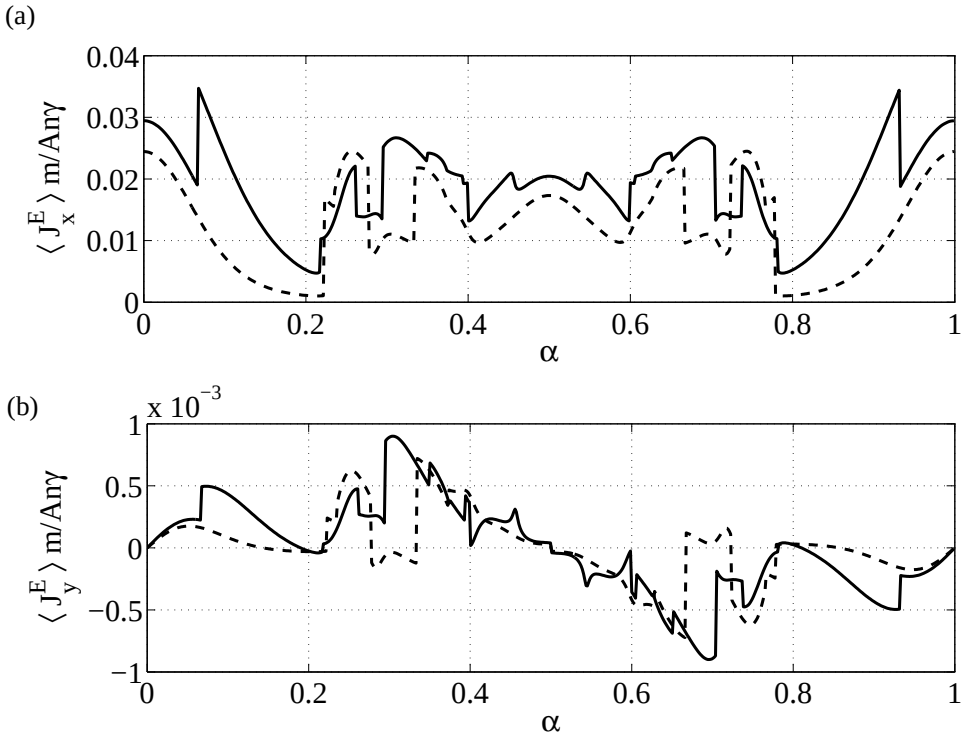

Figure 5.10: End current response per particle for one (dashed, $n = 1$) and two (solid, $n = 2$) particles in an 8×8 lattice along the (a) longitudinal direction, $\langle \hat{J}_x^E \rangle / n$, and (b) along the transverse direction, $\langle \hat{J}_y^E \rangle / n$. The perturbation is modulated at a frequency $\nu = E_R/\hbar$.

$\alpha = 1/3$.

The features of the end current response in Fig. 5.3 as a function of α for two particles in a 8×8 lattice are altered considerably due to finite-size effects in Fig. 5.10. The longitudinal $\left(\langle J_x^E \rangle\right)$ and transverse $\left(\langle J_y^E \rangle\right)$ end currents display similar features close to $\alpha = 1/2, 1/3, 2/3, 1/4, 3/4 \ldots$ though the transverse end currents are antisymmetric about $\alpha = 0.5$. Both single-particle and two-particle end-current responses are similar with a few additional peaks in the latter. In the single-particle analysis, the first distinct peaks ($\alpha = 1/2, 1/3, 2/3$) start emerging for lattice sizes $> 10 \times 10$, a size just beyond our linear-response numerical methods (that include all excited states) for two particles.

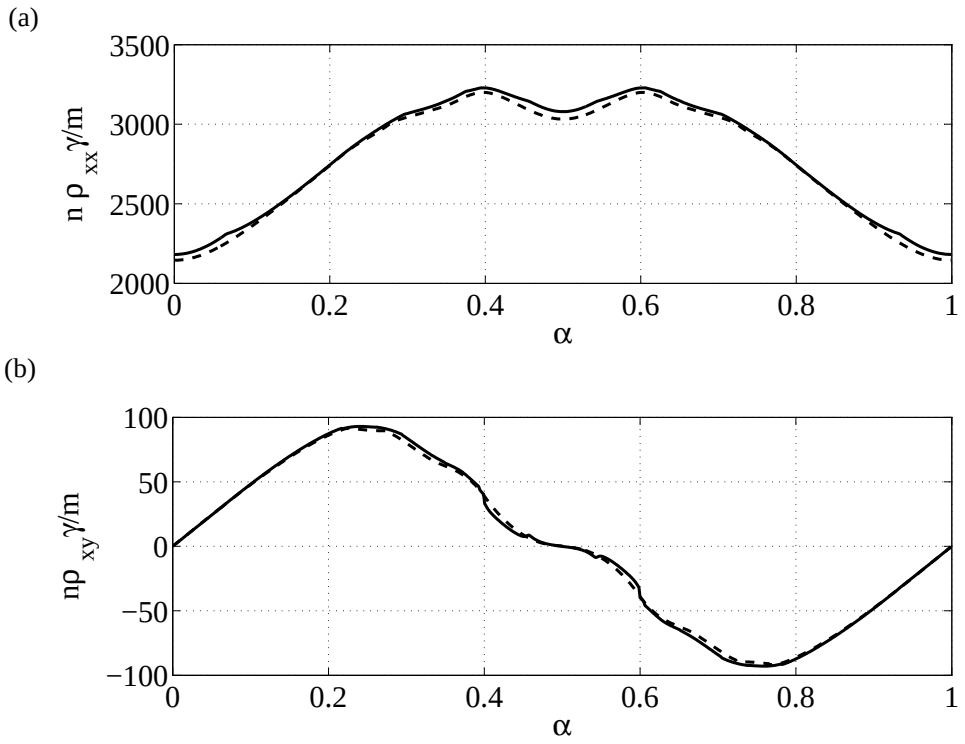

Figure 5.11: Transverse(a) and diagonal(b) resistivity scaled by the number of particles n as a function of α for one (dashed) and two (solid) particles in a 8×8 lattice. In the low filling (particles per lattice site) limit, the effect of the interactions is to decrease the conductivity per particle. The perturbation is modulated at a frequency $\nu = E_R/\hbar$.

The resistivity in Eq. 5.75 scaled by the number of particles as a function of α is plotted in Fig. 5.11. In the low-filling limit (particles/site < 0.1), the effect of the interactions between particles is to enhance the scaled resistivity or, equivalently, lower the sample-averaged conductivity per particle. This is consistent with earlier findings [10], where increasing interactions reduced the current per particle. The two particle resistivity also shows weak dips (inflections) in the longitudinal (transverse) resistivity at fractional values of α. Note that this calculation is in the very dilute limit, where the physics is largely dominated by single-particle effects.

One feature of the Hall effect is the breaking of number-density symmetry along the y–axis despite the perturbation being along the x–axis. This leads to charge buildup

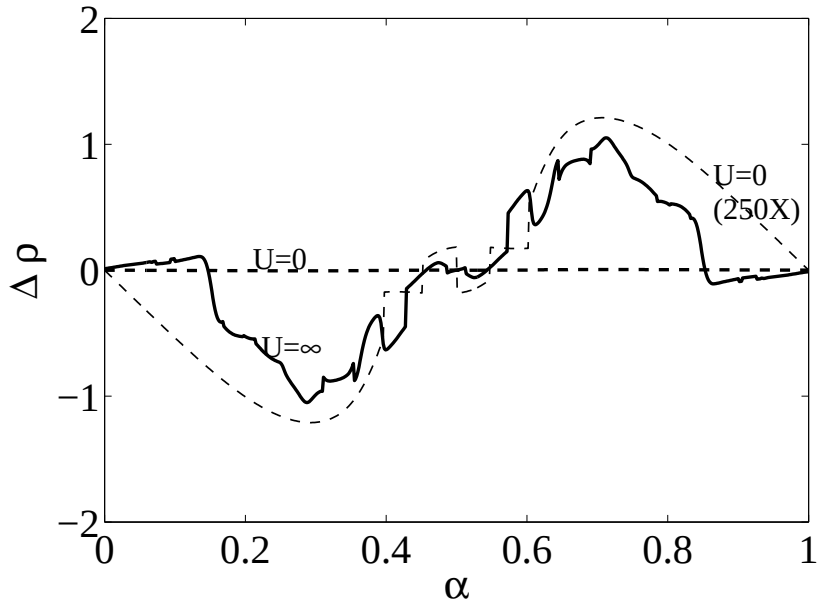

Figure 5.12: Differential density response for four particles in a 4×4 lattice in the strongly repulsive (solid) and non-interacting (dashed) limits. The two dashed lines describe the same limit but are displayed at different magnifications. In the strongly interacting limit, the redistribution due to the Coriolis force for this particular system is three orders of magnitude greater than that in the non-interacting limit.

and eventually creates a stopping Hall potential. The number-density asymmetry can be quantified by the difference in the number of particles on each half, where the lattice is divided in two along the direction of the perturbation. This quantity, $\Delta\rho = \langle\Delta\hat{\rho}_{y>0}\rangle - \langle\Delta\hat{\rho}_{y<0}\rangle$, is plotted as a function of α for four particles in a 4×4 lattice in Fig. 5.12. The effect of interaction on $\Delta\rho$ is examined by comparing the weak ($U = 0$) and strong ($U = \infty$) interaction limits. In the strongly interacting regime, the redistribution (as quantified by $\Delta\rho$) due to the Coriolis force is three orders of magnitude greater than that in the non-interacting limit. The change in the direction of particle accumulation at $\alpha = 0.5$ marks the change in the direction of the Coriolis force. Since the particles are charge neutral in this system, the retarding potential along the transverse direction is created by strong repulsive interaction between particles.

5.5.3 Conclusion

The quantum Hall effect can be interpreted as a topological effect independent of the underlying external potential. The presence of an external weak periodic potential spatially modulates the Hall resistance. Hardcore bosons in a deep rotating optical lattice are probed for the Hall effect using linear-response theory. The single-particle case exhibits fractional quantum Hall features. Density redistribution in small, strongly-correlated many-particle systems shows the equivalent of the classical effect and the mapping between the Coriolis and Lorentz forces. However, larger many-particle systems need to be considered to find the FQHE as described by dips (plateaus) in the diagonal (transverse) elements of the conductivity tensor as a function of α.

Chapter 6

Monte Carlo simulation for non-abelian systems

6.1 Introduction

The numerical results presented till now were obtained using either imaginary time propagation or exact diagonalization techniques. The former was useful to understand the implications of discretization as one adopted a Bose-Hubbard like model while the latter helped bring out important physical insights for small systems. However, exact diagonalization quickly suffers from the exponential catastrophe as the Hilbert space increases exponentially with an increase in the number of particles or the size of the system. The natural logarithm of the Hilbert space size is plotted as a function of the number of particles for several lattices in Fig. 6.1. As can be seen, the number of states quickly overwhelms our computational resources. In this context, it is useful to explore Monte Carlo methods for studying systems which are of an experimentally relevant size.

Monte Carlo methods refer to a general approach where analytically intractable integrals are evaluated by averaging over the value of the integrand at a set of randomly sampled points within the region of integration. In many physical problems, the integrand usually consists of a weighting function (typically the probability density) and the quantity of interest. For such problems, the region of integration can be profitably sampled in proportion to the weighting function using procedures such as Metropolis acceptance or heat-bath acceptance [81]. A major benefit of using Monte Carlo methods over other procedures (such as exact diagonalization) is scalability. In contrast to the

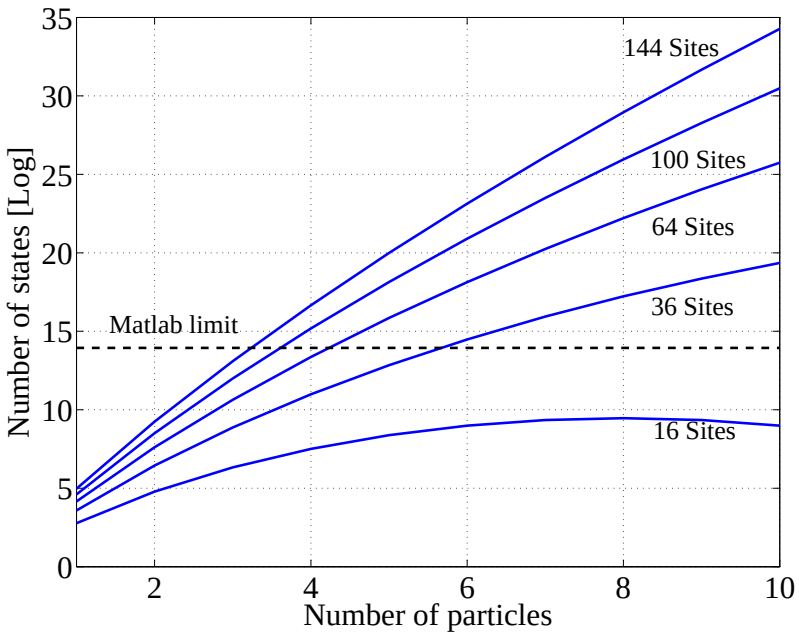

Figure 6.1: Natural logarithm of the size of Hilbert space computed for the two-state approximation as a function of lattice size and number of particles. Due to memory constraints, the computational software that we use (*Matlab*) can diagonalize only matrices smaller than a certain size. That limit is marked by the dashed line above. The number of states for the 16-site curve drops after 8 particles because of the particle-hole symmetry.

exponential increase in computational time seen for the exact diagonalization method, the amount of time required for Monte Carlo approaches scales linearly (in one dimension), or at worst polynomially, with the number of particles and the size of the lattice under consideration.

The field of Monte Carlo simulations was initiated by Lord Rayleigh in 1899 when he showed that a random walk in one dimension could be used to obtain an approximate solution to a parabolic differential equation [67]. Soon after, A. A. Markov published his landmark paper on Markov chains in 1906 [49, 50]. In a chain of Markov events, each future event depends only on the current event and is completely independent of past events. The famous Russian mathematician Andrey Kolmogorov first made the connection between Markov processes and certain differential equations on a long boat

trip down the Volga and published his results in 1931 [44] kicking off the study of diffusion theory that would eventually show up separately again in Green's function Monte Carlo simulations half a century later. The field of Monte Carlo simulations benefited substantially from the Manhattan project during the war years with major contributions from Fermi, Ulam, Neuman and Metropolis. In 1949, Metropolis and Ulam published a statistical approach to evaluating integro-differential equations [53] and coined the phrase 'Monte Carlo methods'. In 1953, Metropolis *et al.* [54] brought together the idea of using Markov chains to generate a suitably weighted distribution using a 'Metropolis acceptance' criterion where each element in the chain differed only slightly from the previous and was accepted or rejected in keeping with the desired probability distribution. By the late seventies, computers had well and truly arrived in physicial simulations and it became possible to do classical and quantum Monte Carlo (QMC) simulations. An important breakthrough for lattice problems arrived with the Suzuki-Trotter decomposition [75], which allows for a particular path integral, or a particular World Line, to be written as a product of easily computed matrix elements. Using this decomposition, Hirsch proposed the World Line Monte Carlo (WLMC) algorithm in 1982 [35].

The WLMC approach evaluates the partition function of a system by considering it as a path integral over imaginary time (or inverse temperature) with periodic boundary conditions along the Trotter (imaginary time) axis. The Trotter axis is then divided into small discrete time steps and the matrix elements for the evolution of the system from one time step to the next are easily available. Each configuration of world lines constitutes an element in the Markov chain. The configuration space is explored by deforming a world line and accepting (or rejecting) the deformation using Metropolis acceptance. The advantages of the WLMC algorithm are: The formalism is a direct representation of the physical system; The procedure is fairly quick for small systems, and; Modifications to the system can easily be incorporated. The disadvantages are two-fold: The amount of time required to reach the desired precision increases dramati-

cally as the temperature of the system approaches zero, and; The world line deformation procedure, known as the 'local update' method, fails to sample all of the configuration space. Many improvements to the local update procedure have since been proposed such as the loop/cluster algorithm [24], the worm algorithm [66] and the directed-loop algorithm [76]. All of the new methods are focussed on replacing the local update procedure with a faster and more effective procedure and these new algorithms have produced remarkable results for otherwise intractable systems, for example, strongly interacting bosons. However, due to the non-local nature of the updates, the newer updating procedures do not lend themselves to grappling with non-abelian systems such as particles in a two-dimensional system with a vector potential. When applied to such systems, the more recent algorithms succumb to a cousin of the infamous 'sign problem' associated with the QMC simulations for fermionic systems. For rotating systems, this effect manifests itself in one of two ways: Either the system always converges ('slips down') to the bosonic solution or the statistical noise increases dramatically as the winding number α associated with the vector potential increases. For this reason, we shall revert back to the original WLMC algorithm proposed by Hirsch and try to adapt it for hardcore bosons in a two dimensional rotating lattice. Other attempts to study non-abelian systems using QMC methods include efforts by Barnes *et al.* [8, 87] and Nielaba *et al.* [51, 52]. A discussion of these approaches will be presented towards the end of this chapter when the context for the descriptions is more readily available.

The first section will provide a brief sketch of the general Markov Chain Monte Carlo (MCMC) approach using Metropolis acceptance. Section 6.3 will be used to provide an outline of the WLMC algorithm as proposed by Hirsch. We will use this section as a starting point for our approach and, in particular, use comparisons with exact results for hardcore bosons in a non-rotating lattice to weed out systematic errors in the abelian limit. The non-abelian aspect of the simulation is introduced in Sec. 6.4. The source of the sign problem is identified and two potential approaches to mitigate

the problem are presented. The last section of this chapter describes other alternatives and further discussion on fundamental difficulties associated with modeling non-abelian systems using QMC methods.

6.2 Markov Chain Monte Carlo methods

Monte Carlo methods refer to a set of sampling and averaging techniques useful for evaluating difficult/complicated integrals especially when the integrals are not tractable analytically and beyond direct numerical reach. In physical problems, these integrals could be path integrals, norms, expectation values or traces. This section will provide a brief general introduction to these methods.

Consider an integral of the form $I = \int_A d\mathbf{x}\ f(\mathbf{x})$ where A denotes the region of interest. To illustrate how the Monte Carlo methods work, we consider the example of a one dimensional space where $f(x) = \sin(x)$ with $x \in [0, \pi/2]$, *i. e.*

$$I \;=\; \int_0^{\pi/2} dx \sin x = 1\,. \tag{6.1}$$

For the purposes of Monte Carlo integration, we consider the integral as,

$$\begin{aligned} I &\equiv \text{length of interval} \times \text{average value of } f(x) \\ &= \frac{\pi}{2} \times \frac{1}{N} \sum_{i=1}^{N} f(x_i)\,. \end{aligned} \tag{6.2}$$

An estimate for the average value of $f(x)$ can be obtained by randomly selecting N samples x_i within the interval $x \in [0, \pi/2]$ and averaging $f(x)$ for the sample set. As expected, the estimate for I obtained this way improves considerably as the sample size increases. As predicted by the Central Limit theorem, the error scales as $1/\sqrt{N}$ (Fig. 6.2). This approach works well for simple integrals. In many cases, the integrand might be peaked in a small region. When this is true, it is beneficial to sample the space A with a frequency proportional to a probability distribution (or *weighting* function) $p(\mathbf{x})$. The distribution function provides for greater sampling around the peaks of $f(\mathbf{x})$

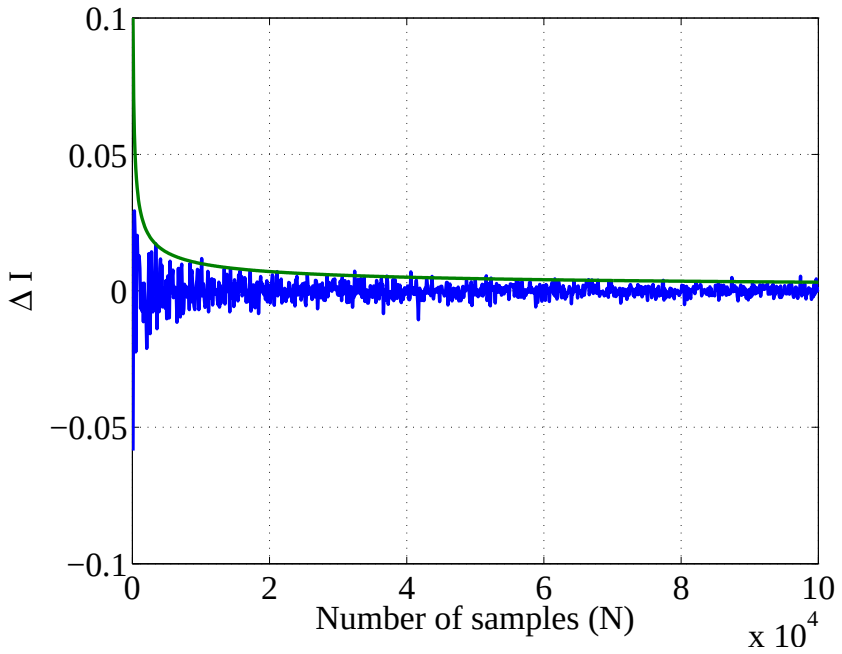

Figure 6.2: The error ΔI (blue) in evaluating integral I (Eq. 6.1) using Monte Carlo simulations as a function of sample size N. The calculation converges to zero as the sample size become large. The error goes as $1/\sqrt{N}$ (green) as described by the central limit theorem.

thus improving Monte Carlo efficiency. This technique is called *importance sampling*. In the context of quantum mechanical expectation values, $p(\mathbf{x})$ becomes the wavefunction probability density. To illustrate how importance sampling is used, suppose that $\mathbf{x}$ is distributed according to the function $p(\mathbf{x})$ where $\int_A d\mathbf{x}\, p(\mathbf{x}) = 1$. The expectation value of a function $f(\mathbf{x})$ is,

$$\langle f \rangle = \frac{\int_A p(\mathbf{x}) f(\mathbf{x})\, d\mathbf{x}}{\int_A p(\mathbf{x})\, d\mathbf{x}} \tag{6.3}$$

$$\approx \frac{1}{N} \sum_{\{x_i\}} f(\mathbf{x}_i) \tag{6.4}$$

where the sample set $\{\mathbf{x}_i\}$ is distributed according to the distribution $p(\mathbf{x})$. Such a sample set can be generated by deploying the algorithm:

- *Step 1*: Pick a random number $\mathbf{x}_i \in A$
- *Step 2*: Generate another random number $\mathbf{y}_i \in [0, 1]$

- *Step 3*: If $\mathbf{y}_i < p(\mathbf{x}_i)$, include $\mathbf{x}_i$ in $\{\mathbf{x}_i\}$ and increment N, else discard
- *Step 4*: Return to *Step 1.*

This method of importance sampling works quite well for small systems where $p(\mathbf{x})$ is easy to compute. However for many systems, $p(\mathbf{x})$ is very expensive to compute and sometimes not available at all. This is where Markov chains become important. As described in the introduction to this chapter, a Markov chain is a series of events (or states) where all future events depend only on the current event and are completely independent of past events. Metropolis *et al.* [53] put forward the idea of using a chain where each state $\mathbf{x}_i$ in the chain differs only slightly from the previous one ($\mathbf{x}_{i-1}$). In many cases, the ratio $R = p(\mathbf{x}_{i+1})/p(\mathbf{x}_i)$ is available and easy to compute. A uniformly distributed random number $r \in [0, 1]$ is generated. If $r < R$, then the state $\mathbf{x}_{i+1}$ is accepted else the old state is retained ($\mathbf{x}_{i+1} = \mathbf{x}_i$). This method of selecting states in a Markov chain is called *Metropolis acceptance* [54]. Sometimes, depending on how sensitive the system is, a slightly different acceptance condition is used *viz.* $r < R/(1 + R)$. For the Metropolis acceptance procedure to work well, two conditions must be satisfied—*ergodicity* and *detailed balance.*

Ergodicity, in this context, means that it should be possible to sample the complete phase space of the system. To quote Ceperley [17] — *There is a non-zero probability of making a move from any state to any other state in a finite number of moves.* Detailed balance ensures that after many iterations,*i. e.*, once a steady state has been reached, the probability $P(\mathbf{x}_i \rightarrow \mathbf{x}_{i+1})$ of going from state $\mathbf{x}_i$ to $\mathbf{x}_{i+1}$ and vice-versa satisfies the relationship,

$$P(\mathbf{x}_i \rightarrow \mathbf{x}_{i+1})\, p(\mathbf{x}_i) = P(\mathbf{x}_{i+1} \rightarrow \mathbf{x}_i)\, p(\mathbf{x}s_{i+1}). \tag{6.5}$$

For further discussion on the technical aspects, the reader is referred to several excellent reviews on the topic available such as Ref. [9, 17, 81] and references therein.

6.3 World Line Monte Carlo

The World Line Monte Carlo (WLMC) method is a way of studying D-dimensional quantum systems by doing classical simulations in $D+1$-dimensions. This section is divided into three parts: The first part lays down the formalism esoteric to the WLMC method; The second part outlines the WLMC algorithm; the third compares WLMC results to those obtained from exact diagonalization for non-rotating systems in order to understand the effects of the Trotter error [75] and see how the algorithm scales with lattice size and particle number.

6.3.1 Formalism

A world line tracks the evolution of a particle in D-dimensional real or momentum space as a function of time. Accordingly, the World Line Monte Carlo (WLMC) method is a Markov chain method in $D+1$ dimensions where the different world lines are randomly sampled using Metropolis acceptance. One can think of WLMC as Path Integral Monte Carlo (PIMC) applied to a lattice model [17]. Hence, there are many close connections to PIMC but one major difference between the two approaches is that the PIMC formalism starts with the action while the WLMC approach starts with the expression for the partition function given by,

$$Z = Tr\left(e^{-\beta\hat{\mathcal{H}}}\right), \tag{6.6}$$

where β is the inverse temperature (we use units with $k_B \equiv 1$), and $\hat{\mathcal{H}}$ the Hamiltonian for the system under consideration. If the Hamiltonian can be written as a sum of M non-commuting parts, $\hat{\mathcal{H}}_i$, the Suzuki-Trotter decomposition [75] can be deployed to

rewrite the trace as,

$$\begin{aligned} Z &= Tr\left(\exp\left[-\beta\sum_{i}^{M}\hat{\mathcal{H}}_i\right]\right) \\ &\equiv Tr\left(\left[\exp\left(-\frac{\beta}{m}\hat{\mathcal{H}}_1\right)\exp\left(-\frac{\beta}{m}\hat{\mathcal{H}}_2\right)\ldots\exp\left(-\frac{\beta}{m}\hat{\mathcal{H}}_M\right)\right]^m\right)+\mathcal{O}\left(\frac{\beta^2}{m^2}\right) \\ &= Z_m+\mathcal{O}\left(\frac{\beta^2}{m^2}\right). \end{aligned} \tag{6.7}$$

Here, the subscript m indicates that Z_m is the m^{th}-approximant of Z. One can also think of the inverse temperature β as the imaginary time. Then dividing β by m corresponds to dividing the imaginary time axis into slices of width $\Delta\tau = \beta/m$. The last term in Eq. 6.7 above is called the Trotter error and is the error due to the non-commutativity of $\hat{\mathcal{H}}_i$. For the two-dimensional Bose-Hubbard Hamiltonian we are interested in, one can rewrite the Hamiltonian as the sum of four non-commuting parts,

$$\hat{\mathcal{H}} \equiv \hat{\mathcal{H}}_{x,\text{odd}}+\hat{\mathcal{H}}_{x,\text{even}}+\hat{\mathcal{H}}_{y,\text{odd}}+\hat{\mathcal{H}}_{y,\text{even}} \tag{6.8}$$

where the terms on the right hand side represent the energy associated with the links marked in Fig. 6.3. For the purposes of this chapter the system we study is described by the Hamiltonian,

$$\hat{\mathcal{H}} = -J\sum_{\langle i,j\rangle}\left(\hat{a}_i\hat{a}_j^\dagger e^{i\phi_{ij}}+\hat{a}_i^\dagger\hat{a}_j e^{-i\phi_{ij}}\right), \tag{6.9}$$

discussed in Eq. 2.37. Note that the onsite energy terms have been dropped. They can easily be included after rewriting them to reflect their contribution to links as opposed to sites. The trace of the approximate partition function Z_m is evaluated by inserting complete sets of Fock states $|v_i\rangle$,

$$\begin{aligned} Z_m &= \sum_{\{v_1\}}\left\langle v_1\left|e^{-\Delta\tau\hat{\mathcal{H}}_{x,odd}}e^{-\Delta\tau\hat{\mathcal{H}}_{x,even}}e^{-\Delta\tau\hat{\mathcal{H}}_{y,odd}}e^{-\Delta\tau\hat{\mathcal{H}}_{y,even}}\ldots m\text{ times}\right|v_1\right\rangle \\ &= \sum_{\{v_1,v_2\ldots v_{4m}\}}\left\langle v_1\left|e^{-\Delta\tau\hat{\mathcal{H}}_{x,odd}}\right|v_2\right\rangle\left\langle v_2\left|e^{-\Delta\tau\hat{\mathcal{H}}_{x,even}}\right|v_3\right\rangle\ldots\left\langle v_{4m}\left|e^{-\Delta\tau\hat{\mathcal{H}}_{y,even}}\right|v_1\right\rangle. \end{aligned} \tag{6.10}$$

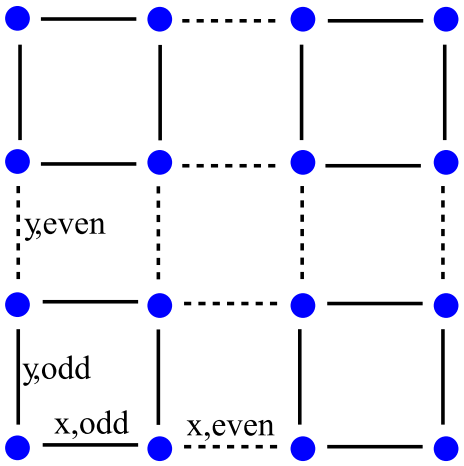

Figure 6.3: Schematic for disaggregating a 2D lattice model into four non-commuting sets of links: x,odd - horizontal solid; x,even - horizontal dashed; y,odd - vertical solid, and ; y, even - vertical dashed. An alternative decomposition is obtained by considering the lattice to consist of two intersecting sets of plaquettes as bounded by the solid and dashed lines [68].

Consider a particular matrix element [81]:

$$\begin{aligned}
&\left\langle v_1 \left| e^{-\Delta\tau \hat{H}_{x,odd}} \right| v_2 \right\rangle \\
&= \left\langle v_1 \left| \exp\left(\Delta\tau J \sum_{\langle i,i+1\rangle_x} \hat{a}_i \hat{a}_{i+1}^\dagger e^{i\phi_{i,i+1}} + \hat{a}_i^\dagger \hat{a}_{i+1} e^{-i\phi_{i,i+1}} \right) \right| v_2 \right\rangle \\
&= \prod_{i \text{ odd}} \langle R_i R_{i+1}| \prod_{\langle i,i+1\rangle} \exp\left[\Delta\tau J \left(\hat{a}_{i+1}^\dagger \hat{a}_i e^{i\phi_{i,i+1}} + \hat{a}_i^\dagger \hat{a}_{i+1} e^{-i\phi_{i,i+1}} \right) \right] \prod_{i \text{ odd}} \left| R_i' R_{i+1}' \right\rangle \\
&= \prod_{\langle i,i+1\rangle} \left\langle R_i R_{i+1} \left| \exp\left[\Delta\tau J \left(\hat{a}_{i+1}^\dagger \hat{a}_i e^{i\phi_{i,i+1}} + \hat{a}_i^\dagger \hat{a}_{i+1} e^{-i\phi_{i,i+1}} \right) \right] \right| R_i' R_{i+1}' \right\rangle . \qquad (6.11)
\end{aligned}$$

Here i is a site index and $R_i \in [0,1]$ indicates whether the site is occupied or not by a hardcore boson. All matrix elements can be tabulated since R_i can take on only the values 0 or 1 (see Appendix C for details of the calculation):

$$\begin{aligned}
\left\langle 10 \left| e^{-\Delta\tau \hat{\mathcal{H}}_{ij}} \right| 10 \right\rangle &= \left\langle 01 \left| e^{-\Delta\tau \hat{\mathcal{H}}_{ij}} \right| 01 \right\rangle = \cosh(J\Delta\tau) \\
\left\langle 01 \left| e^{-\Delta\tau \hat{\mathcal{H}}_{ij}} \right| 10 \right\rangle &= \left\langle 10 \left| e^{-\Delta\tau \hat{\mathcal{H}}_{ij}} \right| 01 \right\rangle^\dagger = e^{i\phi_{ij}} \sinh(J\Delta\tau) \\
\left\langle 00 \left| e^{-\Delta\tau \hat{\mathcal{H}}_{ij}} \right| 00 \right\rangle &= \left\langle 11 \left| e^{-\Delta\tau \hat{\mathcal{H}}_{ij}} \right| 11 \right\rangle = 1 . \qquad (6.12)
\end{aligned}$$

Note that these matrix elements are very similar to those discussed by Hirsch *et al.* [35] except for the phase term introduced when the particle hops from one site to a neighboring site. This phase accumulates when the particle continues hopping and represents the flux[1] . We present a more detailed discussion on the implications of the additional phase factor in the next section. The trace of the partition function (Eq.6.10)

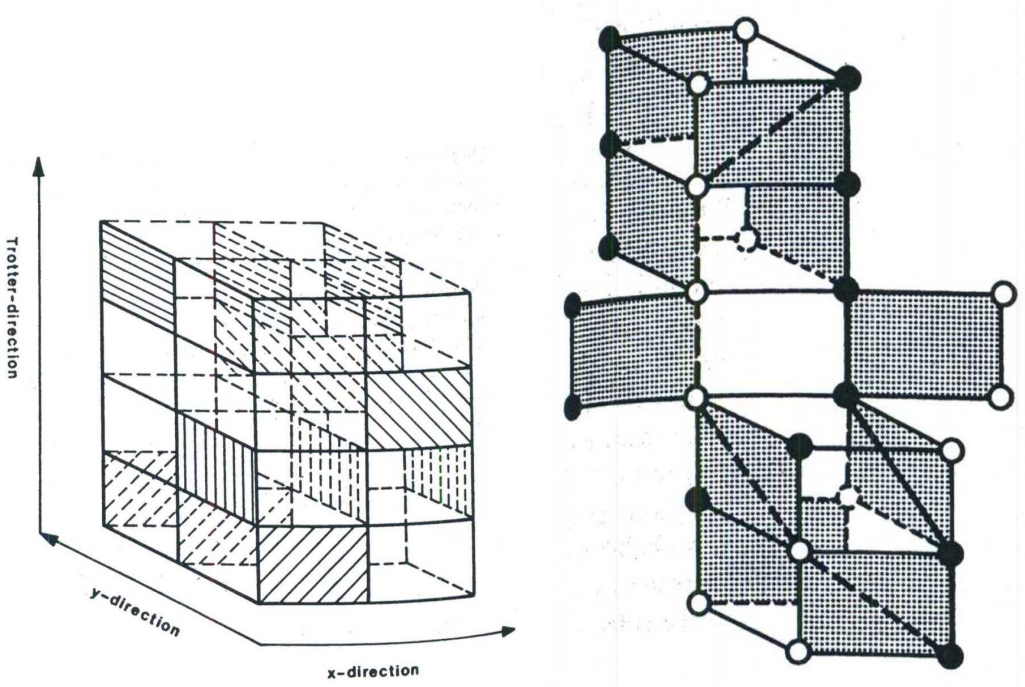

Figure 6.4: (Left) Unit cell of the three-dimensional checkercube. Each time slice is divided into four sub-slices with each sub-slice corresponding to the action of one part of the Hamiltonian in Eq. 6.8. World lines live along the edges of the shaded tiles and can only diagonally across shaded tiles; (Right) An illustration of a local update. The solid line is the original world line and the dashed line describes the proposed move. The full dots are occupied time-space coordinates. A segment of the world line is shifted by one lattice spacing after determining that the target sites are vacant and the move only includes diagonal traversals of shaded tiles. Both schematics were obtained from Ref. [56]

can be considered as a sum of worldlines that have periodic boundary conditions along the Trotter time axis. Each worldline can be represented on a checkercube with each layer corresponding to an imaginary time slice (Fig. 6.4). The shaded tiles correspond

[1] In analogy with magnetic flux, the flux here is the product of the area enclosed by the path and the scaled angular velocity α.

to the action of the individual Hamiltonian components described in Eq. 6.8. If the world line goes along the side of a shaded tile, it picks up a factor of $\cosh(J\Delta\tau)$ and if it crosses a shaded tile it picks up a factor of $\exp(\pm i\phi_{ij})\sinh(J\Delta\tau)$. Accordingly the trace of the partition function is,

$$Z_m = \sum_{\{W\}} e^{i\sum_W \phi_{ij}} \sinh^{N_d(W)}(J\Delta\tau)\cosh^{N_s(W)}(J\Delta\tau)\ , \tag{6.13}$$

where the sum is over all possible world lines and $\sum_W \phi_{ij}$ adds the phases from all diagonal jumps along a given world line. The exponents $N_d(W)$ and $N_s(W)$ correspond to the number of diagonal and straight edges of a particular world line W. The sum of phase factors is resolved in the following way: Consider a single particle world line represented by $\{(x_i, y_i)\}$ where x_i and y_i indicate the position of the particle at the i^{th} time slice. When a particle hops from one site (at time i) to another (at time $i+1$), the phase picked up by the particle is given by,

$$\phi_{ij} = 2\pi\alpha \cdot \frac{1}{2}(x_i y_{i+1} - x_{i+1} y_i) \tag{6.14}$$

The total phase picked up by the world line is

$$\sum_W \phi_{ij} = \sum_{i=1}^{m-1} \phi_{ij} = 2\pi\alpha \sum_{i=1}^{m-1} \frac{1}{2}(x_i y_{i+1} - x_{i+1} y_i) = 2\pi\alpha\Phi(W)\,. \tag{6.15}$$

Geometrically, the sum represents the area enclosed by a polygon whose coordinates are given by (x_i, y_i). Hence, $\Phi(W)$ is the total area enclosed by the worldline or the flux associated with the world line. For the next two sub-sections, we shall keep $\alpha = 0$ for robust implementation of the standard procedure.

6.3.1.1 Algorithm

The WLMC algorithm for the two-dimensional Bose-Hubbard Hamiltonian (Eq. 6.8) is as follows:

Step 1 - Initialize state: Generate a random starting 2D configuration: Let the sites be labelled by $i = 1..N_s$; Choose a site at random and put a particle there;

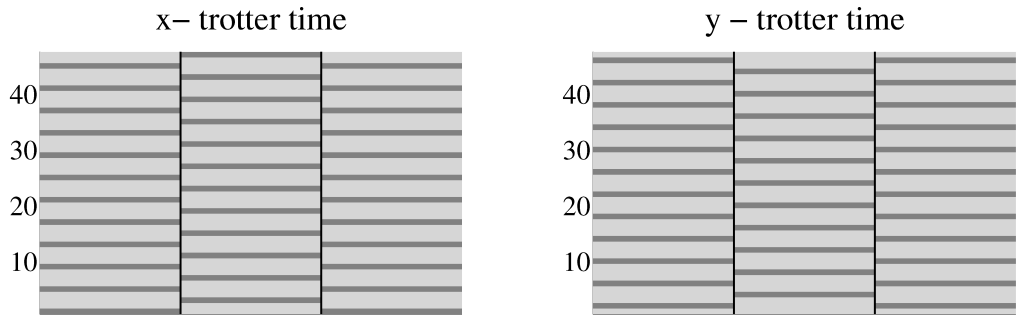

Figure 6.5: Front and side views of the checkercube containing the initial world lines for two particles in a 4×4 lattice. World lines are created by replicating the initial configuration along the Trotter time axis.

Repeat with remaining unoccupied sites until all particles have been placed.

Step 2 - Create world lines: The initial world lines are created by imposing periodic boundary conditions along the Trotter time axis and connecting the ends with straight lines as shown in Fig. 6.5.

Step 3 - Make a local update: As described earlier, due to the nature of the decomposition, each worldline can only travel along the sides or diagonally across dark shaded tiles. These world lines are updated as described in Fig. 6.4, *i. e.*, by moving the worldline across the light colored regions. The updates are accepted or rejected using Metropolis acceptance. To illustrate the update procedure, consider a move along the x-axis. A quantity s can be defined as follows,

$$\begin{aligned} s = & \, n(i,j,t) + n(i,j',t+1) + n(i,j'',t+2) + n(i,j''',t+3) \\ & - n(i+1,j,t) - n(i+1,j',t+1) - n(i+1,j'',t+2) - n(i+1,j''',t+3). \end{aligned} \quad (6.16)$$

where $n(i,j,t) = 1$ if the site indexed by (i,j) is occupied at time slice t and is zero otherwise. The fixed y-coordinates for this move are labelled by j', j'', j'''. A move is possible if $s = 4$ indicating that the sites one step to the right are vacant. The ratio of the contributions of the new and old configurations to the partition function is

$$R \;=\; \tanh^{2u}(J\Delta\tau)\cosh^{-2v}(J\Delta\tau) \quad (6.17)$$

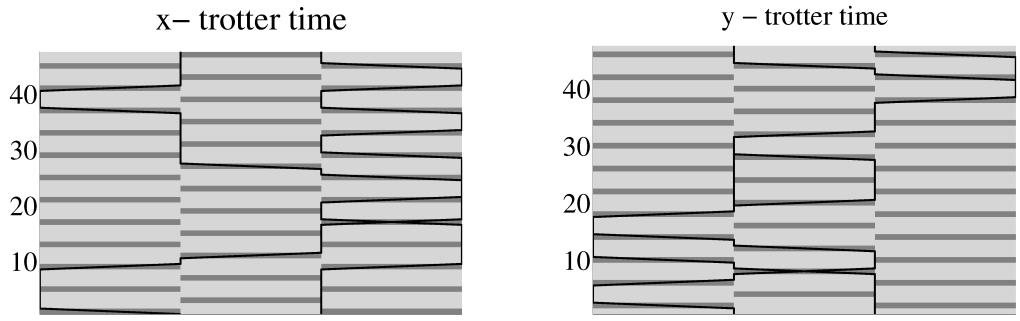

Figure 6.6: Front and side views of the checkercube showing the same world lines in Fig. 6.5 after 100 update sweeps.

where $u = 1 - n(i+1, j, t-1) - n(i+1, j, t+4)$ (see also Hirsch [35]) and v is the incremental change in the number of shaded tiles with a world line on either side. Note that $u \in \{0, \pm 1\}$ and that the other sinh and cosh factors cancel since the rest of the world line remains unchanged. The update is accepted with probability,

$$P = \min\left(1, \frac{R}{1+R}\right) \tag{6.18}$$

The current implementation differs from that used by Hirsch in terms of using a second data structure for keeping track of world lines and making updates along the worldlines as opposed to sweeping the lattice. The advantages of doing this are mostly tactical: It becomes possible to keep track of the flux associated with each world line, and; The updates are more efficient because sweeps are confined to only worldlines in contrast to the examining the entire checker cube.

Step 4: Thermalize the system The system is warmed up by running multiple local update sweeps. Shown in Fig. 6.6 are the world lines for 2 particles in a 4x4 lattice with 48 time slices after 100 update sweeps. The worldlines appear to intersect because they are in different planes. The amount of real space sampled goes up directly with the number of time steps. The total number of shaded squares with world lines going diagonally across are counted towards N_d.

Step 5: Start accumulating quantities of interest For example, the expectation value for the energy can be calculated using [81],

$$\begin{aligned} E &= -\frac{1}{Z_m}\frac{\partial Z_m}{\partial \beta} \\ &= -\sum_{\{W\}} \frac{\xi^{N_d(W)}}{Z_m}\zeta^{mN_p} \times J\left[\left(4N_p - \frac{1}{m}N_d(W_p)\right)\xi + \frac{1}{m\xi}N_d(W_p)\right] \end{aligned} \tag{6.19}$$

where $\xi = \tanh(J\Delta\tau)$ and $\zeta = \cosh(J\Delta\tau)$. Since the Markov chain is generated with the probability, $P \equiv \xi^{N_d(W)}/Z$ (the cosh term gets cancelled in the Metropolis acceptance test). The average value for the energy is given by,

$$E = -\frac{4J}{M}\sum_{\{W\}}\left[N_p\xi + \frac{N_d(W)}{m}\left(\frac{1}{\xi} - \xi\right)\right] \tag{6.20}$$

where M is the total number of measurements. Other accessible expectation values include the site number density and density-density correlation function [81]. It is important to note that the distribution generated by the Metropolis acceptance satisfies the ergodicity condition only for $\alpha = 0$. For $\alpha \neq 0$, it is non-trivial to generate the right world line distribution using Metropolis acceptance.

6.3.2 Comparison with exact diagonalization solutions for zero rotation

As a starting point, we implement the WLMC routine for hard core bosons in a 2D lattice with box boundary conditions using the usual Bose - Hubbard Hamiltonian,

$$\hat{H} = -J\left(\hat{a}_i^\dagger \hat{a}_j + \hat{a}_i \hat{a}_j^\dagger\right). \tag{6.21}$$

To test the routine, we compare ground state energies with zero-temperature results obtained using exact diagonalization. The temperature for the following Monte Carlo runs was held constant at $T = \beta^{-1} = 4/(\Delta\tau m) = 4/(0.1 \times 1024) = 0.039J$.

Single particle simulations: In the first set of runs, we compare the single particle ground state energy as obtained using the WLMC routine with the energy obtained using exact diagonalization. Figure 6.7 shows the ground state energy as

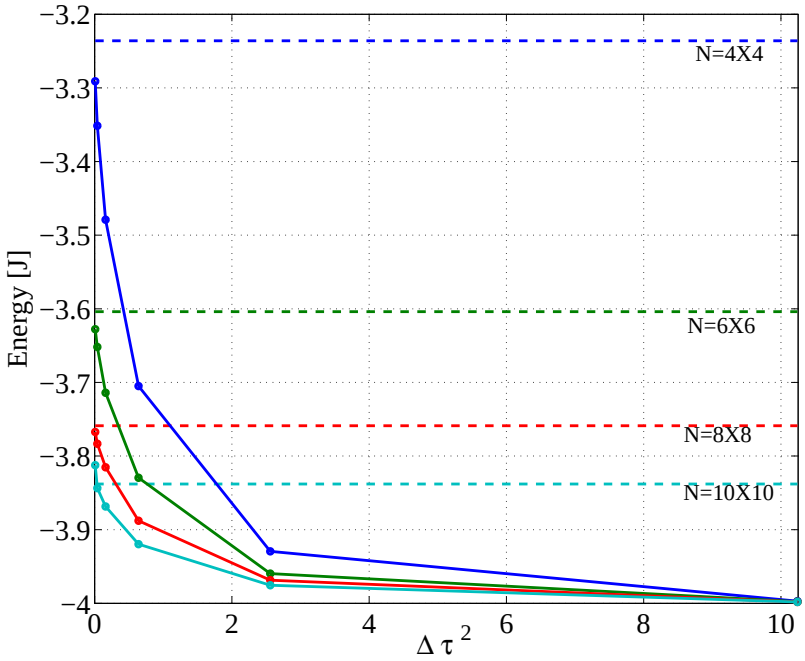

Figure 6.7: Comparison of WLMC results for the ground state energy compared with those obtained using exact diagonalization for a single particle in a non-rotating lattice of size $N_L = \{16, 36, 64, 100\}$. The WLMC results converge to exact diagonalization results with a decrease in the Trotter time step size and with increase in lattice size. The thermalization for the simulations in this section comprises of 10000 sweeps and measurements were made for an additional 10000 sweeps.

a function of Trotter time step size squared ($\Delta\tau^2$) for different lattice sizes ($N_L = \{16, 36, 64, 100\}$). The dashed lines mark the ground state energies obtained via exact diagonalization. As expected for small $\Delta\tau$, the error $E_{\rm MC} - E_{\rm exact} \sim \mathcal{O}\left(\Delta\tau^2\right)$. In addition, the Trotter error decreases with increasing lattice size, *i. e.*,

$$\Delta E = E_{\rm MC} - E_{\rm exact} \quad \propto \quad -\frac{\Delta\tau^2}{N_L^a}\,. \tag{6.22}$$

where a is an uncalculated constant. Simulation time only marginally scaled with lattice size but was directly proportional to the number of time slices (and inversely proportional to $\Delta\tau$).

Many-particle simulations: In the second set of runs, we fix the lattice size at $N_L = 36$ sites and perform simulations for $n = 1, 2, 3$ and 4 particles. Exact

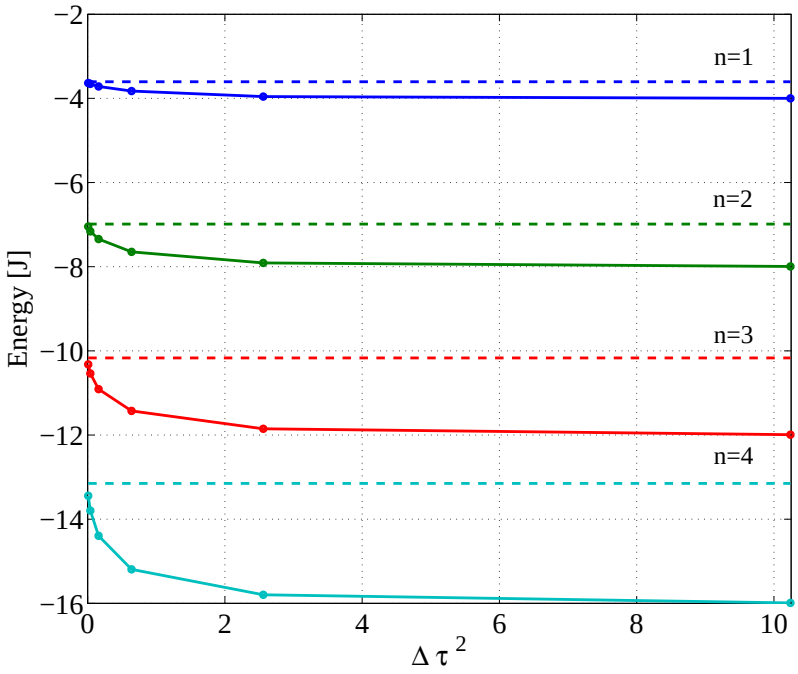

Figure 6.8: Comparison of WLMC results for the ground-state energy compared with those obtained using exact diagonalization for $n = 1, 2, 3, 4$ particles in a non-rotating 6×6 lattice. As before, the WLMC results converge to the exact results with a decrease in the Trotter time-step size and deteriorate with increase in particle number. The thermalization for the simulations in this section comprised of 1000 sweeps and measurements were made for an additional 5000 sweeps.

diagonalization results (using our earlier methods) are not available for more particles in a similar lattice because the requirements to store and work with the massive Hilbert space were numerically infeasible. The runs indicate that the Trotter error increases with the number of particles (Fig. 6.8),

$$E_{\mathrm{MC}} - E_{\mathrm{exact}} \quad \propto \quad -\Delta\tau^2 n^b \,, \tag{6.23}$$

where b is another unknown constant. Also importantly, the simulation time scaled linearly with the number of particles.

In conclusion, the WLMC routine works well for studying particles in stationary lattices: The Trotter error can be reduced to an arbitrarily small number by choosing a small Trotter step size. (however, for smaller Trotter step sizes, the acceptance ratio

is also smaller and hence the simulation becomes more inefficient),

$$\Delta E_{\text{Trotter}} = E_{\text{MC}} - E_{\text{exact}} \propto -\frac{\Delta\tau^2 n^b}{N_L^a}\,, \tag{6.24}$$

and; The time taken to perform the procedure scales linearly with the number of particles without being very sensitive to the lattice size.

6.4 WLMC for non-abelian systems

When rotation is switched on (*i. e.* $\alpha \neq 0$), the WLMC method discussed above produces imaginary transition probabilities. The probability ratio R as defined in Eq.6.17 becomes,

$$R = \frac{e^{i2\pi\alpha\Phi(W')}\xi^{N_d(W')}\zeta^{N_s(W')-N_{adj}(W')}}{e^{i2\pi\alpha\Phi(W)}\xi^{N_d(W)}\zeta^{N_s(W)-N_{adj}(W)}} = e^{i2\pi\alpha\Delta\Phi}\xi^{2u}\zeta^{-2v}\,, \tag{6.25}$$

where $\Delta\Phi = \Phi(W') - \Phi(W)$ ($\Delta\Phi \in \{0, \pm 1\}$) and u, v are defined after Eq. 6.17. The phase factor makes it impossible to use the Metropolis acceptance procedure as defined since R or some derived expression thereof is to be compared with a random number generated between 0 and 1. In this section, we describe three attempts to get around this problem, each with limited success. The closely related negative sign error is discussed in the context of the WLMC procedure.

6.4.1 Ratio correction

The expression for the energy in the presence of rotation[2] is,

$$\begin{aligned} E &= \frac{Tr\left(\hat{\mathcal{H}}e^{-\beta\hat{\mathcal{H}}}\right)}{Tr\left(e^{-\beta\hat{\mathcal{H}}}\right)} \\ &= -\frac{\sum_{\{W\}} e^{i2\pi\alpha\Phi(W)}\xi^{N_d(W)}\zeta^{mN_p} \times J\left[\left(4N_p - \frac{1}{m}N_d(W_p)\right)\xi + \frac{1}{m\xi}N_d(W_p)\right]}{\sum_{\{W\}} e^{i2\pi\alpha\Phi(W)}\xi^{N_d(W)}\zeta^{mN_p}}\,. \end{aligned} \tag{6.26}$$

The ratio-correction method [34] is to associate the phase factor with the local energy and treat the expression for the energy as a ratio of two averages. On dividing the

[2] The rotation introduces a small additional term which goes as $1/\beta$ and can be neglected.

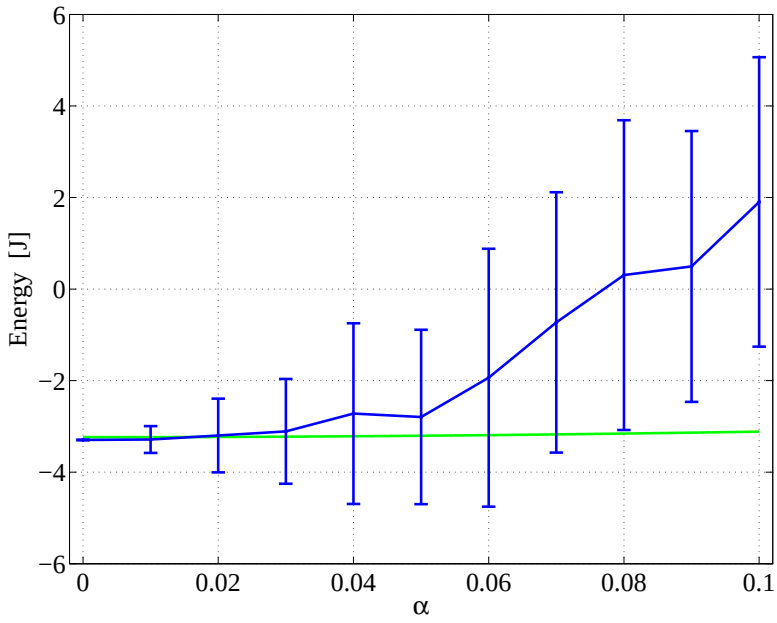

Figure 6.9: WLMC results (blue line with error bars) for the ground state energy of a single particle in a 4×4 lattice using the ratio correction method (Eq. 6.28). The green line indicates the exact diagonalization results. The error bars indicate the statistical noise in the calculation. Both the numerator and the denominator start oscillating significantly as $\alpha > 0.02$ increasing the noise in the estimate for the energy.

numerator and the denominator by the partition function for the non-rotating system, the energy is,

$$E = -\frac{\sum_{\{W\}} \xi^{N_d(W)} \zeta^{mN_p} \quad e^{i2\pi\alpha\Phi(W)} J\left[\left(4N_p - \frac{1}{m}N_d(W_p)\right)\xi + \frac{1}{m\xi}N_d(W_p)\right]}{\sum_{\{W\}} \xi^{N_d(W)}\zeta^{mN_p}} \times \frac{\sum_{\{W\}} \xi^{N_d(W)}\zeta^{mN_p}}{\sum_{\{W\}} e^{i2\pi\alpha\Phi(W)}\xi^{N_d(W)}\zeta^{mN_p}}\,. \tag{6.27}$$

If the world lines are sampled using the Metropolis acceptance as described in Eq. 6.17, then world lines are sampled with probability $\xi^{N_d(W)}\zeta^{mN_p}/\sum_{\{W\}}\xi^{N_d(W)}\zeta^{mN_p}$ and the Monte Carlo average for the energy is given by,

$$E \approx -\frac{\sum e^{i2\pi\alpha\Phi(W)} J\left[\left(4N_p - \frac{1}{m}N_d(W_p)\right)\xi + \frac{1}{m\xi}N_d(W_p)\right]}{\sum e^{i2\pi\alpha\Phi(W)}}\,. \tag{6.28}$$

Here, the sum is over measurements. Unfortunately, as can be seen in Fig. 6.9, this works well only for very small α (< 0.02). As α exceeds this value, the phase makes

both the numerator and denominator oscillate wildly giving rise to increasing shot noise as seen in the rapidly growing error bars in Fig. 6.9.

6.4.2 Complimentary world lines

One line of reasoning would be to combine world lines of equal but opposite windings thus identifying real contributions to the partition function in the following way:

$$\Re\left(Z_m\right) \;=\; \frac{Z_m + Z_m^*}{2} = \sum_{\{W\}} \cos\left(2\pi\alpha\Phi(W)\right) \xi^{N_d(W)} \zeta^{(4mN_p - N_{\rm adj}(W))}\,, \qquad (6.29)$$

where $N_{\rm adj}$ is the number of shaded tiles with a world line running on either side. If we could accept each update (W') is accepted with probability

$$P \;=\; \min\left(1, \frac{R}{1+R}\right) \qquad (6.30)$$

$$\text{where } R \;=\; \frac{\cos\left(2\pi\alpha\Phi(W')\right) \xi^{N_d(W')} \zeta^{-N_{\rm adj}(W')}}{\cos\left(2\pi\alpha\Phi(W)\right) \xi^{N_d(W)} \zeta^{-N_{\rm adj}(W)}}. \qquad (6.31)$$

we should be able to use Eq. 6.20 for the energy. However, the simulations using this rationale fail. Figure 6.10 compares the results from the WLMC simulations (solid lines) with the exact results (dashed lines) across $\alpha \in \{0, 1\}$ (the 'Hofstadter test'). As can be seen, the WLMC simulations using this acceptance procedure do not work well at all because the system keeps sliding down to the bosonic solution[3] . The cos terms in R very quickly prevent the system from building up any reasonable amount of twist. To illustrate this: for $\alpha = 0$ (*i. e.* the cos terms does not act), the system picks up winding up to $\Phi \sim \pm 15 - 20$ for a regular run but $\alpha = 0.1$ the maximum phase winding is $\Phi = 2$. The reason for this can be seen easily by plugging in $\Delta\Phi = \pm 1$ in the expression for R — very soon R turns negative preventing acceptance of further twists.

[3] Sliding to the bosonic solution is also a common problem in fermionic Monte Carlo simulations.

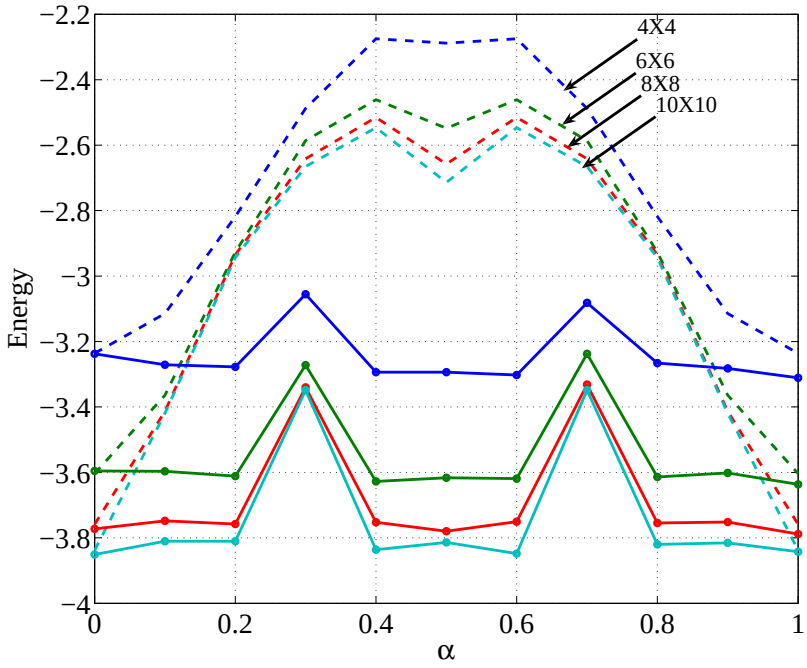

Figure 6.10: Comparison of WLMC results (solid) for the ground state energy compared with those obtained using exact diagonalization (dashed) for a singe particle in a rotating lattice. While the results are in good agreement for $\alpha = 0$ and $\alpha = 1$, the WLMC results are not correct for other values of α. The statistical error was very small for the WLMC calculations.

6.4.3 Smart acceptance

In this subsection, we present another attempt to salvage the WLMC method with rotation. For small α, the Hamiltonian can be written as,

$$\hat{\mathcal{H}} \approx -J \sum_{\langle i,j \rangle} \left(\hat{a}_i \hat{a}_j^\dagger + \hat{a}_i^\dagger \hat{a}_j \right) + iJ \sum_{\langle i,j \rangle} \phi_{ij} \left(\hat{a}_i \hat{a}_j^\dagger - \hat{a}_i^\dagger \hat{a}_j \right) \tag{6.32}$$

The time dependent Schrodinger's equation is,

$$\hat{\mathcal{H}} \left| \Psi \right\rangle = \frac{\hbar}{i} \partial_t \left| \Psi \right\rangle . \tag{6.33}$$

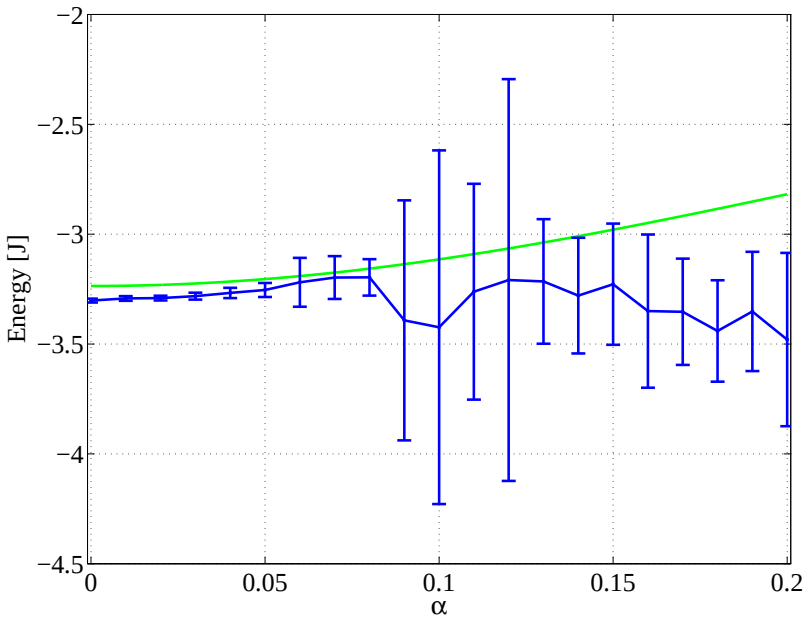

Figure 6.11: Comparison of WLMC results using smart acceptance (solid) for the ground state energy of one particle in a 4×4 lattice compared with those obtained using exact diagonalization (dashed) for a singe particle in a rotating lattice. The results using the smart acceptance procedure are slightly better than those using ratio correction. The negative-sign problem increases the statistical noise dramatically as $\alpha > 0.1$.

Integrating both sides we obtain,

$$|\Psi(t)\rangle = \exp\left(\frac{i}{\hbar}\hat{\mathcal{H}}_1 t\right)|\Psi_o\rangle \tag{6.34}$$

$$\approx \exp\left(-\frac{Jt}{\hbar}\sum_{\langle i,j\rangle}\phi_{ij}\left(\hat{a}_i\hat{a}_j^\dagger - \hat{a}_i^\dagger\hat{a}_j\right)\right)\exp\left(-\frac{iJt}{\hbar}\sum_{\langle i,j\rangle}\left(\hat{a}_i\hat{a}_j^\dagger + \hat{a}_i^\dagger\hat{a}_j\right)\right)|\Psi_o\rangle\,. \tag{6.35}$$

The last step assumes that the two terms in Eq. 6.32 commute. However, they do not and therefore this approximation gets worse with increasing α. Connecting back to the world-line analysis, for a particular world line (that is periodic in time), the first term just adds up the area covered by the particle as it travels in time, *i. e.*,

$$-\sum_{\langle i,j\rangle}\phi_{ij}\left(\hat{a}_i\hat{a}_j^\dagger - \hat{a}_i^\dagger\hat{a}_j\right) \sim -2\pi\alpha\Phi(W) \tag{6.36}$$

where $\Phi(W)$ is the flux area associated with the world line. This seems to suggest that Eq. 6.36 is an appropriate weighing factor (at least for small α) in the Metropolis acceptance, *i. e.*

$$R = \exp\left(-2\pi\alpha\Delta\Phi\right)\xi^{2u}\zeta^{-2v}\,. \tag{6.37}$$

The effect of the additional exponential term is to weigh world lines with smaller flux more for larger α. This modification to the Metropolis acceptance is compensated for by introducing a suitable factor in the expression for the energy (Eq. 6.27) and using ratio correction, the Monte Carlo average for the energy is

$$E = -\frac{\sum e^{(1+i)2\pi\alpha\Phi(W)} J\left[\left(4N_p - \frac{1}{m}N_d(W_p)\right)\xi + \frac{1}{m\xi}N_d(W_p)\right]}{\sum e^{(1+i)2\pi\alpha\Phi(W)}}\,. \tag{6.38}$$

The ground state energy, thus obtained for a single particle in a 4×4 lattice is plotted in Fig. 6.11 along with the energy obtained for the same parameters using exact diagonalization. The smart acceptance procedure works well for small α (< 0.08). For larger α, the statistical noise grows rapidly resulting in poor estimates for the energy.

6.4.4 Negative sign problem

The poor performance of the WLMC methods for rotating Bose-Hubbard systems described in the previous sections can be attributed to the negative-sign problem. The negative-sign problem is usually discussed in the context of Monte Carlo simulations for many-particle fermionic systems where the exchange of two particles introduces a negative sign in the many-body wavefunction. The problem usually manifests itself in one of two ways. The final solution could slide down to the bosonic solution or the statistical noise associated with the solution is very high. Troyer *et al.* [77] showed that a certain set of Monte Carlo methods (Directed loop, worm and stochastic series expansion (SSE)) methods cannot be used for Hubbard Hamiltonians where the hopping coefficient is not real. It is useful to expand on the negative sign problem in the context of the WLMC method.

For the 2D rotating lattice problem, a particle picks up a phase of $2\pi\alpha$ on going around a plaquette. For $\alpha = 0.5$, the many-body wavefunction picks up a negative sign when the particle goes around a plaquette once and Monte Carlo simulations for $\alpha = 0.5$ behave in a fashion similar to that of MC simulations of fermionic systems. Hence, one would expect the negative-sign problem to worsen with increasing α with the statistical noise peaking at $\alpha = 0.5$. The origin of the negative sign problem is interesting to trace. For WLMC, the sign problem comes from the algorithm, in particular the Metropolis acceptance procedure, being unable to correctly weigh the more important world lines because of the oscillation introduced by the phase factor. Consider the expression for the partition function obtained after the Suzuki-Trotter decomposition:

$$Z_m = \sum_{\{W\}} e^{i2\pi\alpha\Phi(W)} \xi^{N_d(W)} \zeta^{N_s(W) - N_{adj}(W)} \tag{6.39}$$

where the sum is over all world lines. The right hand side can also be considered as a sum over a distribution of the number of diagonal edges N_D of each world line and the flux $\Phi(W)$ associated with each. The two quantities are strongly correlated in a non-trivial way making the evaluation of the sum difficult. For the non-rotating case ($\alpha = 0$), the Metropolis acceptance does a fine job of picking out the more important distributions. The factor ξ is less than one and so the greater the value of $N_d(W)$, the smaller the contribution of that particular worldline to the partition function. Hence, the world lines picked by the Metropolis acceptance have smaller diagonal edges compared to those randomly chosen by setting $R = 1$. As demonstrated by Figs. 6.7 and 6.8, the subset of worldlines chosen by the Metropolis acceptance test gets very close to reproducing the exact solution. However, for $\alpha \neq 0$ the phase factor up front is non-zero and starts to oscillate. These oscillations cancel out even the more important contributions and hence the Metropolis acceptance has difficulty isolating the more important world lines.

The smart algorithm described earlier also has difficulty isolating the relevant $N_D - \Phi$ phase space. The phase space sampled by the smart algorithm is only a little

shifted from that sampled by the usual Metropolis but still close to the origin.

6.5 Conclusions

The WLMC method provides results in good agreement with exact solution for abelian systems but seems suspectible to the negative-sign problem when applied to a non-abelian system such as bosons in a 2D rotating lattice (or an effective magnetic field). The negative sign problem stems from the inability of the importance sampling procedure to isolate the most important worldlines. An importance-sampling method better suited than the ones we have tested could potentially give better results for small α but the outlook for circumventing the negative sign problem using this method seems bleak.

Mention must be made of one alternative method which works better than the WLMC algorithm (but is less efficient than the exact diagonalization methods used earlier in the thesis). Zhang *et al.* [87] describe a method where world lines are described in a fashion similar to that used in this chapter. However, the world lines are no longer periodic along the Trotter time axis and one end (the tail) of the world line is free. A histogram for the position of the tail as a function of Trotter time is obtained by using imaginary-time propagation. The ground state is obtained after a sufficiently long time interval after which the energy changes negligibly. This method too suffers from the negative sign problem when α is no longer small.

Chapter 7

Summary and outlook

This thesis is a study of bosons in a two-dimensional rotating lattice. The rotation and two-dimensional nature of the system make it non-abelian while the presence of a lattice introduces a discrete rotational symmetry. In the tight-binding limit, this system can be studied using a modified Bose-Hubbard Hamiltonian. The approximations implicit in the derivation of the single-band Bose-Hubbard Hamiltonian are appropriate for small angular velocities as rotation mixes in the effects of the higher bands. The single-particle Hamiltonian is identical to that for a Bloch electron in the presence of a magnetic field.

A superfluid in a deep lattice demonstrates vorticity in the presence of rotation. The effect of the lattice is to modify the phase structure. The geometry of the lattice allows for the definition of a discrete rotation operator that commutes with the Hamiltonian and hence, the system exhibits quantum phase transitions when the discrete rotational symmetry of the ground state changes as a function of rotation. Topological, perturbative and linear-response analyses indicate the presence of fractional quantum Hall features. In particular, many-body fractional quantum Hall features are seen in the single-particle system. Periodicities in the single-particle density and two-body correlation functions of the ground state are seen at fractional values of the winding parameter α. World Line Monte Carlo simulations for this system are challenging and fraught with the negative-sign problem.

The outlook for the future study of this system can be considered along three directions. The first includes analytical approaches. One could guess at a Laughlin-like many-body wavefunction for the system. Alternatively, instead of associating flux with each plaquette, one could build up a composite-particle picture by attaching Chern-Simons flux to each particle. The second direction is the development of a quantum Monte Carlo algorithm to study experimentally relevant sized systems. The prospects for developing an effective numerical method are poor because of the negative-sign error. However, possibilities of identifying additional wavefunction constraints cannot be ruled out. This would aid the formulation of an appropriate acceptance method. The third direction encompasses experimental approaches. The first rotating-lattice experiments in the weakly-interacting regime are being carried out at Boulder (JILA) by Tung *et al.* [79]. The rotating optical lattice in the JILA setup could be tilted to open up the possibility of studying the effects of the Coriolis force. The weakly-interacting system used consists of a stacked set of identical two-dimensional layers. If the layers are stacked along the z-axis and the lattice is tilted along the x–axis, the effect of the Coriolis force would be to break the two-fold symmetry in the density distribution along the y-axis. An AC field gradient could be created by introducing a jitter in any of the mirrors for the lasers used to create the 2D lattice in the setup described in Ref. [79]. Alternatively, a perturbing potential can be created via the AC Stark shift by adding an off-center Gaussian optical field with the appropriate dynamics. An observable to characterize this is obtained by imaging the density distribution along the z-axis and evaluating the differential density response to the perturbation. For the case of uncharged particles, the signature of the current response is more subtle. A recent paper [62] discusses the detection of quasi-angular momentum states of the unperturbed system using time of flight images. We have found theoretically that the current response to the perturbation can be seen clearly in the residuals obtained by rotating the time-of-flight image by 90 degrees and subtracting from the original. This emphasizes the $x - y$ asymmetry. The

strongly-interacting limit can be achieved by tuning the two-body scattering length using a Feshbach resonance. In this limit, the ground state can be examined via Bragg scattering. Another experimental avenue to realize rotating optical lattices would be with holographic projections using spatial light modulators [31]. Understanding more about bosons in a two-dimensional rotating lattice can potentially lead to exciting new physics such as the realization of composite particles in cold gases and the measurement of the equivalent of the flux quantum for mass transport.

Bibliography

[1] I. Abramowitz and I. A. Stegun. Handbook of Mathematical Functions. National Bureau of Standards, 1964.

[2] Y. Aharonov and D. Bohm. Significance of electromagnetic potentials in the quantum theory. Phys. Rev., 115(3):485–491, Aug 1959.

[3] J. F. Allen and A. D. Misener. Flow of liquid Helium II. Nature, 141:75, 1938.

[4] James G. Analytis, Stephen J. Blundell, and Arzhang Ardavan. Landau levels, molecular orbitals, and the Hofstadter butterfly in finite systems. American Journal of Physics, 72(5):613–618, 2004.

[5] M. H. Anderson, J. R. Ensher, M. R. Matthews, C. E. Wieman, and E. A. Cornell. Observation of Bose-Einstein condensation in a dilute atomic vapor. Science, 269(5221):198–201, 1995.

[6] N. W. Ashcroft and N. D. Mermin. Solid State Physics. Saunders College Publishing, 1976.

[7] M. A. Baranov, Klaus Osterloh, and M. Lewenstein. Fractional quantum Hall states in ultracold rapidly rotating dipolar fermi gases. Physical Review Letters, 94(7):070404, 2005.

[8] T. Barnes and G. J. Daniell. Numerical solution of spin systems and the S=1/2 Heisenberg antiferromagnet using guided random walks. Phys. Rev. B, 37(7):3637–3651, Mar 1988.

[9] G. Bhanot. The Metropolis algorithm. Rep. Prog. Phys., 51:429–457, 1988.

[10] Rajiv Bhat, M. J. Holland, and L. D. Carr. Bose-Einstein condensates in rotating lattices. Physical Review Letters, 96(6):060405, 2006.

[11] Rajiv Bhat, M. Kramer, J. Cooper, and M. J. Holland. Hall effects in Bose-Einstein condensates in a rotating optical lattice. Physical Review A (Atomic, Molecular, and Optical Physics), 76(4):043601, 2007.

[12] Rajiv Bhat, B. M. Peden, B. T. Seaman, M. Krämer, L. D. Carr, and M. J. Holland. Quantized vortex states of strongly interacting bosons in a rotating optical lattice. Phys. Rev. A, 74(6):063606, 2006.

[13] S. G. Bhongale, J. N. Milstein, and M. J. Holland. Resonant formation of strongly correlated paired states in rotating Bose gases. Phys. Rev. A, 69(5):053603, May 2004.

[14] E. I. Blount. Bloch electrons in a magnetic field. Phys. Rev., 126(5):1636–1653, Jun 1962.

[15] S. N. Bose. Plancks gesetz and lichtquantenhypothese. Z. Phys. A, 26(1):178–181, 1924.

[16] C. C. Bradley, C. A. Sackett, J. J. Tollett, and R. G. Hulet. Evidence of Bose-Einstein condensation in an atomic gas with attractive interactions. Phys. Rev. Lett., 75(9):1687–1690, Aug 1995.

[17] D. M. Ceperley. Metropolis methods for quantum Monte Carlo simulations. In J. E. Gubernatis, editor, The Monte Carlo Method in the Physical Sciences, volume 690, pages 85–98. AIP, 2003.

[18] T. Chakraborty and P. Pietiläinen. The Quantum Hall Effect. Springer-Verlag, 1995.

[19] N. R. Cooper and N. K. Wilkin. Composite fermion description of rotating Bose-Einstein condensates. Phys. Rev. B, 60(24):R16279–R16282, Dec 1999.

[20] K. B. Davis, M. O. Mewes, M. R. Andrews, N. J. van Druten, D. S. Durfee, D. M. Kurn, and W. Ketterle. Bose-Einstein condensation in a gas of sodium atoms. Phys. Rev. Lett., 75(22):3969–3973, Nov 1995.

[21] Roberto B. Diener, Qi Zhou, Hui Zhai, and Tin-Lun Ho. Criterion for bosonic superfluidity in an optical lattice. Phys. Rev. Lett., 98(18):180404, 2007.

[22] L.-M. Duan, E. Demler, and M. D. Lukin. Controlling spin exchange interactions of ultracold atoms in optical lattices. Phys. Rev. Lett., 91(9):090402, Aug 2003.

[23] A. Einstein. Quantentheorie des einatomigen idealen gases. Z. Phys, 261:33:879, 1925.

[24] Hans Gerd Evertz, Gideon Lana, and Mihai Marcu. Cluster algorithm for vertex models. Phys. Rev. Lett., 70(7):875–879, Feb 1993.

[25] Zyun F. Ezawa. Quantum Hall Effects. World Scientific Publishing Co, 2000.

[26] A. L. Fetter and J. D. Walecka. Quantum theory of many-particle systems. Dover Publications, June 2003.

[27] Uwe R. Fischer, Petr O. Fedichev, and Alessio Recati. Vortex liquids and vortex quantum Hall states in trapped rotating Bose gases. Journal of Physics B: Atomic, Molecular and Optical Physics, 37(7):S301–S310, 2004.

[28] Matthew P. A. Fisher, Peter B. Weichman, G. Grinstein, and Daniel S. Fisher. Boson localization and the superfluid-insulator transition. Phys. Rev. B, 40(1):546–570, 1989.

[29] Markus Greiner, Olaf Mandel, Tilman Esslinger, Theodor W. Hansch, and Immanuel Bloch. Quantum phase transition from a superfluid to a Mott insulator in a gas of ultracold atoms. Nature, 415(6867):39–44, 2002.

[30] Markus Greiner, Cindy A. Regal, and Deborah S. Jin. Emergence of a molecular Bose-Einstein condensate from a Fermi gas. Nature, 426(6966):537–540, 2003.

[31] David G. Grier. A revolution in optical manipulation. Nat Photon, 424(6950):810–816, 2003.

[32] P. C. Haljan, I. Coddington, P. Engels, and E. A. Cornell. Driving Bose-Einstein-condensate vorticity with a rotating normal cloud. Phys. Rev. Lett., 87(21):210403, Nov 2001.

[33] E. H. Hall. On a new action of the magnet on electric currents. American Journal of Mathematics, 2(3):287–292, 1879.

[34] N. Hatano. Quantum Monte Carlo study on low-dimensional spin systems. PhD thesis, University of Tokyo, 1992.

[35] J. E. Hirsch, R. L. Sugar, D. J. Scalapino, and R. Blankenbecler. Monte Carlo simulations of one-dimensional fermion systems. Phys. Rev. B, 26(9):5033–5055, Nov 1982.

[36] Douglas R. Hofstadter. Energy levels and wave functions of Bloch electrons in rational and irrational magnetic fields. Phys. Rev. B, 14(6):2239–2249, Sep 1976.

[37] M. Holland, S. J. J. M. F. Kokkelmans, M. L. Chiofalo, and R. Walser. Resonance superfluidity in a quantum degenerate fermi gas. Phys. Rev. Lett., 87(12):120406, Aug 2001.

[38] D. Jaksch, C. Bruder, J. I. Cirac, C. W. Gardiner, and P. Zoller. Cold Bosonic atoms in optical lattices. Phys. Rev. Lett., 81(15):3108–3111, Oct 1998.

[39] D. Jaksch and P. Zoller. Creation of effective magnetic fields in optical lattices: the Hofstadter butterfly for cold neutral atoms. New Journal of Physics, 5:56, 2003.

[40] P. Kapitza. Viscosity of liquid Helium below the λ-point. Nature, 141:74, 1937.

[41] A. Khare. Fractional Statistics and Quantum Theory. World Scientific Publishing Co, 2005.

[42] K. v. Klitzing, G. Dorda, and M. Pepper. New method for high-accuracy determination of the fine-structure constant based on quantized Hall resistance. Phys. Rev. Lett., 45(6):494–497, Aug 1980.

[43] W. Kohn. Analytic properties of Bloch waves and Wannier functions. Phys. Rev., 115(4):809–821, Aug 1959.

[44] A. N. Kolmogorov. über die analytischen methoden in der wahrscheinlichkeitsrechnung. Math. Ann., 104:415–458, 1931.

[45] L. D. Landau and S. M. Lifshitz. Mechanics, volume 1 of Course of Theoretical Physics. Butterworth-Heinemann, 1976.

[46] F. London. On the Bose-Einstein condensation. Phys. Rev., 54(11):947–954, Dec 1938.

[47] K. W. Madison, F. Chevy, W. Wohlleben, and J. Dalibard. Vortex formation in a stirred Bose-Einstein condensate. Phys. Rev. Lett., 84(5):806–809, Jan 2000.

[48] G. D. Mahan. Many-Particle Physics. Kluwer Academic/Plenum Publishers, third edition, 2000.

[49] A. A. Markov. Rasprostranenie zakona bol'shih chisel na velichiny, zavisyaschie drug ot druga. Izvestiya Fiziko-matematicheskogo obschestva pri Kazanskom universitete, 15:135–156, 1906.

[50] A. A. Markov. Extension of the limit theorems of probability theory to a sum of variables connected in a chain. Reprinted in Appendix B of: R. Howard. Dynamic Probabilistic Systems, volume 1: Markov Chains. John Wiley and Sons, 1971.

[51] D. Marx and P. Nielaba. Path-integral Monte Carlo techniques for rotational motion in two dimensions: Quenched, annealed, and no-spin quantum-statistical averages. Phys. Rev. A, 45(12):8968–8971, Jun 1992.

[52] D. Marx, S. Sengupta, and P. Nielaba. Diatomic molecules, rotations, and path-integral Monte Carlo simulations: N_2 and H_2 on graphite. The Journal of Chemical Physics, 99(8):6031–6051, 1993.

[53] N. Metropolis and S. Ulam. The Monte Carlo method. Journal of the American Statistical Association, 44(247):335–341, 1949.

[54] Nicholas Metropolis, Arianna W. Rosenbluth, Marshall N. Rosenbluth, Augusta H. Teller, and Edward Teller. Equation of state calculations by fast computing machines. The Journal of Chemical Physics, 21(6):1087–1092, 1953.

[55] I. Morgenstern. Monte Carlo algorithm for a two-dimensional Hubbard model for high-T_c superconductivity. Z. Phys. B, pages 291–297, 1988.

[56] I. Morgenstern and D. Würtz. Monte Carlo simulations for two-dimensional quantum systems. Z. Phys. B, 70:115–120, 1988.

[57] Erich J. Mueller. Artificial electromagnetism for neutral atoms: Escher staircase and Laughlin liquids. Phys. Rev. A, 70(4):041603, Oct 2004.

[58] Erich J. Mueller, Tin-Lun Ho, Masahito Ueda, and Gordon Baym. Fragmentation of Bose-Einstein condensates. Physical Review A (Atomic, Molecular, and Optical Physics), 74(3):033612, 2006.

[59] Qian Niu, D. J. Thouless, and Yong-Shi Wu. Quantized Hall conductance as a topological invariant. Phys. Rev. B, 31(6):3372–3377, Mar 1985.

[60] R. N. Palmer and D. Jaksch. High-field fractional quantum Hall effect in optical lattices. Physical Review Letters, 96(18):180407, 2006.

[61] B. Paredes, P. Fedichev, J. I. Cirac, and P. Zoller. 1/2-anyons in small atomic Bose-Einstein condensates. Phys. Rev. Lett., 87(1):010402, Jun 2001.

[62] B. M. Peden, Rajiv Bhat, M. Krämer, and M. J. Holland. Quasi-angular momentum of Bose and Fermi gases in rotating optical lattices. J. Phys. B: At. Mol. Opt. Phys., 40:3725–3744, 2007.

[63] Oliver Penrose and Lars Onsager. Bose-Einstein condensation and liquid Helium. Phys. Rev., 104(3):576–584, Nov 1956.

[64] R. Pepino, J. Cooper, and M. J. Holland. Open quantum systems. To be published, 2007.

[65] Lev P. Pitaevskii and Sandro Stringari. Bose-Einstein Condensation. The International Series of Monographs on Physics. Oxford University Press, USA, 2003.

[66] N. V. Prokof'ev, B. V. Svistunov, and I. S. Tupitsyn. "Worm" algorithm in quantum Monte Carlo simulations. Physics Letters A, 238(4-5):253–257, 1998.

[67] Lord Rayleigh. On James Bernoulli theorem in probabilities. Philosophical Magazine, 47:246–251, 1899.

[68] J. D. Reger and A. P. Young. Monte Carlo simulations of the spin-1/2 Heisenberg antiferromagnet on a square lattice. Phys. Rev. B, 37(10):5978–5981, Apr 1988.

[69] S Sachdev. Quantum Phase Transitions. Cambridge University Press, January 2000.

[70] J J Sakurai. Modern Quantum Mechanics. Addison Wesley, second edition, September 1993.

[71] Lawrence Schulman. A path integral for spin. Phys. Rev., 176(5):1558–1569, Dec 1968.

[72] V. Schweikhard, I. Coddington, P. Engels, V. P. Mogendorff, and E. A. Cornell. Rapidly rotating Bose-Einstein condensates in and near the lowest Landau level. Phys. Rev. Lett., 92(4):040404, Jan 2004.

[73] Anders S. Sørensen, Eugene Demler, and Mikhail D. Lukin. Fractional quantum Hall states of atoms in optical lattices. Physical Review Letters, 94(8):086803, 2005.

[74] Horst L. Stormer. Nobel lecture: The fractional quantum Hall effect. Rev. Mod. Phys., 71(4):875–889, Jul 1999.

[75] M. Suzuki. Generalized Trotter's formula and systematic approximants of exponential operators and inner derivations with applications to many-body problems. Communications in Mathematical Physics, 51(2):183–190, 1976.

[76] Olav F. Syljuåsen and Anders W. Sandvik. Quantum Monte Carlo with directed loops. Phys. Rev. E, 66(4):046701, Oct 2002.

[77] Matthias Troyer and Uwe-Jens Wiese. Computational complexity and fundamental limitations to fermionic quantum monte carlo simulations. Physical Review Letters, 94(17):170201, 2005.

[78] D. C. Tsui, H. L. Stormer, and A. C. Gossard. Two-dimensional magnetotransport in the extreme quantum limit. Phys. Rev. Lett., 48(22):1559–1562, May 1982.

[79] S. Tung, V. Schweikhard, and E. A. Cornell. Observation of vortex pinning in Bose-Einstein condensates. Physical Review Letters, 97(24):240402, 2006.

[80] R. O. Umucalilar and M. O. Oktel. Phase boundary of the boson Mott insulator in a rotating optical lattice. Physical Review A (Atomic, Molecular, and Optical Physics), 76(5):055601, 2007.

[81] W. von der Linden. A quantum Monte Carlo approach to many-body physics. Phys. Rep., 220:53–162, November 1992.

[82] Gregory H. Wannier. Dynamics of band electrons in electric and magnetic fields. Rev. Mod. Phys., 34(4):645–655, Oct 1962.

[83] N. K. Wilkin and J. M. F. Gunn. Condensation of composite bosons in a rotating BEC. Phys. Rev. Lett., 84(1):6–9, Jan 2000.

[84] N. K. Wilkin, J. M. F. Gunn, and R. A. Smith. Do attractive bosons condense? Phys. Rev. Lett., 80(11):2265–2268, Mar 1998.

[85] J. E. Williams and M. J. Holland. Preparing topological states of a Bose-Einstein condensate. Nature, 401(6753):568–572, 1999.

[86] Congjun Wu, Han-dong Chen, Jiang-piang Hu, and Shou-Cheng Zhang. Vortex configurations of bosons in an optical lattice. Phys. Rev. A, 69(4):043609, Apr 2004.

[87] Lizeng Zhang, Geoff Canright, and Ted Barnes. Simulating complex problems with the quantum Monte Carlo method. Phys. Rev. B, 49(17):12355–12358, May 1994.

[88] Wilhelm Zwerger. Mott - Hubbard transition of cold atoms in optical lattices. Journal of Optics B: Quantum and Semiclassical Optics, 5(2):S9–S16, 2003.

[89] M. W. Zwierlein, J. R. Abo-Shaeer, A. Schirotzek, C. H. Schunck, and W. Ketterle. Vortices and superfluidity in a strongly interacting Fermi gas. Nature, 435(7045):1047–1051, 2005.

Appendix A

Imaginary time propagation

Consider a wavefunction expanded in an eigen basis,

$$|\psi(t)\rangle = \sum_i |\psi_i(t)\rangle = \sum_i c_i(t)\,|\psi_i(0)\rangle \tag{A.1}$$

defined by the eigenvalues of

$$H\,|\psi_i(0)\rangle = E_i\,|\psi_i(0)\rangle \tag{A.2}$$

The Schrödinger Equation of motion is given by,

$$i\hbar\partial_t\,|\psi(t)\rangle = H\,|\psi(t)\rangle = H\sum_i c_i(t)\,|\psi_i(0)\rangle \tag{A.3}$$

$$i\hbar\partial_t \sum_i |\psi_i(t)\rangle = \sum_i E_i c_i(t)\,|\psi_i(0)\rangle = \sum_i E_i\,|\psi_i(t)\rangle \tag{A.4}$$

Solving separately for each component,

$$|\psi_i(t)\rangle = e^{-i\frac{E_i}{\hbar}t}\,|\psi_i(0)\rangle \tag{A.5}$$

For imaginary time propagation, $t \to -i\tau$

$$|\psi_i(t)\rangle = e^{-\frac{E_i}{\hbar}\tau}\,|\psi_i(0)\rangle \tag{A.6}$$

At each time step, the state with the smallest eigenvalue decays the slowest and on renormalization, $|\psi(t)\rangle$ has larger ground state character. Doing a first-order Taylor

expansion,

$$|\psi_i(t+dt)\rangle = \left(1 - \frac{E_i}{\hbar} d\tau\right) |\psi_i(t)\rangle \tag{A.7}$$

$$|\psi(t+dt)\rangle = \sum_i \left(1 - \frac{E_i}{\hbar} d\tau\right) |\psi_i(t)\rangle = |\psi(t)\rangle - d\tau \sum_i \frac{E_i}{\hbar} |\psi_i(t)\rangle \tag{A.8}$$

$$= |\psi(t)\rangle - \frac{d\tau}{\hbar} H |\psi(t)\rangle \tag{A.9}$$

The ground state is eventually obtained on successive iteration if parameters such as the size of the time step and tolerance are balanced. The norm at this point is,

$$N = \langle\psi(t+dt)|\psi(t+dt)\rangle = \langle\psi(t)|\psi(t)\rangle - \frac{2d\tau}{\hbar} \langle\psi(t)| H |\psi(t)\rangle + \left(\frac{d\tau}{\hbar}\right)^2 \langle\psi(t)| H^2 |\psi(t)\rangle \tag{A.10}$$

Ignoring the second order term for small time steps, the norm and the ground-state energy are

$$N = 1 - \frac{2d\tau E_0}{\hbar} \tag{A.11}$$

$$E_0 = \frac{\hbar(1-N)}{2d\tau}. \tag{A.12}$$

Appendix B

Hall effect in the presence of a perturbative lattice

Following the discussion from Ch. 5.4, the equation of motion for the y-coordinate of the guiding center is,

$$\begin{aligned} i\hbar\frac{dY}{dt} &= [Y, \mathcal{H} + V_{lat}] \\ &= \left[Y, \frac{1}{2m}\left(\Pi_x^2 + \Pi_y^2\right) + \left(X - \frac{\Pi_y}{m\Omega}\right) mE_x + V_0\left(\cos^2\frac{\pi x}{d} + \cos^2\frac{\pi y}{d}\right)\right] \\ &= imE_x l_B^2 + \left[Y, V_0\left(\cos^2\frac{\pi x}{d} + \cos^2\frac{\pi y}{d}\right)\right] \end{aligned} \tag{B.1}$$

$$\begin{aligned} &\left[Y, \cos^2\frac{\pi}{d}\left(X - \frac{1}{m\Omega}\Pi_y\right)\right] \\ &= \left[Y, \left(\cos\left(\frac{\pi}{d}X\right)\cos\left(\frac{\pi}{m\Omega d}\Pi_y\right) + \sin\left(\frac{\pi}{d}X\right)\sin\left(\frac{\pi}{m\Omega d}\Pi_y\right)\right)^2\right] \\ &= \left[Y, \cos\left(\frac{\pi}{d}X\right)\cos\left(\frac{\pi}{m\Omega d}\Pi_y\right)\cos\left(\frac{\pi}{d}X\right)\cos\left(\frac{\pi}{m\Omega d}\Pi_y\right)\right] \\ &+ \left[Y, \cos\left(\frac{\pi}{d}X\right)\cos\left(\frac{\pi}{m\Omega d}\Pi_y\right)\sin\left(\frac{\pi}{d}X\right)\sin\left(\frac{\pi}{m\Omega d}\Pi_y\right)\right] \\ &+ \left[Y, \sin\left(\frac{\pi}{d}X\right)\sin\left(\frac{\pi}{m\Omega d}\Pi_y\right)\cos\left(\frac{\pi}{d}X\right)\cos\left(\frac{\pi}{m\Omega d}\Pi_y\right)\right] \\ &+ \left[Y, \sin\left(\frac{\pi}{d}X\right)\sin\left(\frac{\pi}{m\Omega d}\Pi_y\right)\sin\left(\frac{\pi}{d}X\right)\sin\left(\frac{\pi}{m\Omega d}\Pi_y\right)\right] \end{aligned} \tag{B.2}$$

$$\begin{aligned} [Y, X^n] &= X^{n-1}[Y, X] + \left[Y, X^{n-1}\right]X \\ &= X^{n-1}\left(il_B^2\right) + \left(X^{n-2}\left(il_B^2\right) + \left[Y, X^{n-2}\right]X\right)X \\ &= X^{n-1}\left(il_B^2\right) + X^{n-1}\left(il_B^2\right) + \cdots + [Y, X]X^{n-1} \\ &= inl_B^2 X^{n-1} \end{aligned} \tag{B.3}$$

$$\begin{aligned}\left[Y,\cos\left(\frac{\pi}{d}X\right)\right] &= \left[Y,1-\frac{1}{2!}\left(\frac{\pi}{d}X\right)^2+\frac{1}{4!}\left(\frac{\pi}{d}X\right)^4\ldots\frac{1}{2n!}\left(\frac{\pi}{d}X\right)^{2n}+\ldots\right]\\ &= -\frac{1}{2!}\left(\frac{\pi}{d}\right)^2\left[Y,X^2\right]+\frac{1}{4!}\left(\frac{\pi}{d}\right)^4\left[Y,X^4\right]+\ldots+\frac{1}{2n!}\left(\frac{\pi}{d}\right)^{2n}\left[Y,X^{2n}\right]+\ldots\\ &= -\frac{1}{2!}\left(\frac{\pi}{d}\right)^2 2il_B^2X+\frac{1}{4!}\left(\frac{\pi}{d}\right)^4 4il_B^2X^3\ldots+\frac{1}{2n!}\left(\frac{\pi}{d}\right)^{2n}2nil_B^2X^{2n-1}\ldots\\ &= -il_B^2\frac{\pi}{d}\left[\left(\frac{\pi}{d}X\right)-\frac{1}{3!}\left(\frac{\pi}{d}X\right)^3+\ldots+(-1)^n\frac{1}{(2n-1)!}\left(\frac{\pi}{d}X\right)^{2n-1}+\ldots\right]\\ &= -il_B^2\frac{\pi}{d}\sin\left(\frac{\pi}{d}X\right)\end{aligned} \tag{B.4}$$

$$\begin{aligned}&\left[Y,\sin\left(\frac{\pi}{d}X\right)\right]\\ &= \left[Y,\left(\frac{\pi}{d}X\right)-\frac{1}{3!}\left(\frac{\pi}{d}X\right)^3+\ldots+(-1)^n\frac{1}{(2n-1)!}\left(\frac{\pi}{d}X\right)^{2n-1}+\ldots\right]\\ &= \left(\frac{\pi}{d}\right)[Y,X]-\frac{1}{3!}\left(\frac{\pi}{d}\right)^3\left[Y,X^3\right]+\ldots+(-1)^n\left(\frac{\pi}{d}\right)^{2n-1}\frac{1}{(2n-1)!}\left[Y,X^{2n-1}\right]+\ldots\\ &= il_B^2\frac{\pi}{d}-\frac{1}{3!}\left(\frac{\pi}{d}\right)^3\cdot 3il_B^2X^2+\ldots+(-1)^n\left(\frac{\pi}{d}\right)^{2n-1}\frac{1}{(2n-1)!}\cdot(2n-1)\,il_B^2X^{2n-2}+\ldots\\ &= il_B^2\frac{\pi}{d}\left[1-\frac{1}{2!}\left(\frac{\pi}{d}X\right)^2+\ldots+(-1)^n\frac{1}{(2n-2)!}\left(\frac{\pi}{d}X\right)^{2n-2}+\ldots\right]\\ &= il_B^2\frac{\pi}{d}\cos\left(\frac{\pi}{d}X\right)\end{aligned} \tag{B.5}$$

$$\left[Y,\sin\left(\frac{\pi}{m\Omega d}\Pi_y\right)\right] \;=\; \left[Y,\cos\left(\frac{\pi}{m\Omega d}\Pi_y\right)\right]\equiv 0 \tag{B.6}$$

$$\begin{aligned}&\left[Y,\cos\left(\frac{\pi}{d}X\right)\cos\left(\frac{\pi}{m\Omega d}\Pi_y\right)\cos\left(\frac{\pi}{d}X\right)\cos\left(\frac{\pi}{m\Omega d}\Pi_y\right)\right]\\ &= \left[Y,\cos\left(\frac{\pi}{d}X\right)\cos\left(\frac{\pi}{m\Omega d}\Pi_y\right)\right]\cos\left(\frac{\pi}{d}X\right)\cos\left(\frac{\pi}{m\Omega d}\Pi_y\right)\\ &+\cos\left(\frac{\pi}{d}X\right)\cos\left(\frac{\pi}{m\Omega d}\Pi_y\right)\left[Y,\cos\left(\frac{\pi}{d}X\right)\cos\left(\frac{\pi}{m\Omega d}\Pi_y\right)\right]\\ &= \left[Y,\cos\left(\frac{\pi}{d}X\right)\right]\cos\left(\frac{\pi}{m\Omega d}\Pi_y\right)\cos\left(\frac{\pi}{d}X\right)\cos\left(\frac{\pi}{m\Omega d}\Pi_y\right)\\ &+\cos\left(\frac{\pi}{d}X\right)\cos\left(\frac{\pi}{m\Omega d}\Pi_y\right)\left[Y,\cos\left(\frac{\pi}{d}X\right)\right]\cos\left(\frac{\pi}{m\Omega d}\Pi_y\right)\\ &= -il_B^2\frac{\pi}{d}\sin\left(\frac{\pi}{d}X\right)\cos\left(\frac{\pi}{m\Omega d}\Pi_y\right)\cos\left(\frac{\pi}{d}X\right)\cos\left(\frac{\pi}{m\Omega d}\Pi_y\right)\\ &- il_B^2\frac{\pi}{d}\cos\left(\frac{\pi}{d}X\right)\cos\left(\frac{\pi}{m\Omega d}\Pi_y\right)\sin\left(\frac{\pi}{d}X\right)\cos\left(\frac{\pi}{m\Omega d}\Pi_y\right)\\ &= -il_B^2\frac{\pi}{d}\left[\sin\left(\frac{\pi}{d}X\right)\cos\left(\frac{\pi}{d}X\right)+\cos\left(\frac{\pi}{d}X\right)\sin\left(\frac{\pi}{d}X\right)\right]\cos^2\left(\frac{\pi}{m\Omega d}\Pi_y\right)\\ &= -il_B^2\frac{\pi}{d}\sin\left(2\frac{\pi}{d}X\right)\cos^2\left(\frac{\pi}{m\Omega d}\Pi_y\right)\end{aligned} \tag{B.7}$$

$$
\begin{aligned}
&\left[Y, \cos\left(\frac{\pi}{d}X\right)\cos\left(\frac{\pi}{m\Omega d}\Pi_y\right)\sin\left(\frac{\pi}{d}X\right)\sin\left(\frac{\pi}{m\Omega d}\Pi_y\right)\right] \\
&= \left[Y, \cos\left(\frac{\pi}{d}X\right)\cos\left(\frac{\pi}{m\Omega d}\Pi_y\right)\right]\sin\left(\frac{\pi}{d}X\right)\sin\left(\frac{\pi}{m\Omega d}\Pi_y\right) \\
&+ \cos\left(\frac{\pi}{d}X\right)\cos\left(\frac{\pi}{m\Omega d}\Pi_y\right)\left[Y, \sin\left(\frac{\pi}{d}X\right)\sin\left(\frac{\pi}{m\Omega d}\Pi_y\right)\right] \\
&= \left[Y, \cos\left(\frac{\pi}{d}X\right)\right]\cos\left(\frac{\pi}{m\Omega d}\Pi_y\right)\sin\left(\frac{\pi}{d}X\right)\sin\left(\frac{\pi}{m\Omega d}\Pi_y\right) \\
&+ \cos\left(\frac{\pi}{d}X\right)\cos\left(\frac{\pi}{m\Omega d}\Pi_y\right)\left[Y, \sin\left(\frac{\pi}{d}X\right)\right]\sin\left(\frac{\pi}{m\Omega d}\Pi_y\right) \\
&= -il_B^2\frac{\pi}{d}\sin\left(\frac{\pi}{d}X\right)\cos\left(\frac{\pi}{m\Omega d}\Pi_y\right)\sin\left(\frac{\pi}{d}X\right)\sin\left(\frac{\pi}{m\Omega d}\Pi_y\right) \\
&+ il_B^2\frac{\pi}{d}\cos\left(\frac{\pi}{d}X\right)\cos\left(\frac{\pi}{m\Omega d}\Pi_y\right)\cos\left(\frac{\pi}{d}X\right)\sin\left(\frac{\pi}{m\Omega d}\Pi_y\right) \\
&= il_B^2\frac{\pi}{d}\left[-\sin\left(\frac{\pi}{d}X\right)\sin\left(\frac{\pi}{d}X\right) + \cos\left(\frac{\pi}{d}X\right)\cos\left(\frac{\pi}{d}X\right)\sin\right]\cos\left(\frac{\pi}{m\Omega d}\Pi_y\right)\sin\left(\frac{\pi}{m\Omega d}\Pi_y\right) \\
&= il_B^2\frac{\pi}{d}\cos\left(2\frac{\pi}{d}X\right)\cos\left(\frac{\pi}{m\Omega d}\Pi_y\right)\sin\left(\frac{\pi}{m\Omega d}\Pi_y\right) \qquad \text{(B.8)}
\end{aligned}
$$

$$
\begin{aligned}
&\left[Y, \sin\left(\frac{\pi}{d}X\right)\sin\left(\frac{\pi}{m\Omega d}\Pi_y\right)\cos\left(\frac{\pi}{d}X\right)\cos\left(\frac{\pi}{m\Omega d}\Pi_y\right)\right] \\
&= \left[Y, \sin\left(\frac{\pi}{d}X\right)\sin\left(\frac{\pi}{m\Omega d}\Pi_y\right)\right]\cos\left(\frac{\pi}{d}X\right)\cos\left(\frac{\pi}{m\Omega d}\Pi_y\right) \\
&+ \sin\left(\frac{\pi}{d}X\right)\sin\left(\frac{\pi}{m\Omega d}\Pi_y\right)\left[Y, \cos\left(\frac{\pi}{d}X\right)\cos\left(\frac{\pi}{m\Omega d}\Pi_y\right)\right] \\
&= \left[Y, \sin\left(\frac{\pi}{d}X\right)\right]\sin\left(\frac{\pi}{m\Omega d}\Pi_y\right)\cos\left(\frac{\pi}{d}X\right)\cos\left(\frac{\pi}{m\Omega d}\Pi_y\right) \\
&+ \sin\left(\frac{\pi}{d}X\right)\sin\left(\frac{\pi}{m\Omega d}\Pi_y\right)\left[Y, \cos\left(\frac{\pi}{d}X\right)\right]\cos\left(\frac{\pi}{m\Omega d}\Pi_y\right) \\
&= il_B^2\frac{\pi}{d}\cos\left(\frac{\pi}{d}X\right)\sin\left(\frac{\pi}{m\Omega d}\Pi_y\right)\cos\left(\frac{\pi}{d}X\right)\cos\left(\frac{\pi}{m\Omega d}\Pi_y\right) \\
&- il_B^2\frac{\pi}{d}\sin\left(\frac{\pi}{d}X\right)\sin\left(\frac{\pi}{m\Omega d}\Pi_y\right)\sin\left(\frac{\pi}{d}X\right)\cos\left(\frac{\pi}{m\Omega d}\Pi_y\right) \\
&= il_B^2\frac{\pi}{d}\cos\left(2\frac{\pi}{d}X\right)\sin\left(\frac{\pi}{m\Omega d}\Pi_y\right)\cos\left(\frac{\pi}{m\Omega d}\Pi_y\right) \qquad \text{(B.9)}
\end{aligned}
$$

$$
\begin{aligned}
&\left[Y, \sin\left(\frac{\pi}{d}X\right)\sin\left(\frac{\pi}{m\Omega d}\Pi_y\right)\sin\left(\frac{\pi}{d}X\right)\sin\left(\frac{\pi}{m\Omega d}\Pi_y\right)\right] \\
&= \left[Y, \sin\left(\frac{\pi}{d}X\right)\sin\left(\frac{\pi}{m\Omega d}\Pi_y\right)\right]\sin\left(\frac{\pi}{d}X\right)\sin\left(\frac{\pi}{m\Omega d}\Pi_y\right) \\
&+ \sin\left(\frac{\pi}{d}X\right)\sin\left(\frac{\pi}{m\Omega d}\Pi_y\right)\left[Y, \sin\left(\frac{\pi}{d}X\right)\sin\left(\frac{\pi}{m\Omega d}\Pi_y\right)\right] \\
&= \left[Y, \sin\left(\frac{\pi}{d}X\right)\right]\sin\left(\frac{\pi}{m\Omega d}\Pi_y\right)\sin\left(\frac{\pi}{d}X\right)\sin\left(\frac{\pi}{m\Omega d}\Pi_y\right) \\
&+ \sin\left(\frac{\pi}{d}X\right)\sin\left(\frac{\pi}{m\Omega d}\Pi_y\right)\left[Y, \sin\left(\frac{\pi}{d}X\right)\right]\sin\left(\frac{\pi}{m\Omega d}\Pi_y\right) \\
&= il_B^2\frac{\pi}{d}\cos\left(\frac{\pi}{d}X\right)\sin\left(\frac{\pi}{m\Omega d}\Pi_y\right)\sin\left(\frac{\pi}{d}X\right)\sin\left(\frac{\pi}{m\Omega d}\Pi_y\right) \\
&+ il_B^2\frac{\pi}{d}\sin\left(\frac{\pi}{d}X\right)\sin\left(\frac{\pi}{m\Omega d}\Pi_y\right)\cos\left(\frac{\pi}{d}X\right)\sin\left(\frac{\pi}{m\Omega d}\Pi_y\right) \\
&= il_B^2\frac{\pi}{d}\sin\left(2\frac{\pi}{d}X\right)\sin^2\left(\frac{\pi}{m\Omega d}\Pi_y\right) \qquad \text{(B.10)}
\end{aligned}
$$

Putting it together,

$$
\begin{aligned}
&\left[Y, \cos^2\frac{\pi}{d}\left(X - \frac{1}{m\Omega}\Pi_y\right)\right] \\
&= -il_B^2\frac{\pi}{d}\sin\left(2\frac{\pi}{d}X\right)\cos^2\left(\frac{\pi}{m\Omega d}\Pi_y\right) + il_B^2\frac{\pi}{d}\sin\left(2\frac{\pi}{d}X\right)\sin^2\left(\frac{\pi}{m\Omega d}\Pi_y\right) \\
&+ il_B^2\frac{\pi}{d}\cos\left(2\frac{\pi}{d}X\right)\cos\left(\frac{\pi}{m\Omega d}\Pi_y\right)\sin\left(\frac{\pi}{m\Omega d}\Pi_y\right) \\
&+ il_B^2\frac{\pi}{d}\cos\left(2\frac{\pi}{d}X\right)\sin\left(\frac{\pi}{m\Omega d}\Pi_y\right)\cos\left(\frac{\pi}{m\Omega d}\Pi_y\right) \\
&= -il_B^2\frac{\pi}{d}\left[\sin\left(2\frac{\pi}{d}X\right)\cos\left(\frac{2\pi}{m\Omega d}\Pi_y\right) - \cos\left(2\frac{\pi}{d}X\right)\sin\left(\frac{2\pi}{m\Omega d}\Pi_y\right)\right] \\
&= -il_B^2\frac{\pi}{d}\sin 2\frac{\pi}{d}\left(X - \frac{1}{m\Omega}\Pi_y\right) = -il_B^2\frac{\pi}{d}\sin\left(\frac{2\pi x}{d}\right) \qquad \text{(B.11)}
\end{aligned}
$$

Similarly,

$$
\left[Y, \cos^2\frac{\pi y}{d}\right] = \left[Y, \cos^2\frac{\pi}{d}\left(Y + \frac{1}{m\Omega}\Pi_x\right)\right] = 0 \qquad \text{(B.12)}
$$

$$
\begin{aligned}
i\hbar\frac{dY}{dt} &= mE_x\left(il_B^2\right) + -il_B^2\frac{\pi}{d}V_0\sin\left(\frac{2\pi x}{d}\right) \qquad \text{(B.13)} \\
\frac{dY}{dt} &= \frac{l_B^2}{\hbar}\left[mE_x - \frac{\pi}{d}V_0\sin\left(\frac{2\pi x}{d}\right)\right] \\
&= \frac{1}{m\Omega}\left[mE_x - \frac{\pi}{d}V_0\sin\left(\frac{2\pi x}{d}\right)\right] = \frac{E_x}{\Omega} - \frac{V_0}{m\Omega}\frac{\pi}{d}\sin\left(\frac{2\pi x}{d}\right) \qquad \text{(B.14)}
\end{aligned}
$$

Similarly,

$$
\frac{dX}{dt} = \frac{V_0}{m\Omega}\frac{\pi}{d}\sin\left(\frac{2\pi x}{d}\right). \qquad \text{(B.15)}
$$

If density is assumed to be constant, i.e, the lattice potential is perturbative,

$$J_y(x) = -m\rho_0 \frac{dY}{dt} = -m\rho_0 \left[\frac{E_x}{\Omega} - \frac{V_0}{m\Omega} \frac{\pi}{d} \sin\left(\frac{2\pi x}{d} \right) \right] \tag{B.16}$$

The Hall resistance is then,

$$\begin{aligned}
\frac{1}{R_H(x)} &= \frac{J_y(x)}{E_x} = -m\rho_0 \left[\frac{1}{\Omega} - \frac{V_0}{mE_x\Omega} \frac{\pi}{d} \sin\left(\frac{2\pi x}{d} \right) \right] \\
\nu &= 2\pi l_B^2 \rho_0 \\
\frac{1}{R_H(x)} &= m\frac{\nu}{2\pi l_B^2} \left[\frac{1}{\Omega} - \frac{V_0}{mE_x\Omega} \frac{\pi}{d} \sin\left(\frac{2\pi x}{d} \right) \right] \\
&= \frac{m^2\nu}{2\pi\hbar} \left[1 - \frac{V_0}{mE_x} \frac{\pi}{d} \sin\left(\frac{2\pi x}{d} \right) \right] \qquad \text{(B.17)} \\
R_H(x) &= \frac{h}{m^2\nu} \left[1 - \frac{V_0}{mE_x} \frac{\pi}{d} \sin\left(\frac{2\pi x}{d} \right) \right]^{-1} = \frac{R_0}{\nu} \left[1 - \frac{V_0}{mE_x} \frac{\pi}{d} \sin\left(\frac{2\pi x}{d} \right) \right]^{-1} \qquad \text{(B.18)}
\end{aligned}$$

Appendix C

Partition function matrix elements for the World Line Monte Carlo method

This section of the appendix contains the intermediate steps used to obtain the matrix elements in Eqs. 6.12. Consider the fragment of the Hamiltonian (Eq. 6.9) describing the contribution of the link connecting sites i and j.

$$\hat{\mathcal{H}}_{ij} = -J\left(\hat{a}_i\hat{a}_j^\dagger e^{i\phi_{ij}} + \hat{a}_i^\dagger\hat{a}_j e^{-i\phi_{ij}}\right). \tag{C.1}$$

The relevant portion of the wavefunction is$|\Psi_{ij}\rangle = |n_i n_j\rangle$where n_i and n_j are site density operators which can take on values $\{0,1\}$ for hardcore bosons. The exponentiated form of $\hat{\mathcal{H}}_{ij}$ as it appears in the partition function is,

$$\begin{aligned}
e^{-\Delta\tau\hat{\mathcal{H}}_{ij}} &= e^{J\Delta\tau\left(\hat{a}_i\hat{a}_j^\dagger e^{i\phi_{ij}} + \hat{a}_i^\dagger\hat{a}_j e^{-i\phi_{ij}}\right)} \\
&= 1 + (J\Delta\tau)\left(\hat{a}_i\hat{a}_j^\dagger e^{i\phi_{ij}} + \hat{a}_i^\dagger\hat{a}_j e^{-i\phi_{ij}}\right) \\
&\quad + \frac{(J\Delta\tau)^2}{2}\left(\hat{a}_i\hat{a}_j^\dagger\hat{a}_i\hat{a}_j^\dagger e^{i2\phi_{ij}} + \hat{a}_i\hat{a}_j^\dagger\hat{a}_i^\dagger\hat{a}_j + \hat{a}_i^\dagger\hat{a}_j\hat{a}_i\hat{a}_j^\dagger + \hat{a}_i^\dagger\hat{a}_j\hat{a}_i^\dagger\hat{a}_j e^{-i2\phi_{ij}}\right) \\
&\quad + \frac{(J\Delta\tau)^3}{3!}\left(\hat{a}_i\hat{a}_j^\dagger\hat{a}_i\hat{a}_j^\dagger\hat{a}_i\hat{a}_j^\dagger e^{i3\phi_{ij}} + \hat{a}_i\hat{a}_j^\dagger\hat{a}_i\hat{a}_j^\dagger\hat{a}_i^\dagger\hat{a}_j e^{i\phi_{ij}} + \hat{a}_i\hat{a}_j^\dagger\hat{a}_i^\dagger\hat{a}_j\hat{a}_i\hat{a}_j^\dagger e^{i\phi_{ij}}\right. \\
&\quad + \hat{a}_i\hat{a}_j^\dagger\hat{a}_i^\dagger\hat{a}_j\hat{a}_i^\dagger\hat{a}_j e^{-i\phi_{ij}} + \hat{a}_i^\dagger\hat{a}_j\hat{a}_i\hat{a}_j^\dagger\hat{a}_i\hat{a}_j^\dagger e^{i\phi_{ij}} + \hat{a}_i^\dagger\hat{a}_j\hat{a}_i\hat{a}_j^\dagger\hat{a}_i^\dagger\hat{a}_j e^{-i\phi_{ij}} \\
&\quad \left. + \hat{a}_i^\dagger\hat{a}_j\hat{a}_i^\dagger\hat{a}_j\hat{a}_i\hat{a}_j^\dagger e^{-i\phi_{ij}} + \hat{a}_i^\dagger\hat{a}_j\hat{a}_i^\dagger\hat{a}_j\hat{a}_i^\dagger\hat{a}_j e^{-i3\phi_{ij}}\right) + \ldots
\end{aligned} \tag{C.2}$$

For hardcore bosons,

$$\hat{a}_i^\dagger\hat{a}_i^\dagger|\Psi_{ij}\rangle \equiv \hat{a}_j^\dagger\hat{a}_j^\dagger|\Psi_{ij}\rangle \equiv \hat{a}_i\hat{a}_i|\Psi_{ij}\rangle \equiv \hat{a}_j\hat{a}_j|\Psi_{ij}\rangle \equiv 0. \tag{C.3}$$

Using this, Eq.C.2 reduces to,

$$\begin{aligned} e^{-\Delta\tau\hat{\mathcal{H}}_{ij}} \rightarrow_{hardcore} \; & 1 + (J\Delta\tau)\left(\hat{a}_i\hat{a}_j^\dagger e^{i\phi_{ij}} + \hat{a}_i^\dagger\hat{a}_j e^{-i\phi_{ij}}\right) \\ & + \frac{(J\Delta\tau)^2}{2}\left(\hat{a}_i\hat{a}_j^\dagger\hat{a}_i^\dagger\hat{a}_j + \hat{a}_i^\dagger\hat{a}_j\hat{a}_i\hat{a}_j^\dagger\right) \\ & + \frac{(J\Delta\tau)^3}{3!}\left(\hat{a}_i\hat{a}_j^\dagger\hat{a}_i^\dagger\hat{a}_j\hat{a}_i\hat{a}_j^\dagger e^{i\phi_{ij}} + \hat{a}_i^\dagger\hat{a}_j\hat{a}_i\hat{a}_j^\dagger\hat{a}_i^\dagger\hat{a}_j e^{-i\phi_{ij}}\right) + \ldots \end{aligned} \tag{C.4}$$

To get at the matrix elements, this operator above is allowed to act on the four different states that $|\Psi_{ij}\rangle$ can represent:

$$\begin{aligned} e^{-\Delta\tau\hat{\mathcal{H}}_{ij}}|10\rangle &= |10\rangle + (J\Delta\tau)\,e^{i\phi_{ij}}|01\rangle + \frac{(J\Delta\tau)^2}{2}|10\rangle + \frac{(J\Delta\tau)^3}{3!}e^{i\phi_{ij}}|01\rangle + \ldots \\ &= \cosh(J\Delta\tau)|10\rangle + e^{i\phi_{ij}}\sinh(J\Delta\tau)|01\rangle \end{aligned} \tag{C.5}$$

$$\begin{aligned} e^{-\Delta\tau\hat{\mathcal{H}}_{ij}}|01\rangle &= |01\rangle + (J\Delta\tau)\,e^{-i\phi_{ij}}|10\rangle + \frac{(J\Delta\tau)^2}{2}|01\rangle + \frac{(J\Delta\tau)^3}{3!}e^{-i\phi_{ij}}|10\rangle + \ldots \\ &= \cosh(J\Delta\tau)|01\rangle + e^{-i\phi_{ij}}\sinh(J\Delta\tau)|10\rangle \end{aligned} \tag{C.6}$$

$$e^{-\Delta\tau\hat{\mathcal{H}}_{ij}}|00\rangle = |00\rangle \tag{C.7}$$

$$e^{-\Delta\tau\hat{\mathcal{H}}_{ij}}|11\rangle = |11\rangle\,. \tag{C.8}$$

Alternatively, the matrix elements are given by,

$$\begin{aligned} \left\langle 10\left|e^{-\Delta\tau\hat{\mathcal{H}}_{ij}}\right|10\right\rangle &= \left\langle 01\left|e^{-\Delta\tau\hat{\mathcal{H}}_{ij}}\right|01\right\rangle = \cosh(J\Delta\tau) \\ \left\langle 01\left|e^{-\Delta\tau\hat{\mathcal{H}}_{ij}}\right|10\right\rangle &= \left\langle 10\left|e^{-\Delta\tau\hat{\mathcal{H}}_{ij}}\right|01\right\rangle^\dagger = e^{i\phi_{ij}}\sinh(J\Delta\tau) \\ \left\langle 00\left|e^{-\Delta\tau\hat{\mathcal{H}}_{ij}}\right|00\right\rangle &= \left\langle 11\left|e^{-\Delta\tau\hat{\mathcal{H}}_{ij}}\right|11\right\rangle = 1\,. \end{aligned} \tag{C.9}$$